# Title: Coronin1A regulates tumor microenvironment in colitis-associated colorectal cancer in a SUMO-dependent way

Rohan Babar[1], Poorvi Saini[1a], Neha Guliya[1a], Vishnu Ashok Kumar E[2b], Prakhar Varshney[3b], Aamir Suhail[4], Mukesh Singh[5], Prabhakar Mujagond[6], Shivangi Tyagi[1], Lalita Mehra[5], Dolly Jain[1], Prasenjit Das[5], Krishnan Vengadesan[1], Avinash Bajaj[1], Vineet Ahuja[5] and Chittur V. Srikanth [1*]

1. Laboratory of Gut Infection and Inflammation Biology, Regional Centre for Biotechnology, 3rd milestone, Faridabad-Gurugram expressway, Faridabad. India 121001.
2. Nencki Institute of Experimental Biology, Warsaw, Poland.
3. Department of Laboratory Medicine and Pathology, Centre for Immunology, University of Minnesota, USA.
4. Harvard Medical School, USA.
5. All India Institute of Medical Sciences, New Delhi, India.
6. Meril Life Science Pvt.Ltd, India

a: second author with equal contribution, b: third author with equal contribution.

*** Corresponding Author:**

C. V. Srikanth: cvsrikanth@rcb.res.in

## ABSTRACT

Inflammatory bowel disease (IBD), comprising Crohn's disease and Ulcerative colitis, is a group of multifactorial illnesses with persistent gastrointestinal inflammation and a series of undesirable consequences. IBD patients have a three times higher risk of developing colitis-associated colorectal cancer (CAC). A higher mutational burden due to persistent inflammation acts as a driver of dysplasia and even tumorigenesis. While the pathological sequence is known, the molecular mechanisms underlying the transition from chronic inflammation to CAC remain largely elusive. Post-translational modification- SUMOylation plays an integral role in shaping gut inflammation as well as several forms of cancers, including sporadic colorectal cancer. In this study, the contribution of SUMOylation to CAC pathogenesis was characterized. In the AOM-DSS CAC mice model and human IBD patient specimens, SENP5, but not other deSUMOylases, shows an altered expression. Notably, both SENP5 expression dynamics and alterations in the SUMOylome occur in chronically inflamed and neoplastic colon tissues. SENP5 interactome analysis identified Coronin1A (Coro1A), an actin-binding protein predominantly expressed in immune cells. Coro1A also shows a state-specific, distinct expression pattern in the colon. Interestingly, in contrast to wild-type mice, Coro 1A knockout mice were resistant to polyp formation, with reduced cell proliferation, oncogene expression, and epithelial-to-mesenchymal transition (EMT) gene activation, and reduced extracellular matrix (ECM) development and fibrosis, suggesting its integral role in tumorigenesis. WT mice with chronically inflamed colons and polyps have a higher number of M2-like macrophages, with increased abundance of Coro1A, suggesting a role of Coro1A in modulating the tissue microenvironment toward a pro-tumorigenic state. Mechanistically, Coro1A physically interacts with TGF-β RI and regulates TGF-β-TGF-β RI signalling endosome stability, thereby controlling TGF-β-mediated macrophage polarization. Detailed *in vitro* experiments revealed stabilization of Coro 1A through its interaction with SUMOylated Raftlin protein. Overall, Coro 1A is necessary and sufficient for TGF-β signalling, macrophage polarization, and tumorigenesis in CAC.

**Key Words:** Coronin 1A, SENP5, Transforming Growth Factor -β receptors, M2 macrophages, Colitis-associated colorectal cancer, SUMO2/3.

55 **Introduction:**

56 Colorectal cancer (CRC) is a notorious form of gastrointestinal cancer, with high incidence and
57 alarmingly poor prognosis (Bray et al., 2024; Sung et al., 2025; Schmitt & Greten, 2021). Despite
58 some improvements in therapy, the mortality of CRC remains significantly high, with a 5-year
59 survival rate for stage 4 CRC being less than 10%. Predominant forms of colorectal cancer include
60 (a) sporadic colorectal cancer (hereafter SCRC), which arises due to spontaneous mutation(s) in
61 colorectal epithelium, and (b) colitis-associated colorectal cancer (hereafter CAC), resulting from
62 chronic inflammation in the gastrointestinal tract (Foersch & Neurath, 2014; R. W. Zhou et al.,
63 2023). Multiple routes of tumor initiation and progression in CRC include distinct molecular
64 drivers, such as Adenomatous polyposis coli (APC), TP53, Kirsten rat sarcoma (KRAS), B-Raf
65 protooncogene ser/thre kinase (BRAF), PIK3CA, MMR genes (MSH2, MSH6, and MLH1), and
66 SMAD4, etc (Bogaert & Prenen, 2014; Díaz-Gay et al., 2025; Su et al., 2024). Significantly, the
67 underlying molecular pathology differs across CRC subtypes. SCRC typically follows an
68 adenoma-to-carcinoma sequence driven by prior genetic predispositions (Yamagishi et al., 2016;
69 Yin et al., 2023). Whereas CAC begins with chronic inflammation, progresses through grades of
70 dysplasia, and ultimately ends in carcinoma(Zhou et al., 2023). Consistently, patients with Crohn's
71 disease (CD) and ulcerative colitis (UC) display a 2-3-fold higher risk of developing CAC (Shawki
72 et al., 2018; Yashiro, 2014; Yin et al., 2023). Chronic inflammation exposes IBD patients to
73 repeated cycles of damage and healing of the mucosa, triggering genetic and/or epigenetic
74 perturbations. These events, referred to as induced field cancerization, prime the tumorigenesis
75 process. Consistent with this, ulcerative colitis patients display a 25-fold higher mutational burden,
76 rendering them susceptible to CAC (Kakiuchi et al., 2020). Infiltrating immune cells and resident
77 fibroblasts of the chronically inflamed gut can induce Wnt-β-Catenin, STAT3/IL-6, and
78 COX2/PGE2 pathways, which are potentially pro-tumorigenic (Dan et al., 2023; Shawki et al.,
79 2018). The tissue microenvironment in this case generates robust reactive oxygen/nitrogen species
80 along with a secretome comprising IL-6, TNF-α, GM-CSF, IL-23, and IL-17, further contributing
81 to DNA damage, epithelial proliferation, and myeloid cell recruitment and activation. Once
82 tumorigenesis is set, the tissue microenvironment is reprogrammed into a tumor-favoring
83 immunosuppressive state. TGF-β, IL-10 loop, or CCR2/CXCL-12 immune evasion pathways
84 induce polarization of immune cells into M2 macrophages, N2 neutrophils, Th2 cells, and T-reg
85 cells (Y. Deng et al., 2025; M. Zhang et al., 2023). Collectively, these events shield dysplastic cells

86 from immune surveillance and foster their proliferation. However, the mechanisms underlying
87 TME reprogramming remain elusive.

88 Macrophage involvement, characterized as CD11b$^{+}$, F4/80$^{+}$, and Ly6C high and M2 type
89 macrophages, which are referred to as tumor-associated macrophages (TAMs), significantly
90 contributes to the initiation and progression of CAC(Y. Deng et al., 2025; Shin et al., 2023;
91 Hardbower et al., 2017; Y. H. Sheng et al., 2022; Y. Wang et al., 2023; Yuan et al., 2021). Though
92 crosstalk among M2 macrophages, surrounding stromal cells, and other immune cells shapes the
93 tumor microenvironment during CAC progression, there is a lack of mechanistic understanding
94 of these events.

95 Expansion of immunosuppressive, pro-tumorigenic microenvironment- creates a permissive
96 niche for dysplastic clones to proliferate. A form of cellular post-translational modification
97 (PTM), called SUMOylation, has been shown to be integral in shaping inflammation and cancer.
98 Mediated by the action of three enzymes (E1, E2, and E3), the covalent attachment of SUMO
99 protein isoform (SUMO 1-5) to the target protein takes place, which potentially modulates its
100 function. The deSUMOylase enzymes (SENP1-3 and SENP5-7) then deconjugate the SUMO
101 attachment, making the process reversible. A series of publications have demonstrated a strong
102 connection of SUMOylation with inflammation (Mustfa et al., 2017; Suhail et al., 2019),(Long et
103 al., 2025; Ma et al., 2024). Dysregulation of the SUMOylation pathway has also been linked to
104 EMT and cancer pathophysiology (Gu et al., 2023a; L. Wang et al., 2021). The key molecules
105 involved in the transition from chronic colitis to cancer, such as NF-κB, β-Catenin, p53, AKT,
106 and STAT3, with respect to their activation, stability, and localization, are known to be regulated
107 by SUMOylation. (Gostissa et al., 1999; Lin et al., 2016; Yang et al., 2020; Z. Zhou et al., 2016)
108 Components of the SUMOylation machinery are overexpressed in SCRC and are associated with
109 poor patient prognosis (Du et al., 2016; Liu et al., 2023; Z. Sheng et al., 2025). However, it
110 remains underexplored in CAC to date. Since chronic inflammation in IBD is the primary driver
111 of CAC development, we hypothesized that SUMOylation contributes directly or indirectly to
112 CAC progression. In this study, we demonstrate a dynamic expression pattern of deSUMOylase
113 SENP5 and its prominent interacting partner Coronin1A, an actin-binding immune cell-specific
114 protein, particularly in chronically inflamed regions compared with polyp regions. Coronin1A

maintains the canonical TGF-β pathway and thus supports TGF-β-mediated M2 macrophage polarization and modulation of the tumor microenvironment in CAC.

## Results:

### • Dynamic expression pattern of SENP5 in chronic colitis and colitis-associated colorectal cancer (CAC)

To test the possible role of the SUMOylation machinery in CAC, we employed the previously reported AOM-DSS mice model of CAC (Arnesen et al., 2021). Briefly, 4 mice were included in each group: Control, Chronic colitis (hereafter referred to as CC), and the CAC. After intraperitoneal administration of azoxymethane (AOM) at 10mg/kg to the CAC group, 1% Dextran sulphate sodium (DSS) was given in their drinking water for alternate weeks for 14 weeks to the CAC and CC groups. In contrast, control mice received normal drinking water throughout the experiment. (Fig. 1A). The animals were monitored throughout the experiment, including constant recording of their body weight (Fig. 1B). Post-experimental treatment regimen, the animals were euthanized, and relevant organs were harvested. The successful establishment of the CAC model was evident by the presence of multiple polyps in the distal colon of the CAC group.

In contrast, the rest of the colon in the CAC (hereafter referred to as Non-polyp) and CC exhibited a pronounced morphological signature of chronic inflammation, characterized by reduced body weight and colon length (Fig. 1 B and C), along with enhanced splenomegaly (Fig. 1D). Histopathology of colon revealed marked infiltration of immune cells along with other signs of chronic inflammation and malignancy in CC and CAC polyps, respectively (Fig. 1E). qRT-PCR-based analysis confirmed significant upregulation of C-Myc in the polyp region (38±5.074), followed by the non-polyp region (22.83±4.642), confirming the development of malignancy in the CAC group. (Fig.S1 A). To test the involvement of SUMOylation in CAC, the abundance of SUMO1 and SUMO2/3 conjugated proteins (hereafter referred to as SUMOylome) in CC and polyp tissue lysates was examined. Compared to the control group, a detectable change in SUMO1 SUMOylome and a pronounced alteration of SUMO2/3 SUMOylome were observed in lysates from both CC and polyps (Fig.1F). An accumulation of free SUMO1 was observed in CC and polyp tissue lysate.

144 In contrast, no comparable accumulation of SUMO2/3 was observed. To investigate
145 possible involvement of deSUMOylases in this process, qRT-PCR-based expression analysis of
146 deSUMOylases was carried out. Notably, expression of SENP1, SENP2, SENP3, SENP6, and
147 SENP7 remained unchanged, while SENP5 showed a significant increase in expression in the CC
148 (2.61±0.15) and non-polyp regions (2.38±0.25) of CAC. Intriguingly, in stark contrast, SENP5
149 expression was downregulated in the CAC polyps (-2.8± 0.15) (Fig. 1G). We validated SENP5
150 expression dynamics in AOM-DSS mice tissue lysate by immunoblotting (Fig. 1H).
151 Furthermore, the relevance of this finding was investigated in actual CAC patient specimens
152 obtained from the Gastroenterology and Nutrition clinic (AIIMS, Delhi). Biopsies of CAC (N=15),
153 SCRC (N=9), and irritable bowel syndrome (IBS)(N=10) were included in this study. SUMO1 and
154 SUMO2/3 SUMOylome was examined in CAC patient tissue lysates. Consistent with the above
155 findings, a notable alteration in both SUMO1 and SUMO2/3 SUMOylome was observed. The
156 SUMO2/3 SUMOylome was more drastically affected. Moreover, consistent with the AOM-DSS
157 model, increased free sumo was observed in patient tissue lysates (Fig.1I). Furthermore,
158 expression of SENP5 in CAC patient specimens was also downregulated (~2.06 ± 0.50-fold) (Fig.
159 1J). Interestingly, in stark contrast, SENP5 was upregulated in sporadic colorectal cancer patient
160 samples (hereafter referred to as SCRC) (Fig. 1J). Immunoblots of SENP5 in CAC patient tissue
161 lysates also revealed reduced expression compared to healthy controls (Fig. 1K).
162 Additionally, $Apc^{+/-}$ and $Apc^{+/+}$mice were used to develop SCRC (Ren et al., 2019). The animals
163 were administered 2% DSS for 1 week, followed by 14 weeks of incubation to induce
164 tumorigenesis (Fig. S1B). At the conclusion of the experiment, mice were euthanized, and colons
165 were harvested. Prominent polyps were present at the distal end of the $Apc^{+/-}$ mice colon (Fig.S1C).
166 Tissue lysates from the control colon, as well as the polyp and non-polyp regions of $Apc^{+/-}$, were
167 probed for SENP5 by immunoblotting.
168 Notably, upregulated expression of SENP5 was observed in the polyp region compared to the
169 healthy control and non-polyp region (Fig.1L). Our findings of SENP5 in SCRC patients and the
170 murine model ($Apc^{+/-}$) are consistent with the previous report showing that upregulated SENP5 in
171 SCRC plays a key role in DNA damage repair (Liu et al., 2023). These results clearly indicated a
172 key difference between SCRC and CAC in SENP5 function. The marked difference in SENP5
173 expression between polyps and non-polyps in the CAC model prompted us to investigate the

mechanism in greater detail. To understand the regulatory mechanism driven by SENP5, we conducted SENP5 interactome analysis.

- **Altered Interactome of SENP5 in chronic colitis and colitis-associated colorectal cancer (CAC)**

The interactome of SENP5 was investigated by performing Co-IP of tissue lysates from control, chronic colitis, non-polyp, and polyp regions of the AOM-DSS mouse model, followed by MS/MS analysis (n=3). An IgG isotype control antibody was used as a negative control. (Fig. 2. A) Pull-down proteins were analyzed by high-resolution tandem mass spectrometry (MS/MS) using a quadrupole time-of-flight (qTOF) mass spectrometer. Initially, 2315 proteins were identified across all four groups; after contaminant removal, the remaining 1,884 proteins were subjected to further analysis. The MaxQuant platform was used to quantify the identified proteins. Peptides found in the isotype control IgG were manually subtracted from the pull-down samples during subsequent analysis. Differential proteome of control, chronic colitis (CC), non-polyp, and polyp obtained from intensity-based absolute quantification illustrated in a Venn diagram (Fig. 2 B), revealing 460 proteins in control, 508 in CC, 510 in non-polyp, and 406 in polyp. Out of which 29 proteins were unique to control, 43 were unique in CC, 74, and 21 were unique in non-polyp and polyp, respectively. Notably, 282 proteins are present in all four conditions. In the identified set of proteins, we detected SUMO2. Recent structural studies have demonstrated the active, specific interaction between SENP5 and SUMO2, underscoring the robustness of our interactome approach. (Sánchez-Alba et al., 2025) A list of proteins identified across all four conditions is provided in the supplementary.

Differential enrichment analysis of SENP5-interacting proteins showed a distinct pattern across all four conditions. 114 proteins were enriched, and 15 proteins were depleted in their interaction with SENP5 significantly in the non-polyp region. Under CC,39 proteins were enriched with SENP5, and 13 proteins were depleted in their interactions with SENP5.

In the polyp group, 132 proteins showed reduced interaction with SENP5, and five proteins showed enrichment with SENP5. Here, the definition of significance is a fold change greater than two and a $p$-value $<0.05$.

204 To understand the biological significance of proteins differentially enriched for SENP5,
205 Gene Ontology (GO) pathway analysis was performed on enriched and depleted proteins across
206 all three disease conditions. Pathway enrichment significance was assessed using hypergeometric
207 and multiple test correction at FDR less than 0.05. The *p*-values are corrected for multiple testing
208 within each category using the Benjamini-Hochberg procedure. As both non-polyp and chronic
209 colitis represent states of chronic inflammation, we chose non-polyp samples for differential GO
210 pathway enrichment analysis. In this enrichment analysis, polyp and non-polyp samples were
211 independently compared with the control to identify pathways associated with the tumor and the
212 adjacent non-tumor area.
213 Molecular function and cellular component-based GO pathway analysis revealed a profound
214 enrichment of SENP5-interacting proteins with actin filament binding or actin binding functions,
215 and the actin cytoskeleton cellular component, particularly in the non-polyp region. While the
216 enrichment of these proteins was very feeble in the polyp region (Fig. 2C) (Fig.S2. A). These
217 results suggest that SENP5 displays a more pronounced interaction with proteins involved in Actin
218 binding or linked to the actin cytoskeleton in the non-polyp region. In contrast, such interactions
219 are markedly reduced in polyp regions. From the significantly enriched list of proteins falling
220 under the Actin binding or Actin filament binding function, we shortlisted proteins Coro1A, Tmp4,
221 Myh9, Col6A3, and Dync1h1, based on their roles in cancer or disease progression, as well as the
222 presence of prominent SUMO-binding or SUMO-interacting sites (Fig.2D). The differential
223 enrichment of selected genes was visualized on volcano plot, revealing their prominent enrichment
224 in the non-polyp and CC region and abolished enrichment in polyp region. (Fig 2. E) (Fig.S2.B) It
225 underlines a shift in the interactome of SENP5 from the non-polyp to the polyp region, indicating
226 a crucial role of these proteins in disease progression. Among the selected candidates, Coro1A
227 (Coronin 1A) stood out as the most prominent pick. The immune cell-specific protein Coro1A is
228 known to interact with filamentous Actin and regulate actin dynamics by regulating the Arp2/3
229 complex (Galkin et al., 2008; Humphries et al., 2002) (Machesky et al., 1997; Shatery Nejad et al.,
230 2025). Coronin 1A plays a role in T-cell maturation, as well as T-cell receptor-based signaling,
231 neutrophil trafficking, and immune deficiency (Castro-Castro et al., 2011; Mueller et al., 2008;
232 Pick et al., 2017).Additionally, there is multiple evidence of Coronin1A involvement in
233 immunological pathways associated with chronic inflammation and its related manifestations,
234 such as lung fibrosis, lupus nephritis, and non-alcoholic steatohepatitis (NASH), and autoimmune

diseases such as systemic lupus erythematosus and multiple sclerosis. (X. Deng et al., 2024; Nicolaou et al., 2020; Siegmund et al., 2016) (Haraldsson et al., n.d.)In light of these, we set forth to investigate the role of Coronin-1A in CAC progression.

- **Coro1A is an interactor of SENP5**

The interactome analysis enabled us to identify Coronin-1A (hereafter referred to as Coro1A) as an interactor of SENP5. Coro1A-SENP5 interaction was scrutinized using a co-immunoprecipitation (Co-IP) assay. The immunoblot clearly showed strong binding of Coro1A to SENP5, particularly in tissues from CC and non-polyp areas of CAC mice (Fig. 3A). Furthermore, the expression profile of Coro1A was examined in the AOM-DSS mouse model. An elevated expression of Coro1A in CC and, interestingly, in the non-polyp region of CAC was observed. In contrast, in the polyp, much lower expression was detected (Fig. 3B). These results were validated in a murine colitis genetic model using IL10$^{-/-}$ mice. IL10$^{-/-}$ mice spontaneously develop colitis (Gunasekera et al., 2020).To establish a synchronized CAC in this background, the animals were administered AOM (10mg/kg) intraperitoneally, followed by 7 alternating cycles of low-dose 1% DSS (Fig. S3A). Post-treatment, the mice were euthanized, and the relevant organs were harvested. Notably, we did not detect any polyps in CAC mice, despite probing the colons of CC and CAC mice for Coro1A expression. Immunoblotting of colon lysates revealed a pronounced increase in Coro1A expression in both CC and CAC tissues compared to untreated controls (Fig. 3C), confirming that Coro1A upregulation is not restricted to a single chronic colitis model but is found in a broad range of chronic colitis models. Next, the expression of Coro1A was analyzed in an acute colitis mouse model. The acute colitis model was developed as described by (Suhail et al., 2019)(Fig. S3B). Coro1A expression was not modulated in the acute colitis mouse model (Fig. S3C). These results implied that Coro1A induction is limited to chronic colitis. Additionally, we probed Coro1A in colonic lysates from the Apc$^{+/-}$ SCRC model and found no significant differences in its expression; however, a trend of decreasing Coro1A expression was observed in the non-tumor adjacent area and the tumor area. (Fig. S3D). Next, the relevance of Coro1A expression in chronic gut inflammation was examined in human colon biopsies. Biopsy samples from UC (N=5) patients also showed significantly elevated Coro1A expression compared to those

265 from IBS patients (N=4), as shown by immunoblot (Fig. 3D). These findings suggest a potential
266 role for Coro1A in the development of colitis-associated cancer.

267 Together, these findings indicate that Coro1A upregulation is a feature specific to chronic
268 inflammatory settings and inflammation-driven tumorigenesis, rather than sporadic tumor
269 development. To gain insights into the subcellular localization of Coro1A, immunohistochemistry
270 (IHC) was performed. Enhanced expression of Coro1A was observed in infiltrating immune cells
271 in the CC and non-polyp areas compared with the control. Coro1A protein was detected in the
272 polyp region, though with less intensity as compared to CC and non-polyp (Fig. 3E). Furthermore,
273 these observations were confirmed in patient biopsy-derived archived slides, which showed a
274 consistent increase in Coro1A expression in infiltrating immune cells in UC and the adjacent
275 inflamed CAC tumor area compared to the IBS control. Notably, a prominent presence of Coro1A
276 in the CAC tumor, albeit less than in non-polyp and UC, was observed (Fig. 3F). These results
277 reveal that Coro1A is uniformly present in immune cells and is consistently upregulated during
278 chronic inflammation. However, an unusually high abundance of Coro1A in the non-polyp region
279 of CAC prompted us to investigate its role in CAC development.

280• **Absence of Coro1A confers resistance to CAC development in mice**

281 To understand the relevance of increased Coro1A expression in infiltrating immune cells, we
282 employed Coro1A KO mice (hereafter, Coro1A$^{KO}$). Coro1A $^{KO}$ mice were generated in the
283 laboratory of J.M. Penninger (IMBA, Vienna) by using *a Cre/LoxP*-based gene-targeted strategy.
284 The deleted region encompasses the entire coding sequence after exon 1 (Kaminski et al., 2011).
285 Complete KO of the Coro1A gene was confirmed by immunoblot of Coro1A from colonic tissue
286 lysates of Wild-type mice (WT) and Coro1A$^{KO}$ mice (Fig. S4A and B).
287 To understand the relevance of Coro1A in CAC development, WT and Coro1A$^{KO}$ were subjected
288 to the AOM-DSS treatment as described in Fig.1A. A schematic representation of the experimental
289 design, which lasted for 14 weeks, is shown in Fig. 4A. The animals were monitored throughout
290 the experiment, including constant recording of their body weight (Fig. S4C). Post experiment,
291 mice were euthanized, and the colon, spleen, and other relevant organs were harvested. Gross
292 morphological parameters were evaluated to compare the extent of disease development in WT
293 and Coro1A$^{KO}$ mice. The length of the colon and splenomegaly were analyzed in both CC and
294 CAC groups across both genotypes. A considerable reduction in colon length of CC and CAC

295 categories of each genotype was observed, indicating the establishment of colitis (Fig. S4.D). No
296 significant differences were observed in the respective sub-categories between the WT and
297 Coro1A$^{KO}$ groups. However, the colon from WT mice in the CAC group showed a wider distal
298 end than those in all other groups from both genotypes, suggesting the possible presence of polyps.
299 In line with this, the colon from WT mice in the CAC group showed the development of multiple
300 polyps, a feature absent in Coro1A$^{KO}$ mice (Fig. 4B). Moreover, there was an evident
301 splenomegaly in the case of the CAC$^{WT}$ group, which was more pronounced in the WT as
302 compared to their KO counterparts (Fig. S4E). H&E staining of colonic tissue sections from WT
303 and Coro1A$^{KO}$ mice across all conditions was carried out. Sections from CC$^{WT}$ and CAC $^{WT}$ groups
304 showed prominent markers of colitis and cancer, including high-grade dysplasia, mild field effect,
305 collagen deposition, distorted crypt architecture, a widened muscularis layer, and moderate
306 inflammation with immune cell infiltration.
307 In contrast, the CC and CAC groups of Coro1A$^{KO}$ mice exhibited no or very low-grade dysplasia,
308 field effect, crypt distortion, and collagen deposition, accompanied by prominent immune cell
309 infiltration and inflammation, as indicated by the histopathology score (Fig. 4C and Fig. S4F).
310 Further Sirius red staining showed prominent collagen deposition in CC$^{WT}$ and CAC $^{WT.}$In contrast,
311 Coro1A$^{KO}$ mice exhibited strikingly less collagen deposition in CC and CAC, indicating attenuated
312 extracellular matrix (ECM) deposition in Coro1A $^{KO}$ mice compared with WT. (Fig.4D). The lack
313 of polyp formation and absence of adenocarcinoma in Coro1A$^{KO}$ CAC mice necessitated the
314 investigation of molecular markers associated with proliferation, inflammation, extracellular
315 matrix (ECM) deposition, and epithelial-to-mesenchymal transition (EMT) in colonic tissue
316 lysates from both genotypes across all samples.
317 Both Ki-67, a proliferation marker, and C-Myc, a protooncogene, were markedly elevated in CC
318 $^{WT}$(2.973±0.6296; 2.363±0.3234) and CAC$^{WT}$ (6.600±0.05003; 5.050±0.3396) mice, whereas they
319 were downregulated in the CC$^{Coro1aKO}$(-2.723±1.513;-1.987±0.7342) and CAC$^{Coro1aKO}$(-
320 3.137±0.2270; -1.980±0.2722) counterparts (Fig.4.E). Expression of E-Cadherin was dramatically
321 downregulated in CC$^{WT}$(-29.10 ± 9.570) while the CAC$^{WT}$ group showed marked upregulation
322 (14.22±1.650). Interestingly, both features were completely absent in the Coro1AKO groups. This
323 pattern of E-cadherin expression aligns with recent reports of elevated E-cadherin expression in
324 solid tumors (Burandt et al., 2021; Rodriguez et al., 2012) (Fig. S4G). Cox2, a pro-inflammatory
325 marker, was downregulated significantly in CC(-8.043±2.687) and CAC(-4.457±1.057) of WT,

326 whereas Coro1A$^{KO}$ CC and CAC showed very subtle changes. Anti-inflammatory and pro-wound
327 healing marker-Arginase-1(Arg1) was markedly upregulated in CAC$^{WT}$(6.700±0.6255), and
328 downregulated in CC$^{WT}$(-3.600±0.5615). In the Coro1A$^{KO}$ CC and CAC mice, this pattern was
329 observed, but with significantly lower values (-2.097±0.3783; 1.847±0.8995) (Fig.4F). Together,
330 these results indicate a tendency toward higher cell proliferation, higher oncogenic, excessive
331 wound healing, anti-inflammatory, and lower pro-inflammatory activity in WT mice; however,
332 these features were either absent or diminished in Coro1A$^{KO}$ mice.
333 Further analysis of ECM remodeling genes, including Fibronectin, α-SMA, and Col1A1, revealed
334 significant upregulation in WT mice from the CC(4.183±0.6451; 10.04±3.008; 4.227±0.9239) and
335 CAC(5.233±0.04910; 2.633±0.9347; 6.157±0.6388) groups. In contrast, their expression was
336 comparatively lower in respective groups of CC$^{Coro1A\ KO}$ (-4.727±1.916; -2.898± 0.3824; 0.5067±
337 0.1074) and CAC$^{Coro1AKO}$(-4.370±1.344;-2.513±0.1995;1.100±0.04933) mice (Fig.4G).
338 Consistently, EMT-associated transcription factors SNAIL and SLUG were also upregulated in
339 CAC $^{WT}$ (7.072±1.964; 24.33± 5.503) relative to the counterpart Coro1A$^{KO}$ tissues group (-7.223±
340 0.2706; 0.5819± 0.3946) (Fig.S4H). Additionally, p53 was upregulated in CAC$^{WT}$ (1.490± 0.4539)
341 compared to CC$^{WT}$ (-0.1667±0.3820) and both Coro1A KO conditions(-0.300±0.1102;
342 0.1367±0.1637). It is consistent with reports of p53 overexpression in UC, CAC, and sporadic
343 colorectal cancer (Khursheed et al., 2024; Lu et al., 2017; Popp et al., 2016) (Fig. 4H). Altogether,
344 these findings demonstrate that molecular footprints associated with proliferation, inflammation,
345 ECM remodeling, and EMT are pronounced in WT mice, correlating with their increased
346 susceptibility to CAC development compared to Coro1A$^{KO}$ mice.
347

348• **Increased expression of Coro1A is associated with M2 macrophages**

349 To understand the immune cell type that shows enhanced Coro1A expression in chronic
350 inflammatory conditions and plays a crucial role in CAC development, we analyzed immune cells
351 isolated from the lamina propria of control, CC, non-polyp, and polyp tissues from WT mice by
352 flow cytometry. Flow cytometry was performed using predefined gating strategy, as shown in Fig.
353 S5A. Analysis revealed, in contrast to the control group, a marked increase in the number of
354 F4/80$^{+}$ and CD11b$^{+}$ macrophages in CC, non-polyp, and polyp regions (Fig. 5A and B), while the
355 neutrophil count (CD45$^{+}$ and Ly6G$^{+}$) was decreased in the CC and non-polyp regions, but

356 unexpectedly elevated in the polyp tissue (Fig S.5 B and C). To confirm whether Coro1A is
357 increased in infiltrating macrophages, the Median fluorescence intensity (MFI) of Coro1A during
358 flow cytometric analysis was calculated. MFI analysis revealed increased abundance of Coro1A
359 in infiltrating macrophages across all three conditions (Fig. 5C). While decreased abundance of
360 Coro1A was observed in neutrophils in the CC and non-polyp regions, it was strikingly elevated
361 in the polyp region (Fig. S5D). Under prolonged chronic inflammation, dynamic macrophages
362 exhibit remarkable plasticity, adapting to either a pro-inflammatory (M1) or an anti-inflammatory
363 (M2) state. Overall, macrophages, particularly anti-inflammatory, pro-tumorigenic M2
364 macrophages, utilize a variety of signaling cascades to promote CAC. (Hardbower et al., 2017;
365 Wang et al., 2023; Yuan et al., 2021 Suarez-Lopez et al., 2018) Further analysis demonstrated a
366 gradual enrichment of($Arg^+$-1) M2-like macrophages in CC, non-polyp, and polyp regions
367 compared to the $iNOS^+$ M1-like macrophages (Fig. 5D). A significantly higher M2 ($Arg^+$) /M1
368 ($iNOS^+$) ratio was seen in the area of non-polyp and polyp (Fig.5E). Subsequent analysis revealed
369 increased MFI of Coro1A is associated with $Arg^+$ M2 macrophages (Fig. 5F), whereas $iNOS^+$ M1
370 macrophages did not show such a trend (Fig. S5E).

371 To gain a mechanistic understanding of these observations, *in vitro* experiments were conducted.
372 Macrophages were treated with IL-4 and TGF-β to induce an M2-like phenotype as previously
373 reported (Stein et al., n.d.)(Zhang et al., 2016).Notably, exposure to these two cytokines increased
374 intracellular Coro1A levels (Fig. 5 G and H). This phenotype was accompanied by the upregulation
375 of several canonical M2 macrophage markers 14 hours post cytokine treatment (p.c.t) (Fig. 5I and
376 J).

377 Considering TGF-β being one of the inducers of Coro1A, the levels of TGF-β in the tissue lysates
378 of the AOM-DSS murine model were verified. Found an increased abundance of TGF-β in the CC
379 and CAC colon of IL-$10^{-/-}$ AOM-DSS mice, as determined by ELISA, underscoring the connection
380 between TGF-β and Coro1A signaling (Fig. 5 K). Collectively, these results suggest that Coro1A
381 is involved in the function of M2-like macrophages and thus modulates the tumor
382 microenvironment.

383• **Coro1A interacts directly with the TGF-βRI and controls TGF-β-mediated M2 macrophage**
384 **polarization**

385 Previous reports have implicated Coro1A in regulating TGF-βRI and in the differentiation of Th17
386 $CD4^+$ T cells (Kaminski et al., 2011). Based on this, we set forth to investigate the possible
387 mechanism by which Coro1A crosstalk with TGF-β-signaling in macrophages. Co-IP analyzed the
388 potential interaction between Coro1A and TGF-βRI. RAW264.7 cell lysate was pulled down with
389 an anti-Coro1A antibody, followed by immunoblotting against TGF-βRI. A direct interaction of
390 Coro1A with TGF-βRI was evident (Fig. 6.A). Furthermore, structured illumination microscopy
391 (SIM) revealed a direct interaction between TGF-βRI and Coro1A, as evidenced by strong
392 colocalization signals (Fig.6B). Furthermore, interaction of Coro1A was not restricted to TGF-β
393 RI; it also interacted with TGF-β RII (Fig. S. 6A).

394 The role of Coro1A in macrophage function was next assessed. J774 macrophages stably knocked
395 down for Coro1A (hereafter referred to as J774 $^{\text{Coro1A KD}}$) were used (Fig. 6C) and (Fig.S6B)
396 (Jayachandran et al., 2008). The interaction between Coro1A and TGF-βRI was validated in J774
397 $^{\text{WT}}$ and J774 $^{\text{Coro1A KD}}$ cells by antibody-based pull-down. The blots revealed interaction of Coro1A
398 and TGF-βRI in J774 $^{\text{WT}}$ cells but not in J774 $^{\text{Coro1A KD}}$ cells (Fig. 6D).
399 Under the basal level, there is no significant change in the expression of prototypical M2 markers
400 like Arginase-1, IL-10, master regulator of M2 macrophage markers SNAIL, and TGF-βRI, in
401 $J774^{\text{WT}}$ and $J774^{\text{Coro1A KD}}$ cells. Upon stimulation with TGF-β, $J774^{\text{WT}}$ exhibited strong induction
402 of M2 markers Arginase-1 (6.877±1.372) and SNAIL (5.395±0.856), whereas this phenotype was
403 severely blunted in $J774^{\text{Coro1A-KD}}$ cells (Arginase-1 0.5067±0.0898, SNAIL 2.201±1.164)
404 measured by qRT-PCR (Fig.6E, Left and Right). In line with these changes in gene expression,
405 the secretion of the anti-inflammatory cytokine IL-10 was significantly higher in $J774^{\text{WT}}$ cells
406 (55.83±14.29) after TGF-β stimulation; however, in J774 $^{\text{Coro1A KD}}$ cells treated with TGF-β, IL-10
407 secretion was considerably lower (6.904±15.23). (Fig. 6F). Furthermore, Arginase-1-positive cells
408 were quantified using Flow Cytometry, revealing that J774 $^{\text{WT}}$ cells showed a pronounced response
409 to TGF-β stimulation, with increased Arginase-1-positive cells (27.67±9.615), whereas J774 $^{\text{Coro1A}}$
410 $^{\text{KD}}$ cells failed to respond to TGF-β with the same efficiency (4.667±2.749). (Fig. 4G). Considering
411 reduced expression of Arginase, SNAIL, and less secretion of IL-10, the expression of TGF-βRI
412 in J774 $^{\text{WT}}$ and J774 $^{\text{Coro1A KD}}$ cells was examined. TGF-βRI showed comparable basal levels of
413 expression in both J774 $^{\text{WT}}$ and J774 $^{\text{Coro1A KD}}$ cells. Upon TGF-β exposure, it was upregulated in
414 both cell types (1.993±0.1658; 1.513±0.4103) (Fig. 6H). This indicates that TGF-β receptor
415 transcription is intact in J774 $^{\text{coro1A KD}}$ cells, and that impaired signaling likely arises from defects

416 at the protein level. Mechanistically, in the canonical TGF-β signaling pathway, the activated TGF-
417 β receptor phosphorylates SMAD2/3, which form a complex with SMAD4 and translocate to the
418 nucleus to drive transcription of target genes (Nakao & Imamura, 1997). Accordingly, TGF-β
419 stimulation increases the nuclear accumulation of pSMAD2/3 in cells responding to the TGF-β
420 trigger, as compared to less or non-stimulated cells. In line with the above observation, J774 $^{WT}$
421 cells exposed to TGF-β showed enhanced nuclear accumulation of SMAD3 as compared to J774
422 $^{Coro1A\ KD}$ cells (Fig. 6I). Furthermore, bone marrow-derived macrophages (hereafter referred to as
423 BMDMs) isolated from WT mice showed promising accumulation of pSMAD3 in their nucleus
424 on TGF-β stimulation, whereas Coro1A$^{KO}$ mice-derived BMDMs showed impaired nuclear
425 accumulation of pSMAD3, as shown by immunofluorescence microscopy (Fig. 6J). Together,
426 these findings demonstrate that Coro1A is a critical regulator of TGF-β-mediated SMAD3
427 activation in macrophages and, consequently, of TGF-β-mediated macrophage polarization.

428

429• **Coro1A is required for the stability of TGF-βRI**

430 To understand the relevance of Coro1A interaction with TGF-βRI, TGF-βRI expression was
431 investigated in stable J774 $^{Coro1A\ KD}$ cells. A significant decrease in TGF-βRI protein expression
432 levels was seen in J774$^{Coro1A\ KD}$ cells compared to J774$^{WT}$ cells (Fig. 7A). Additionally, TGF-βRI
433 expression was validated in BMDM$^{WT}$ and BMDM $^{Coro1A\ KO}$ by confocal microscopy. A significant
434 reduction in FITC-labelled TGF-βRI fluorescence intensity in BMDM $^{Coro1A\ KO}$ was observed, as
435 compared to BMDM $^{WT}$ (Fig. 7B). Furthermore, to assess overall TGF-βRI-mediated signaling in
436 J774 $^{Coro1A\ KD}$ cells, pAKT/AKT level, as one of the immediate downstream readouts of the TGF-
437 β signaling, was examined. TGF-β-induced pAKT level was markedly reduced in J774 $^{Coro1A\ KD}$
438 cells as compared to J774 $^{WT}$ cells, indicating impaired SMAD-independent signaling as well in
439 J774 $^{Coro1A\ KD}$ cells (Fig. 7C). TGF-β signaling is autoregulatory; the activation of intact TGF-β
440 receptors induces *TGFB1* transcription, leading to enhanced precursor synthesis and the release of
441 mature TGF-β into the supernatant. Conversely, impaired TGF-βR signaling lowers both
442 intracellular precursor levels and the secreted TGF-β (Deng et al., 2024; Massagué, 2012).ELISA
443 and immunoblot verified autoregulatory secretion of TGF-β in cell supernatant from J774 $^{WT}$ and
444 J774 $^{Coro1A\ KD}$ cells. A considerably lower concentration of TGF-β appeared in the cell supernatant
445 collected from J774 $^{Coro1A\ KD}$ cells as compared to J774 $^{WT}$ cells (Fig. 7D). These findings were

446 further supported by immunoblot analysis of secreted TGF-β in the supernatant, confirming a
447 reduced secretion of TGF-β from J774 $^{Coro1A\ KD}$ cells (Fig.S6C). Further, the TGF-β level in the
448 tissue lysate of WT and Coro1A $^{KO}$ CAC mice model was measured using ELISA. TGF-β levels
449 were upregulated in CC $^{WT}$ and CAC $^{WT}$ compared to both WT Control and their respective Coro1A
450 $^{KO}$ counterparts, indicating a marked reduction in TGF-β synthesis in Coro1A $^{KO}$ mice. (Fig. 7E).
451 Next, the mechanism by which Coro1A safeguards TGF-βRI from degradation was investigated.
452 Previous studies have shown that Coro1A decorates signaling endosomes of the neuronal growth
453 factor (NGF)-tropomyosin-related kinase type-1 (TrkA) once it is internalized within the neuronal
454 cell body from lysosomal degradation. (Suo et al., 2014).
455 We hypothesized that the TGF-β-TGF-βRI complex, upon internalization, is protected from
456 degradation by Coro1A in macrophages. In line with this, bafilomycin-A1-mediated blocking of
457 lysosomal acidification rescued the TGF-βRI level in J774 $^{Coro1A\ KD}$ cells as compared to untreated
458 J774 $^{Coro1A\ KD}$ cells (Fig.7F), whereas blocking proteasomal degradation by MG-132 treatment
459 resulted in no change in TGF-βRI expression in J774 $^{Coro1A\ KD}$ cells. (Fig.S6D). As a positive
460 control, p62 accumulated under bafilomycin-A1 treatment, while polyubiquitinated proteins were
461 enriched following MG-132 treatment, confirming effective lysosomal and proteasomal inhibition,
462 respectively (Fig. S6E and F). Furthermore, colocalization of FITC-labelled TGF-βRI(Green) with
463 Lysotracker (Red) in BMDM $^{WT}$ and BMDM $^{Coro1A\ KO}$ revealed a higher degree of TGF-βRI
464 accumulation within lysosomes of BMDM $^{Coro1A\ KO}$, as observed by strong yellow color puncta
465 (Fig. 7G). Together, these results suggest that in the absence of Coro1A, canonical and non-
466 canonical TGF-β signaling are hampered because TGF-β-TGF-βRI signaling endosomes are
467 predominantly targeted for lysosomal degradation.
468
469 • **Coro1A utilizes the calcium-calcineurin signaling pathway to protect TGF-βRI from**
470 **degradation.**
471 Previous reports have demonstrated that Coro1A-mediated calcium influx protects NGF-TrkA
472 signaling endosomes and *M. tuberculosis* phagosomes from lysosomal degradation (Jayachandran
473 et al., 2007; Mueller et al., 2008; Suo et al., 2014) (Giorgio Ferrari, 1999).
474 To test whether Coro1A utilizes calcium ion influx to stabilize TGF-β-TGF-β RI signaling
475 endosomes from lysosomal degradation, RAW 264.7 cells were treated with cell-permeable
476 calcium chelator 1,2-bis(o-aminophenoxy) ethane-N, N, N, N-tetraacetic acid, tetraacetoxymethyl

477 ester (BAPTA-AM) and assessed the TGF-βRI level by immunoblotting. Notably, the level of
478 TGF-βRI in RAW264.7 cells treated with BAPTA-AM was significantly lower than that in
479 untreated controls (Fig. 8A). The result phenocopied the finding observed in the Coro1A-depletion
480 condition. (Fig.7A). Moreover, increasing calcium concentration in J774 $^{Coro1A\ KD}$ cells using
481 calcium ionophore Ionomycin partially rescued TGF-β RI level as compared to J774 $^{Coro1A\ KD}$ cells
482 (Fig. 8B). Taken together, these data suggest stability of TGF-βRI is directly linked to the ability
483 of Coro1A to induce calcium release. Provided that *M. tuberculosis* (Jayachandran et al., 2007)
484 and NGF-TrkA signaling endosomes (Suo et al., 2014) utilize calcium ion-activated calcineurin
485 phosphatase to evade lysosomal degradation, it was speculated that TGF-β RI signaling endosomes
486 may employ a similar mechanism. In RAW264.7 cells, potent calcineurin inhibitors, Cyclosporin
487 A (CsA) and FK506, were added to test whether inhibiting calcineurin phosphatase results in
488 degradation of TGF-β RI. Similar to BAPTA-AM, treatment with CsA and FK506 resulted in a
489 significant reduction in TGF-βRI expression (Fig. 8C and D). Collectively, these results suggest
490 that Coro1A, associated with TGF-β-TGF-β RI signaling endosomes, utilizes the calcium-
491 calcineurin signaling pathway to protect TGF-β RI signaling endosomes from lysosomal
492 degradation in the macrophages.
493
494• **SUMO2/3 governs the stability of Coro1A**
495 Since Coro1A was identified in this study as an interactor of deSUMOylase SENP5, we tested
496 whether Coro1A is SUMO-modified. Co-immunoprecipitation was performed using anti-
497 SUMO2/3 antibody in J774$^{WT}$ cell lysates, followed by immunoblotting against Coro1A.
498 Interestingly, Coro1A was detected in the SUMO2/3 pull-down (Fig. 9A, bottom). Moreover, the
499 Coro1A band appeared at its usual molecular weight, with no shift in molecular weight detected,
500 indicating that Coro1A itself does not undergo SUMOylation. Surprisingly, in reverse Co-IP with
501 Coro1A, SUMO2/3 bands appeared in the range of 75 kDa-150 kDa, suggesting that Coro1A may
502 interact with already SUMOylated proteins (Fig. 9A, Top). In line with previous findings on
503 Coro2A, where it interacts with SUMOylated Liver X-receptors (LXRs) through SUMO-
504 interacting motifs (SIM)(Huang et al., 2011). It was speculated that Coro1A may utilize its SIM
505 site to interact with SUMOylated proteins. SIM, a conserved hydrophobic amino acid (V/I V/I X
506 V/I), followed by acidic residues, enables the protein to interact with other SUMOylated proteins,

507 influencing their stability, localization, and downstream signaling.(Kerscher, 2007; Song et al.,
508 2004).
509 Using GPS-SUMO and JASSA (Beauclair et al., 2015; Gou et al., 2024),we identified potential
510 SIM sites in Coro1A; however, sites recognized by both tools with high scores were prioritized
511 (Fig.9 B). SIM Sites 124-128, 155-159, and 167-171 were selected for further study. These
512 findings raise two questions: the functional relevance of Coro1A SIM sites and the identity of the
513 protein undergoing SUMOylation to which Coro1A interacts via its SIM site. Conservation of the
514 chosen SIM sites was analyzed using a multiple-sequence alignment across different species (Fig.
515 S7A). To identify the critical SIM site required for Coro1A to function and the relevance of SIM-
516 SUMO interaction, SIM sites were perturbed by performing Site-Directed Mutagenesis (SDM) by
517 replacing the hydrophobic Valine (V) residue with positively charged Lysine (K) residue; this
518 change is expected to disrupt the SIM-SUMO interaction, as established by Song et al. (2004)
519 (Fig.S7 B).
520 To understand the fate of these mutants, Coro1A-GFP $^{WT}$ and SIM mutants (Coro1A-GFP $^{V124K}$,
521 Coro1A-GFP $^{V155K}$, and Coro1A-GFP $^{V167K}$) were transfected into RAW264.7 cells, and protein
522 expression was analyzed on an immunoblot. A marked reduction in the expression of Coro1A-
523 GFP$^{V155K}$ was observed on immunoblot (Fig. 9C). To validate the above finding, the
524 hydrophobicity of the SIM site in the Coro1A $^{V155K}$ mutant was replenished by replacing lysine
525 (K) with alanine (A), resulting in partial rescue of the Coro1A-GFP protein (Fig. 9D).
526 Furthermore, confocal microscopy of RAW264.7 cells transfected with Coro1A-GFP $^{WT}$ and
527 Coro1A SIM mutants showed that neither mutation altered localization nor induced aggregation
528 in Coro1A. However, Coro1A-GFP $^{V155K}$ showed a marked reduction in GFP fluorescence
529 intensity as compared to Coro1A-GFP $^{WT}$ and other SIM mutants (Fig. 9E).
530 Overall, these results suggest that perturbing SIM sites affects Coro1A stability. Molecular
531 dynamics simulations were carried out between Coro1A $^{WT}$ and Coro1A $^{V155K}$ mutant using the
532 CABS-Flex 3.0 server (https://doi.org/10.1093/nar/gkaf412) to rule out the possibility of structural
533 aberration induced by the V155K mutation in Coro1A. The results showed that both the wildtype
534 and V155K mutant proteins exhibited similar dynamic behavior, indicating that the mutation does
535 not induce any significant structural aberration that could cause protein denaturation (Fig. S7C).
536 Next, SIM-SUMO interaction was disrupted independently of Coro1A by transiently knocking
537 down the only SUMO-conjugating enzyme, UBC9, in RAW264.7 cells, thereby lowering global

538 SUMOylation. Under these conditions, Coro1A expression was strikingly less. (Fig.9F). This
539 effect is restricted at the protein level, as the transcript of Coro1A was upregulated on UBC9
540 knockdown (Fig.S7D). To investigate the route of Coro1A-GFP $^{V155K}$ degradation, RAW264.7
541 cells transfected with Coro1A-GFP $^{WT}$ and $^{V155K}$ mutant were treated with MG-132 and
542 Bafilomycin-A1. Surprisingly, partial rescue was observed in Coro1A-GFP $^{V155K}$ in both
543 conditions (Fig.9G). Altogether, these results show that disruption of the SIM site or lowering
544 global SUMOylation leads to degradation of the Coro1A protein, indicating that Coro1A depends
545 on SUMO2/3 and SUMOylated target protein for stability.
546
547• **Coro1A interacts with SUMOylated Raftlin-1 through SIM interaction**
548 To identify potential SUMOylated proteins involved in the SIM-SUMO interaction with Coro1A,
549 two distinct bands of SUMO2/3, observed between 75 kD and 150 kD (Fig. 9A, Top), were
550 subjected to mass spectrometry. After subtracting proteins detected in IgG, a list of potential
551 proteins that may undergo SUMOylation was obtained (Fig. 10A).
552 From that list, Raftlin, a novel major lipid raft protein, was selected as a promising candidate to
553 undergo SUMOylation and interact with Coro1A. Previous reports have shown that Raftlin
554 controls T-cell receptor (TCR) and B-cell receptor (BCR) signaling by mobilizing calcium ions
555 (Kazuko Saeki & Akihiko Yoshimura, 2003; Saeki et al., 2009). Raftlin plays a critical role in
556 endocytosis, decorates signaling endosomes, and is detected together with Coro1A in the VEGFR2
557 interactome (Tatematsu et al., 2016; Watanabe et al., 2011a; Bayliss et al., 2020). These findings
558 indicate a close association between Raftlin and Coro1A, and, together with their functional
559 similarity, led us to select Raftlin as a potential candidate for the Coro1A SIM-SUMO interaction.
560 To test the interaction between Coro1A and Raftlin, co-immunoprecipitation (co-IP) was
561 performed using an anti-Coro1A antibody in J774 $^{WT}$ and J774 $^{Coro1A\ KD}$ cell lysates. Raftlin-
562 Coro1A interaction appeared in J774 $^{WT}$, but not in J774 $^{Coro1A\ KD}$ (Fig. 10 B). Furthermore, their
563 interaction was validated in RAW264.7 cells, confirming its conservation across different cell
564 types (Fig. S7E). To identify potential SUMOylation sites present in Raftlin, the GPS-SUMO and
565 JASSA software tools were employed. Both software tools with high scores identified the K31 and
566 K224 sites (Fig. 10C). To narrow down on the possible SUMOylation site, an *in-silico* protein-
567 protein docking approach was employed. While docking the SUMO2 protein on the alpha fold
568 predicted structure of Raftlin, parameters like supramolecular geometry, accessibility of lysine (K)

569 residues for isopeptide bond formation with SUMO, and minimal energy score were considered.
570 Molecular docking demonstrated interaction between the di-glycine motif of SUMO2 (G-97) with
571 K31, K139, and K308 of Raftlin, with SUMO2-K31 interaction being most compact and exhibiting
572 the lowest minimum energy score (Fig. 10D). Additionally, multiple sequence alignment revealed
573 that K31 is highly conserved across different species, underlining its functional importance
574 (Fig.S7F) whereas other mentioned sites are not conserved. To test whether Raftlin undergoes
575 SUMOylation and whether K31 is the potential site of SUMO binding, SDM was performed to
576 substitute lysine (K31) with arginine (K31R), as SUMO can form an isopeptide bond with only
577 lysine and not with arginine (Rytinki & Palvimo, 2009). Next, RAW264.7 cells were transfected
578 with Raftlin $^{WT}$ and Raftlin $^{K31R,}$ along with appropriate controls, and subjected to GFP-antibody-
579 based pull-down. Immunoblot revealed a prominent interaction between Raftlin $^{WT}$ and SUMO2/3,
580 as well as between Raftlin $^{WT}$ and Coro1A. In contrast, Raftlin $^{K31R}$ did not interact with SUMO2/3
581 and showed a feeble interaction with Coro1A (Fig. 10E). Raftlin $^{K31R}$ showed comparable stability
582 to Raftlin $^{WT}$ as demonstrated by immunoblotting (Fig. S7G). In line with this, structured
583 illumination microscopy (SIM) demonstrated strong colocalization of Coro1A (Red) with Raftlin
584 $^{WT}$ (Green), which was markedly reduced with Raftlin $^{K31R}$ (Fig. 10F). To map the interacting
585 interface of SUMOylated Raftlin with Coro1A, a stable Raftlin-SUMO complex was docked on
586 Coro1A (PDB ID: 2AQ5). Protein-protein docking analysis indicated that SUMO interacts with
587 Coro1A through a region spanning residues 155-159 and 167-171. The SUMO-interacting
588 interface on Coro1A is highlighted in yellow (Fig.10G). Notably, these regions correspond to
589 SUMO-interacting motifs (SIMs) of Coro1A, consistent with our previous findings demonstrating
590 that SIM 155-159 is critical for Coro1A to interact with SUMO2/3 and maintain stability. Overall,
591 these results revealed that Coro1A interacts with SUMOylated Raftlin at K31 through the SIM
592 site.
593
594 **Discussion:**
595 In the current work, a screen was carried out to assess the possible involvement of SUMOylation
596 machinery components in CAC, leading to the identification of the deSUMOylase- SENP5. To
597 dissect the contribution of SENP5 in CAC, its interactome was analyzed, and Coro1A emerged as
598 an outcome. Coro1A, an actin-binding regulatory protein, is associated with immune cell function
599 but has not been explored in the context of IBD or CAC (Humphries et al., 2002; Mueller et al.,

600 2008; Pick et al., 2017; Stocker et al., 2018 ). However, increased expression of Coro1A has been
601 reported in several chronically inflamed and autoimmune disease models, such as renal fibrosis,
602 lupus nephritis, and lung fibrosis, as well as in some forms of cancer (X. Deng et al., 2024; Elihamu
603 et al., 2025; Kros et al., 2024; Nicolaou et al., 2020; Niu et al., 2024; Siegmund et al., 2016). In
604 lung adenocarcinoma, increased expression of Coro1A correlated with TNM stage, ranked among
605 the top 10 prognostic markers, particularly as an M2 or TAM macrophage marker, and appeared
606 to shape the tumor microenvironment (TME) (Z. Li et al., 2025; Sun et al., 2024) (Bao et al., 2022;
607 Y. Zhou et al., 2021). Coro1A expression is linked to cancer pathogenesis, since knockdown of
608 Coro1A curbs the growth and metastasis of breast cancer cells (Elihamu et al., 2025; He et al.,
609 2018; Jeon et al., 2024; Kros et al., 2024). Likewise, Coro 1A has been identified as one of the
610 five robust biomarkers in bladder cancer (Kumar et al., n.d.).

611 A direct interaction of Coro1A with the C-terminus of $\beta_2$ integrins is required
612 for polymorphonuclear leukocyte (PMNs) trafficking, adhesion, and post-adhesion events (Pick et
613 al., 2017). Furthermore, in a cystic fibrosis model, Coro1A was shown to regulate integrin
614 clustering and activation, a mechanism required for monocyte function (Younis et al., 2024). The
615 immune regulatory function of Coro 1A is exemplified by the finding linking Coro 1A to allograft
616 tolerance. Specifically, T cells lacking Coro1A suppressed the allograft rejection phenotype in a
617 wild-type host upon adoptive transfer, while maintaining T cell-specific responses against the
618 pathogen (Jayachandran et al., 2019). Likewise, Coro1A $^{KO}$ mice display attenuated response in
619 an experimental model of encephalomyelitis (Jayachandran et al., 2019; Kaminski et al., 2011).
620 Overall, these reports make it evident that several aspects of immune cell function, including
621 maintenance of numbers, trafficking, adhesion, and post-adhesion events, are directly governed by
622 Coro 1AMueller et al., 2008; Ndinyanka Fabrice et al., 2025; Pick et al., 2017; Shiow et al., 2009;
623 Younis et al., 2025) (Siegmund et al., 2016).

624 Arguably, these phenotypes result from significant signaling alterations in these cells, with
625 Coro1A function playing a direct role. Coro1A was shown to regulate TGF-βR signaling in an
626 experimental autoimmune encephalomyelitis (EAE) model. Coro1A$^{KO}$ mice exhibited less severe
627 EAE. Unexpectedly, upon re-induction of EAE, Coro1A$^{KO}$ mice showed severe disease, with a
628 strong correlation with IL-17-producing T cells. Coro1A$^{KO}$ Th17 cells show a severe defect in
629 TGF-βR-mediated SMAD3 activation, leading to increased IL-17 secretion (Kaminski et al.,

630 2011). TGF-β and IL-4 are key inducers of M2 macrophages and systemic immune suppression.
631 TGF-β promotes immune suppression in T cells, Dendritic cells (DCs), neutrophils, and
632 macrophages via canonical (SMAD2/3-dependent) and non-canonical pathways. TGF-β signaling
633 hampers DC maturation and antigen-presenting capacity by modulating co-stimulatory molecule
634 expression. In T-Cells, TGF-β suppresses TCR-induced cell proliferation and regulatory T cell
635 differentiation by inducing Foxp3. TGF-β also polarizes neutrophils towards the pro-tumorigenic
636 N2 phenotype. Given the broad immunosuppressive effects of TGF-β, we hypothesize that Coro1A
637 may regulate these TGF-β-induced processes in immune cells, as we have demonstrated in
638 macrophages (Z. Deng et al., 2024b; Fridlender et al., 2009; Gong et al., 2012a; C. S. Lin et al.,
639 2013; Mckarns et al., 2004; Strobl & Knapp, 1999).

640 Owing to TGF-β signaling's multifaceted functions, mutations in components have also
641 been linked to colorectal cancer, particularly in the tumor microenvironment (TME). Genetic
642 alterations in genes encoding components of the TGF-β signaling pathway, particularly TGF-βRII
643 (50-60%) and SMAD4 (46-48%), are the most common in CAC cases (Calon et al., 2012; Means
644 et al., 2018; Yashiro, 2014). In CAC macrophages, characterized as $CD11b^+$ $F4/80^+$ $Ly6C^+$, are
645 increased and play a crucial role in tumorigenesis; their depletion halts tumorigenesis. Highly
646 plastic macrophages under persistent chronic conditions polarize towards an M2-like phenotype
647 and act as a key driver of the CAC (Hardbower et al., 2017; Sheng et al., 2022; Shin et al., 2023;
648 Wang et al., 2023; Yuan et al., 2021).

649 Interestingly, polymorphisms in TGF-β Receptors and/or signaling components have been
650 reported to be associated with a concomitant decrease in the $CD11b^+$ $F4/80^+$ M2 macrophage
651 population (Gong et al., 2012). In line with this, in the current work, we observed that Coro1A is
652 a potent regulator of TGF-β signaling in macrophages in CAC. Myeloid cells play a key role in
653 shaping TME, and TGF-β signaling is essential for myeloid cell function in CAC (Chan et al.,
654 2022). Furthermore, TGF-β-deficient mice exhibit significantly reduced CAC burden, lower tumor
655 burden, and substantially reduced IL-6 and TNF-α production (J. Li et al., 2013; W. Wang et al.,
656 2015). This phenotype closely matches our observation in $Coro1A^{KO}$ mice, which show reduced
657 TGF-β signaling and fewer tumors. The integral role of Coro1A in immune cell function and TGF-
658 β signaling also strongly connects to fibrosis and the mechanisms that contribute to it. The c-AMP-
659 responsive element-binding protein (CREBH) controls Coro1A expression and regulates

660 autophagy in NASH, thereby preventing liver fibrosis. CREBH$^{KO}$ mice exhibit liver fibrosis by
661 activating TGF-β, CTGF signaling pathways, and deposition of collagen, α-SMA, and fibronectin
662 (Deng et al., 2024).An extensive clinical study involving colorectal cancer patients (N=94) showed
663 that overexpression of markers of cancer-associated fibroblasts was associated with tumor-
664 infiltrating lymphocytes, thus revealing a vital role for CAFs in maintaining the colorectal TME
665 (Zadka et al., 2021). In our study, Coro1A$^{KO}$ mice showed resistance to polyp formation in an
666 AOM-DSS model, with significantly reduced markers of fibrosis, accompanied by attenuated
667 proliferation, oncogene, and EMT gene activation. The connection between Coro1A and fibrosis
668 and tumorigenesis was through its regulation of TGF-β signaling. Mechanistically, Coro1A-
669 mediated mobilized calcium activates Calcineurin phosphatases, which, in turn, activate genes
670 involved in preventing lysosomal fusion of phagosomes and signaling endosomes(Jayachandran
671 et al., 2007; Suo et al., 2014). In our study, we also found Coro1A employing the same calcium-
672 calcineurin pathway to protect the TGF-β signaling endosome from lysosomal degradation.

673 The fascinating part of the work is how SUMOylation of Raftlin protein bridges these
674 diverse pathways. We observed that Coro1A depends on SUMOylated Raftlin for stability via the
675 SUMO-SIM interaction. SIM-deficient Coro1A undergoes rapid degradation, leading to
676 concomitant dysregulated TGF-β signaling. Raftlin and Coro1A exhibit a functional correlation.
677 Like Coro1A, Raftlin also controls B-cell receptor (BCR) and T-cell receptor (TCR) signaling by
678 modulating calcium mobilization, and both are key players in clathrin-mediated endocytosis, a
679 common pathway utilized by TGF-β signaling endosomes to initiate signaling. Given their
680 functional correlation, our finding highlights SUMO as a connecting link between Coro1A and
681 Raftlin (Bayliss et al., 2020; Kazuko Saeki & Akihiko Yoshimura, 2003; Saeki et al., 2009;
682 Tatematsu et al., 2016; Watanabe et al., 2011) (Lacy et al., 2018). Presumably, SENP5 plays a role
683 in Raftlin SUMOylation, an attractive area for future research. Overall, our study revealed a critical
684 role of Coro1A in shaping the tumor microenvironment in CAC by modulating TGF-β signaling
685 and promoting a M2-like non-inflammatory macrophage phenotype.

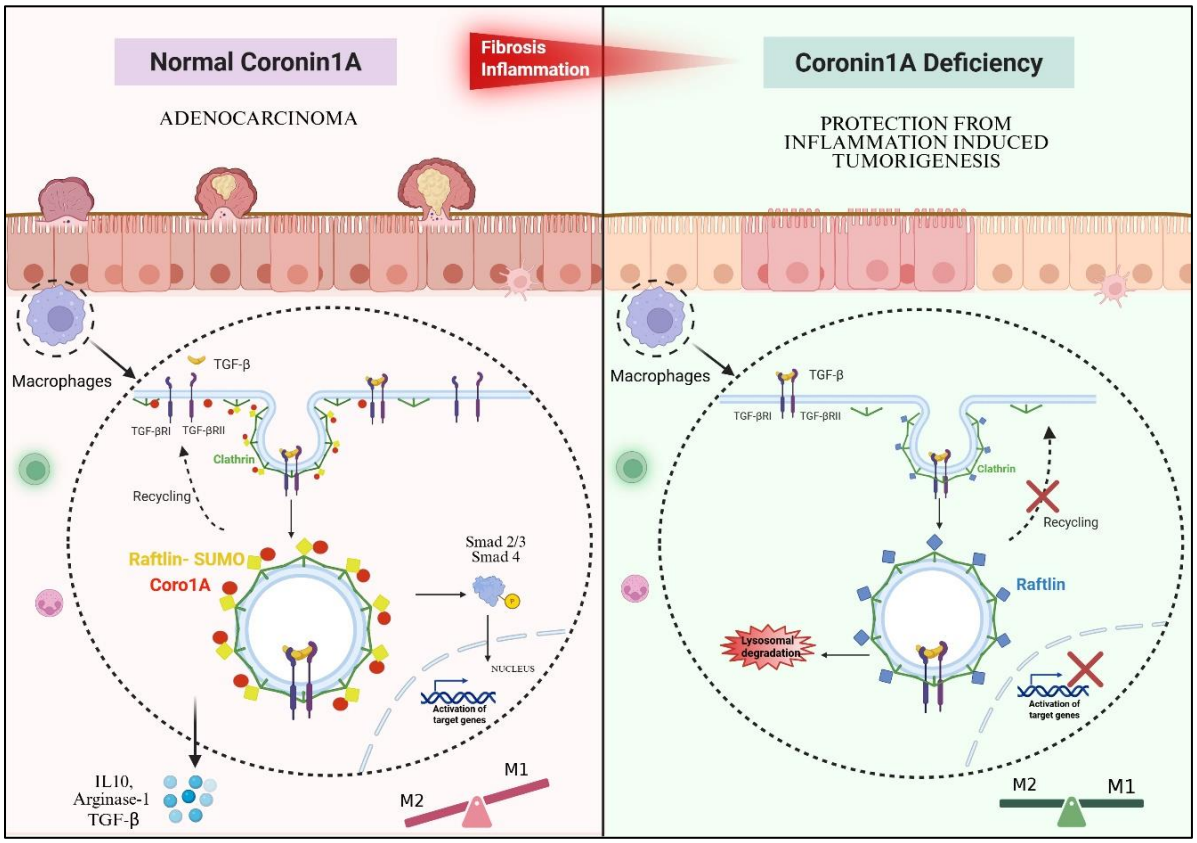


**Figure 11.** Graphical Summary demonstrating the role of Coro1A in regulating TGF-β signaling and modulating tumor microenvironment.

697 **Figure legends:**

698 **Dynamic expression pattern of SENP5 in chronic colitis and colitis-associated colorectal**
699 **cancer (CAC)**

700 A. Schematic representation of the chemically induced murine CAC model (AOM-DSS) in
701 C57BL/6 mice.

702 B. The graph represents the body weight of experimental animals during the development of
703 the AOM-DSS model.

704 C. A representative image showing the gross morphology of the colon. The graph on the right
705 shows the quantification of colon length. White arrows indicate polyps present at the distal end of
706 the colon.

707 D. A representative image shows the gross morphology of the spleen. The graph to the right
708 shows the spleen weight-to-body weight ratio in the mice.

709 E. Representative Hematoxylin and Eosin-stained colon section from Control, CC, non-polyp,
710 and polyp.

711 F. Immunoblot of SUMO-1 and SUMO-2/3 conjugated proteins (global SUMOylome) from
712 colonic tissue lysates of chronic colitis (CC) and polyps from the murine CAC model, with free
713 SUMO is shown in the red box.

714 G. Heatmap qRT-PCR-based fold change expression of deSUMOylases SENP1, SENP2,
715 SENP3, SENP5, SENP6, and SENP7 in CC, non-polyp, and polyp regions of the CAC murine
716 model relative to the average control values.

717 H. Immunoblot showing SENP5 expression in lysates from colonic tissue of Control, CC,
718 non-polyp, and polyp samples. The graph at the bottom shows the densitometric analysis of the
719 fold intensity of SENP5 expression, normalized to the loading control.

720 I. Immunoblot of SUMO-1 and SUMO-2/3 conjugated proteins (global SUMOylome) from
721 tissue lysates of CAC patient samples with free SUMO is shown in the red box.
722 J. qRT-PCR-based fold change expression of deSUMOylase SENP5 from SCRC (N=9) and
723 CAC (N=15) patient samples relative to the average IBS values (N=10).
724 K. Immunoblot showing SENP5 expression in colonic biopsies from control and CAC
725 patients. The graph at the bottom shows the densitometric analysis of the fold intensity of SENP5
726 expression, normalized to the loading control.
727 L. Immunoblot showing SENP5 expression in colonic tissue lysates of Control, non-polyp
728 SCRC, and polyp SCRC of $Apc^{+/+}$ and $APC^{+/-}$ model. The graph at the bottom shows the
729 densitometric analysis of the fold intensity of SENP5 expression, normalized to the loading
730 control.
731 Each dot represents (C, D, H, and L) for one mouse, (J) for one patient, and (K) lysate from one
732 patient biopsy. Each box represents one mouse (G). Actin was used as a loading control for F, H,
733 and L, and GAPDH was used as a loading control for I and K. GAPDH was used for gene
734 normalization (G and J). The immunoblots shown here are representative of three biological
735 replicates. Error bars represent mean ±SEM. Statistical analysis performed using the unpaired
736 Student's t-test, with a p-value <0.05 considered statistically significant. *<0.05, **<0.01,
737 ***<0.001, ****<0.0001, ns: non-significant.
738
739 Figure-2
740 **Altered interactome of SENP5 in chronic colitis and colitis-associated colorectal cancer**
741 A. Schematic representation of SENP5 pull-down using anti-SENP5 antibody from Control, CC,
742 non-polyp, and polyp tissue lysates. Isotype antibody (IgG) was used as a negative control.

743 B. Venn diagram showing the number of unique and common proteins across the Control, CC,
744 non-polyp, and polyp groups.
745 C. The Gene Ontology (GO) Pathway analysis (molecular function) of differentially enriched
746 SENP5 interacting proteins in the non-polyp and polyp region, as compared to the Control.
747 Pathway enrichment significance was assessed using hypergeometric and multiple test
748 correction at FDR less than 0.05.
749 D. Table of shortlisted potential SENP5 interacting proteins from the Actin binding function
750 pathway based on their functional role in cancer or any disease progression, and having a
751 SUMO binding or interacting motif.
752 E. Volcano plot of differentially enriched proteins with SENP5 in non-polyp and polyp as compared
753 to the Control, with shortlisted potential SENP5 interactors marked. Here, significance is defined
754 as fold change >2 and p-value < 0.05.
755
756 Figure-3
757 **Coro1A as an interactor of SENP5**
758 A. Top: Colonic tissue lysates of Control, CC, non-polyp, and polyp were immunoprecipitated with
759 anti-SENP5 antibody and immunoblotted for Coro1A. Bottom: 10% of input loaded from the
760 same tissue lysate and immunoblotted for Coro1A and Actin. Isotype antibody (IgG) was used
761 as a negative control.
762 B. Immunoblot showing Coro1A expression in colonic tissue lysates of Control, CC, non-polyp,
763 and polyp. The graph on the right shows densitometric analysis of fold intensity of Coro1A
764 expression, normalized to loading control.

765 C. Immunoblot showing Coro1A expression in colonic tissue lysates from Control, CC, and CAC
766 colon of an AOM-DSS model performed in IL-10$^{-/-}$ mice. The graph on the right shows
767 densitometric analysis of fold intensity of Coro1A expression, normalized to loading control.
768 D. Immunoblot showing Coro1A expression in human colonic biopsies of IBS (N=4) and ulcerative
769 colitis (N=5) patients. The graph on the right shows densitometric analysis of fold intensity of
770 Coro1A expression, normalized to loading control.
771 E. Immunohistochemistry of Coro1A in colonic tissue sections of Control, CC, non-polyp, and
772 polyp region of AOM-DSS mice model. Scale bar 100µm.
773 F. Immunohistochemistry of Coro1A in archived colonic biopsy slides from IBS, UC, and CAC
774 patients. Scale bar 100µm.
775 Each dot represents (B and C) one mouse or (D) one patient biopsy tissue lysate. Actin was used
776 as a loading control (A and B), and GAPDH was used as a loading Control (C and D). The inset
777 shows a zoomed image of a colon section. Asterisks show Coro1a expression (E and F). The
778 immunoblots shown here are representative of three biological replicates.
779 Error bars represent mean ±SEM. Statistical analysis performed using the unpaired Student's t-
780 test, with a p-value <0.05 considered statistically significant. *<0.05, **<0.01, ***< 0.001,
781 ****<0.0001, ns: non-significant.
782
783 Figure-4
784 **Absence of Coro1A confers resistance to CAC development in mice:**
785 A. Schematic representation of the chemically induced murine CAC model (AOM-DSS) in WT
786 (C57BL/6) and Coro1 A $^{KO}$ (C57BL/6) mice.

787 B. Representative longitudinal cut-open colon image from the CAC group of WT and Coro1A $^{KO}$

788 mice. White arrows indicate polyps present at the distal end of the WT colon.

789 C. Representative Hematoxylin and Eosin-stained colon section from Control, CC, and CAC group

790 of WT and Coro1A $^{KO}$ mice.

791 D. Representative Sirius Red-stained colon section from Control, CC, and CAC group of WT and

792 Coro1A$^{KO}$ mice.

793 E. qRT-PCR-based fold change expression of Proliferation and Oncogene; Ki67 and C-Myc

794 relative to the average control values.

795 F. qRT-PCR-based fold change expression of pro-inflammatory and anti-inflammatory markers,

796 COX-2 and Arginase-1, relative to the average control values.

797 G. qRT-PCR-based fold change expression of ECM markers, Fibronectin, α-SMA, and Col1A1

798 relative to the average control values.

799 H. qRT-PCR-based fold change expression of p53 relative to the average control values.

800 Each dot represents one of the mice (E, F, G, and H). Samples analyzed by qRT-PCR include

801 CC $^{WT}$, CAC $^{WT}$, CC $^{Coro1A\ KO}$, and CAC $^{Coro1A\ KO}$. GAPDH was used for Gene normalization

802 (E, F, G, and H). Error bars represent mean ± SEM. Statistical analysis performed using the

803 unpaired Student's t-test, with a p-value <0.05 considered statistically significant. *<0.05,

804 **<0.01, ***< 0.001, ****<0.0001, ns: non-significant.

805

806 Figure -5

807 **Increased expression of Coro 1A is associated with M2 macrophages.**

808 A. Representative counter plots showing F4/80$^{+}$ and CD11b$^{+}$ macrophage infiltration in Control,

809 CC, non-polyp, and polyp regions.

810 B. Percentage infiltration of macrophages in Control, CC, non-polyp, and polyp as determined by
811 flow cytometry.
812 C. Median Fluorescence intensity (MFI) of Coro1A in infiltrated macrophages across Control, CC,
813 non-polyp, and polyp as measured by flow cytometry.
814 D. Representative plot showing the distribution of $iNOS^+$ (%) and Arg-$1^+$ (%) macrophages across
815 Control, CC, non-polyp, and polyp.
816 E. Ratio of M2 (Arg-$1^+$) to M1 ($iNOS^+$) macrophages in all four conditions: Control, CC, non-
817 polyp, and polyp, as determined by flow cytometry.
818 F. MFI of Coro1A in Arg-$1^+$ macrophages across Control, CC, non-polyp, and polyp.
819 G. Immunoblot showing expression of Coro1A in bone-marrow-derived macrophages (BMDMs)
820 cells treated with IL-4 for 16, 18, and 20 hours. The graph on the right shows the densitometric
821 analysis of the fold intensity of Coro1A expression, normalized to the loading control.
822 H. Immunoblot showing expression of Coro1A in RAW 264.7 cells treated with TGF-β for 2,3, and
823 4 hours. The graph on the right shows the densitometric analysis of the fold intensity of Coro1A
824 expression, normalized to the loading control.
825 I. qRT-PCR analysis showing fold-change expression of M1(iNOS and IL-8) and M2 (Arg-1,
826 YM1, and Mrc1) macrophage markers in BMDMs treated with IL-4.
827 J. qRT-PCR analysis showing fold-change expression of M2 macrophage markers, Arginase-1, and
828 SNAIL in RAW264.7 cells treated with TGF-β.
829 K. Quantification of TGF-β levels in colonic tissue lysates from AOM-DSS mice, measured by
830 ELISA.

831 Each dot represents (B, C, E, F, and K) one mouse, or (G, H, I, and J) independent experiments
832 of 3 biological replicates. Actin is used as a loading control (G and H). GAPDH used for Gene

833 normalization (I and J). The immunoblots shown here are representative of three biological
834 replicates. Error bars represent mean ± SEM. Statistical analysis performed using the unpaired
835 Student's t-test, with a p-value <0.05 considered statistically significant. *<0.05, **<0.01, ***<
836 0.001, ****<0.0001, ns: non significant.
837
838 Figure-6

839 **Coro1A interacts with TGF-β receptors directly and controls TGF-β-mediated M2**
840 **macrophage polarization.**

841 A. Top: RAW264.7 cell lysates immunoprecipitated with anti-Coro1A antibody and
842 immunoblotted for TGF-βRI. Bottom:10% of input loaded from the same cell lysate and
843 immunoblotted for Coro1A, TGF-βRI, and Actin. Isotype antibodies (IgG) were used as a
844 negative control.
845 B. Representative structured illumination microscopy (SIM) showing cellular localization of
846 TGF-βRI (Red) and Coro 1A (Green). The asterisks in the zoomed version of the merged image
847 show colocalization of TGF-βRI (Red) and Coro1A-GFP (Green).
848 C. Immunoblot confirming loss of Coro1A protein expression in stable J774 $^{\text{Coro1A KD}}$ cells
849 compared to J774$^{\text{WT}}$ cells.
850 D. Top: J774 $^{\text{WT}}$ and J774 $^{\text{Coro1A KD}}$ cell lysates immunoprecipitated with anti-Coro1A antibody
851 and immunoblotted for TGF-βRI. Bottom: 10% of input loaded from cell lysate and
852 immunoblotted for Coro1A, TGF-βRI, and Actin. Isotype antibodies (IgG) were used as a
853 negative control.
854 E. qRT-PCR-based fold-change expression of Arginase-1 (left) and SNAIL (right) in J774 $^{\text{WT}}$ and
855 J774 $^{\text{Coro1A KD}}$ cells with and without TGF-β stimulation.

856 F. Concentration analysis of IL-10 in the cell culture supernatant of J774 $^{WT}$ and J774$^{Coro1A\ KD}$
857 cells with and without TGF-β stimulation using ELISA.
858 G. Flow cytometry-based analysis of Arginase-1 positive cells in J774 $^{WT}$ and J774 $^{Coro1A\ KD}$ cells
859 with and without TGF-β stimulation.
860 H. qRT-PCR-based fold-change expression of TGF-βRI in J774 $^{WT}$ and J774 $^{Coro1A\ KD}$ cells with
861 and without TGF-β stimulation.
862 I. Immunoblot showing nuclear accumulation of SMAD3 post 30 and 60 minutes of TGF-β
863 exposure to J774 $^{WT}$ and J774 $^{Coro1A\ KD}$ cells.
864 J. Representative confocal images of BMDM $^{WT}$ and BMDM $^{Coro1A\ KO}$ cells with and without
865 TGF-β stimulation, stained for pSMAD3 (Red). A dotted white circle demarks nuclear
866 boundaries. The graph to the right illustrates the mean fluorescence intensity of pSMAD3 in
867 the nuclei (n = 60). (Scale bar = 5μm).
868 Each dot represents (E, F, G, and H) one independent experiment of a biological experiment,
869 and (J) one cell. Actin was used as a loading control (A, C, and D). Lamina AC was used as a
870 loading control (I), GAPDH was used for Gene normalization (E and H). The immunoblots shown
871 here are representative of three biological replicates. Error bars represent mean ± SEM. Statistical
872 analysis performed using the unpaired Student's t-test, with a *p*-value <0.05 considered
873 statistically significant. *<0.05, **<0.01, ***<0.001, ****<0.0001, ns: non-significant.
874
875
876
877
878

879 Figure-7

880 **Coro1A is required for the stability of TGF-βRI**

881 A. Immunoblot showing TGF-β R1 expression in J774 $^{WT}$ and J774 $^{Coro1A\ KD}$ cells. The graph at
882 the bottom shows densitometric analysis of the fold intensity of TGF-βRI, normalized to the
883 Control.

884 B. Representative confocal image of BMDM $^{WT}$ and BMDM $^{Coro1A\ KO}$ cells stained for TGF-
885 βRI (Green) (n=100). The graph on the right shows the quantification of TGF-βRI mean
886 fluorescence intensity. (Scale bar=5μm).

887 C. Immunoblot showing pAKT and AKT expression in J774 $^{WT}$ and J774 $^{Coro1A\ KD}$ cells. The graph
888 at the bottom shows the desitometric analysis of the fold intensity of pAKT, normalized to the
889 AKT.

890 D. Concentration analysis of TGF-β in the cell culture supernatant of J774 $^{WT}$ and J774 $^{Coro1A\ KD}$
891 cells using ELISA.

892 E. Concentration analysis of TGF-β from the tissue lysates of WT and Coro1A $^{KO}$ CAC (AOM-
893 DSS) mice model.

894 F. Immunoblot showing TGF-βRI expression in J774$^{WT}$ and J774$^{Coro1A\ KD}$ cells with and without
895 Bafilomycin-A1 treatment (100nM). The graph at the bottom shows densitometric analysis of
896 TGF-βRI, normalized to the Control.

897 G. Representative confocal images of BMDM $^{WT}$ and BMDM $^{Coro1A\ ko}$ cells stained for TGF-βRI
898 (Green) using anti-TGF-βRI antibody and Lysosomes with LysoTracker Red DND-99 (Red).
899 The graph at the bottom illustrates the quantification of colocalization between TGF-βRI and
900 Lysosomes, as determined from images (n=60), using Mander's overlap coefficient. (Scale
901 bar=5μm).

902 Each dot represents an independent experiment (A, C, D, and F), one cell (B and G), and one
903 mouse (E). Actin was used as a loading control (A and F), and GAPDH was used as a loading
904 control (C). The immunoblots shown here are representative of three biological replicates.
905 Error bars represent mean ± SEM. Statistical analysis performed using the unpaired Student's
906 t-test, with a p-value <0.05 considered statistically significant. *<0.05, **<0.01, ***< 0.001,
907 ****<0.0001, ns: non-significant.

908 Figure-8

909 **Coro1A utilizes calcium-calcineurin signaling to protect TGF-βRI from lysosomal**
910 **degradation.**

911 A. Immunoblot showing TGF-βRI expression in RAW 264.7 cell lysate after treatment with
912 BAPTA-AM (10 μM). The graph on the right shows densitometric analysis of fold intensity of
913 TGF-βRI, normalized to the loading Control.

914 B. Immunoblot showing TGF-βRI expression in J774 $^{WT}$ and J774 $^{Coro1A\ KD}$ cell lysates post-
915 treatment with Inomycin (3.5 μM). The graph on the right shows densitometric analysis of fold
916 intensity of TGF-βRI, normalized to the loading Control.

917 C. Immunoblot showing TGF-βRI expression in RAW264.7 cell lysate post-treatment with
918 Cyclosporin A (CsA) (6 μM). The graph on the right shows densitometric analysis of fold
919 intensity of TGF-βRI, normalized to the loading Control.

920 D. Immunoblot showing TGF-βRI expression in RAW 264.7 cell lysate post-treatment with FK506
921 (3 μM). The graph on the right shows densitometric analysis of fold intensity of TGF-βRI,
922 normalized to the loading Control.

923 Each dot represents an independent biological replicate (A, B, C, and D). As a loading control,
924 Actin was used (A, B, C, and D). The immunoblots shown here are representative of three

925 biological replicates. Error bars represent mean ± SEM. Statistical analysis performed using the
926 unpaired Student's t-test, with a p-value <0.05 considered statistically significant. *<0.05,
927 **<0.01, ***< 0.001, ****<0.0001, ns: non-significant.

928 Figure-9

929 **SUMO2/3 governs the stability of Coro1A**

930 A. Top: J774$^{WT}$ cell lysates immunoprecipitated with anti-Coro1A antibody and immunoblotted
931 for SUMO2/3. Bottom: reverse Co-IP using anti-SUMO2/3 antibody from the same lysates and
932 probed for Coro1A with 10% of input loaded and immunoblotted for Coro1A, SUMO2/3, and
933 Actin. Isotype antibodies (IgG) were used as a negative control.

934 B. The table represents possible SIM sites in Coro 1A as predicted by software programs GPS-
935 SUMO and JASSA. SIM sites predicted by both the software are highlighted in yellow.

936 C. Immunoblot showing Coro1A-GFP $^{WT}$ and SIM mutants (V124K, V155K, V167K) fusion
937 protein expression in transfected RAW264.7 cells. The graph at the bottom shows
938 densitometric analysis of the fold intensity of Coro1A-GFP, normalized to the loading control.

939 D. Immunoblot showing Coro1A -GFP $^{WT}$ and SIM mutants (V155K, V155A) fusion protein
940 expression in transfected RAW264.7 cells. The graph on the right shows densitometric
941 analysis of the fold intensity of Coro1A-GFP, normalized to the loading control.

942 E. Representative confocal images of Coro1A-GFP $^{WT}$ and SIM mutants (V124K, V155K,
943 V167K ) fusion protein expression in transfected RAW264.7 cells. (Scale bar =5μm).

944 F. Immunoblot showing Coro1A and UBC9 expression upon siRNA-mediated UBC9
945 knockdown in RAW264.7 cells. The graphs at the bottom show densitometric analysis of the
946 fold intensity of Coro1A and UBC9, normalized to the loading control.

947 G. Immunoblot showing expression of Coro1A-GFP $^{WT}$ and SIM mutant (V155K) fusion protein
948 expression in RAW264.7 cells with and without treatment of MG-132 (20 μM) and
949 Bafilomycin-A1 (100 nM).

950 Each dot represents an independent experiment (C, D, and F) of biological replicates. Actin
951 was used as a loading control (A, C, D, F, and G). The immunoblots shown here are
952 representative of three biological replicates. Error bars represent mean ± SEM. Statistical
953 analysis performed using the unpaired Student's t-test, with a p-value <0.05 considered
954 statistically significant. *<0.05, **<0.01, ***< 0.001, ****<0.0001, ns: non-significant.

955 Figure-10

956 **Coro1A interacts with SUMOylated Raftlin-1 through the SIM site**

957 A. The table lists putative SUMOylated proteins identified by mass spectrometry.

958 B. Top: J774$^{WT}$ and J774$^{Coro1A\ KD}$ cell lysates immunoprecipitated with anti-Coro1A antibody and
959 immunoblotted for Raftlin. 10% of the input was loaded from the same cell lysate and probed
960 for Raftlin, Coro1A, and Actin. Isotype antibody (IgG) was used as a negative control. Actin
961 was used as a loading control.

962 C. The table shows the possible SUMOylation sites in Raftlin, as predicted by GPS-SUMO and
963 JASSA. SUMoylation sites predicted by both software are highlighted in yellow.

964 D. Computational molecular docking of the alphafold structure of Raftlin and SUMO 2 using
965 HADDOCK2.4. web server. Alpha fold structure of Raftlin (Grey) and SUMO2 is (Magenta).
966 K31, the SUMO binding site is highlighted in Red.

967 E. Top: Raftlin$^{WT}$, Raftlin $^{K31R}$, and Vector control transfected into RAW264.7 cell lysates were
968 immunoprecipitated with an anti-GFP antibody and immunoblotted for SUMO2/3, Coro1A,
969 and GFP. Bottom: 10% of the input was loaded from the same cell lysate and probed for Raftlin,

970 Coro1A, Actin, and SUMO2/3. Isotype antibody (IgG) was used as a negative control. Actin
971 was used as a loading control.
972 F. Representative images of structured illumination microscopy displaying images of transfected
973 RAW264.7 cells with Raftlin$^{WT}$ and Raftlin $^{K31R}$ (Green) stained with Coro1A (Red) using anti-
974 Coro1A antibody. The inset shows zoomed areas of images, marked with arrows, to illustrate
975 colocalization (scale bar = 5 μm).
976 G. Computational molecular docking of the crystal structure of Coro1A (2AQ5) and stable binary
977 structure of Raftlin and SUMO 2 performed using HADDOCK2. 4. 3-D structure of Coro1A
978 (Green), Raftlin-1 (Grey), and SUMO2 is Magenta, and SIM sites 155-159 and SIM 167-171
979 are in red. The area of SUMO2 interacting with Coro1A is highlighted in yellow.
980
981 **Figure 11**. Graphical Summary demonstrating the role of Coro1A in regulating TGF-β
982 signaling and modulating tumor microenvironment.
983
984 **Supplementary Figure 1**

985 A. qRT-PCR-based fold change expression of C-Myc from CC, non-polyp, and polyp tissue of
986 AOM-DSS mice model. GAPDH was used for gene normalization. Each dot represents one
987 mouse.
988 B. Schematic representation of the sporadic colorectal cancer (SCRC) model in Apc$^{+/+}$ and Apc
989 $^{+/-}$ mice.
990 C. Representative longitudinal cut-open colon image of Apc$^{+/+}$ and Apc$^{+/-}$ mice. Black arrows
991 indicate polyps present at the distal end of the colon.
992 Error bars represent mean ±SEM. Statistical analysis performed using the unpaired Student's t

993 test, with a p-value <0.05 considered statistically significant. *<0.05, **<0.01, ***< 0.001,
994 ****<0.0001, ns: non-significant.
995
996
997 **Supplementary Figure 2**
998 A. The Gene Ontology (GO) Pathway analysis (cellular component) of differentially enriched
999 SENP5 interacting proteins in the non-polyp and polyp region, as compared to the Control.
1000 Pathway enrichment significance was assessed using hypergeometric and multiple test
1001 correction at FDR less than 0.05.
1002 B. Volcano plot of differentially enriched proteins with SENP5 in CC as compared to the Control,
1003 with shortlisted potential SENP5 interactors marked. Here, significance is defined as fold
1004 change >2 and *p*-value < 0.05.
1005
1006 **Supplementary Figure 3**
1007 A. Schematic representation of the CAC (AOM-DSS) model in WT and IL10$^{-/-}$ mice.
1008 B. Schematic representation of the Acute colitis model (Day-7) in WT mice.
1009 C. Immunoblot showing Coro1A expression in lysates of colonic tissue from the acute colitis
1010 model. The graph on the right shows densitometric analysis of fold intensity of Coro1A
1011 expression, normalized to loading control.
1012 D. Immunoblot showing Coro1A expression in colonic tissue lysates of Control, non-polyp, and
1013 polyp (Apc$^{+/-}$)SCRC model. The graph on the right shows densitometric analysis of fold
1014 intensity of Coro1A expression, normalized to loading control.

1015 Each dot represents one mouse (C and D). Actin was used as a loading control (C and D). The
1016 immunoblots shown here are representative of three biological replicates. Error bars represent
1017 mean ±SEM. Statistical analysis performed using the unpaired Student's t-test, with a p-value
1018 <0.05 considered statistically significant. *<0.05, **<0.01, ***< 0.001, ****<0.0001, ns: non-
1019 significant.

1020 **Supplementary Figure 4**

1021 A. Representative immunoblot confirming loss of Coro1A protein expression in colonic tissue
1022 lysate of Coro1A $^{KO}$ mice compared to WT mice.

1023 B. Representative agarose gel image confirming the genotype of Coro1A $^{KO}$ mice (400bp).

1024 C. The graph represents the body weight of experimental animals during the development of the
1025 AOM-DSS model.

1026 D. A representative image showing the gross morphology of the colon from both genotypes (WT
1027 and Coro1A $^{KO}$). The graph at the bottom shows the quantification of colon length.

1028 E. A representative image showing the gross morphology of the spleen (Splenomegaly) from both
1029 genotypes (WT and Coro1A $^{KO}$). The graph at the bottom shows the quantification of spleen
1030 weight to the mice's body weight.

1031 F. Histopathological scoring of murine colon tissue sections was performed in a blinded manner
1032 by an experienced pathologist. Parameters such as collagen deposition, mascularis layer
1033 widening, crypt architecture distortion, and inflammation were scored as 0 (absent), 1(mild),
1034 and 2 (moderate). Field effect was scored as 0 (absent) and 1 (present), and dysplasia as 0
1035 (absent), 1 (low-grade dysplasia), and 2 (high-grade dysplasia).

1036 G. qRT-PCR-based fold change expression of E-Cadherin relative to the average control values.

1037 H. qRT-PCR-based fold change expression of EMT markers, SLUG, and SNAIL relative to the
1038 average control values.
1039 Each dot represents one mouse (D, E, F, and G). Samples analyzed by qRT-PCR include CC $^{WT}$,
1040 CAC $^{WT}$, CC $^{Coro1A\ KO}$, and CAC $^{Coro1A\ KO}$. GAPDH was used for Gene normalization (F and G).
1041 Error bars represent mean ± SEM. Statistical analysis performed using the unpaired Student's t-
1042 test, with a p-value <0.05 considered statistically significant. *<0.05, **<0.01, ***< 0.001,
1043 ****<0.0001, ns: non-significant.
1044
1045 **Supplementary Figure 5**
1046 A. Representative flow cytometry plots showing the gating strategy used for cell population
1047 identification and analysis, including a fluorescence-minus-one (FMO) control.
1048 B. Representative counter plots showing CD 45$^{+}$ and Ly6G$^{+}$ neutrophil infiltration in Control, CC,
1049 non-polyp, and polyp regions.
1050 C. Percentage infiltration of Neutrophils in Control, CC, non-polyp, and polyp as determined by
1051 flow cytometry.
1052 D. Median Fluorescence intensity (MFI) of Coro1A in infiltrated neutrophils across Control, CC,
1053 non-polyp, and polyp as measured by flow cytometry.
1054 E. MFI of Coro1A in iNOS$^{+}$ macrophages across Control, CC, non-polyp, and polyp.
1055 Here, each dot represents one mouse (B, C, D, and E). Error bars represent mean ± SEM.
1056 Statistical analysis performed using the unpaired Student's t-test, with a p-value <0.05
1057 considered statistically significant. *<0.05, **<0.01, ***< 0.001, ****<0.0001, ns: non-
1058 significant.
1059 **Supplementary Figure 6**

1060 A. Top: RAW264.7 cell lysates immunoprecipitated with anti-Coro1A antibody and
1061 immunoblotted for TGF-βRII. Bottom:10% of input loaded from the same cell lysate and
1062 immunoblotted for Coro1A, TGF-β RII, and Actin. Isotype antibodies (IgG) were used as a
1063 negative control.

1064 B. Representative confocal images of J774 $^{WT}$ and J774 $^{Coro1A\ KD}$ cells showing a marked reduction
1065 in the expression of Coro1A in J774$^{Coro1A\ KD}$ cells (Scale bar=5μm). Coro1a shows typical cortex-
1066 based localization in J774$^{WT}$ cells, which is absent in J774$^{Coro1A\ KD}$ cells. Actin was stained with
1067 Phalloidin to mark the cell boundaries.

1068 C. Immunoblot showing TGF-β secreted by J774 $^{WT}$ and J774 $^{Coro1A\ KD}$ cells in respective cell
1069 culture media. Ponceau image was used as a loading control. The graph at the bottom shows
1070 densitometric analysis of fold intensity of Coro1A expression, normalized to the loading control.

1071 D. Immunoblot showing TGF-β RI expression in J774 $^{WT}$ and J774 $^{Coro1A\ KD}$ cells with and without
1072 MG-132 treatment (20 μM). The graph on the right shows densitometric analysis of the fold
1073 intensity of TGF-βRI, normalized to the loading control.

1074 E. Representative immunoblot showing p62 expression in J774 $^{WT}$ and J774 $^{Coro1A\ KD}$ cells with
1075 and without Bafilomycin-A treatment (100 nM).

1076 F. Representative immunoblot showing poly-ubiquitination in J774 $^{WT}$ and J774 $^{Coro1A\ KD}$ cells with
1077 and without MG-132 treatment (20 μM).

1078 Each dot represents (C and D) one independent experiment of three biological replicates. Actin
1079 is used as a loading control (A, D, E, and F). The immunoblots shown here are representative of
1080 three biological replicates. Error bars represent mean ± SEM. Statistical analysis performed
1081 using the unpaired Student's t-test, with a p-value $<0.05$ considered statistically
1082 significant. *<0.05, **<0.01, ***< 0.001, ****<0.0001, ns: non-significant.

1083 **Supplementary Figure 7**

1084 A. Multiple sequence alignment of Coro1A protein sequences from eight mammalian species
1085 reveals that selected SIM sites are conserved (highlighted in a red rectangle).

1086 B. Table representing site-directed mutations performed in SUMO-interacting motifs (SIM) sites;
1087 Valine (V) of the SIM site replaced by Lysine (K).

1088 C. RMSF plots of Coro1A$^{WT}$ and Coro1A$^{V155K}$ mutant showing fluctuations of residues observed
1089 in molecular dynamics run by the CABS flex server.

1090 D. qRT-PCR-based fold change expression of UBC9 and Coro1A from RAW264.7 cells
1091 transfected with Scr siRNA and UBC9 siRNA. GAPDH was used for gene normalization. Each
1092 dot represents one independent experiment.

1093 E. Top: RAW 264.7 cell lysates immunoprecipitated with anti-Coro1A antibody and
1094 immunoblotted for Raftlin. Bottom:10% of input loaded from the same cell lysate and
1095 immunoblotted for Coro1A, Raftlin, and Actin. Isotype antibodies (IgG) were used as a negative
1096 control.

1097 F. Multiple sequence alignment of Raftlin protein sequences from eight mammalian species
1098 reveals a conserved SUMO-binding site (K31) (highlighted in a black rectangle).

1099 G. Representative immunoblot showing stable expression of Raftlin $^{K31R}$, similar to Raftlin $^{WT}$.

1100

1101 **Material Methods:**

1102 **Human patient samples:**

1103 Human patient samples for IBS (10), UC (19), SCRC (9), and CAC (15) were obtained from the
1104 Gastroenterology Department at All India Institute of Medical Sciences, New Delhi, India. Colonic
1105 biopsies of patients were obtained during routine colonoscopies, with exclusion and inclusion
1106 criteria as specified by Mustafa et al. (2017) and Suhail et al. (2019).Six biopsies were collected

1107 from each patient for use in qRT-PCR, immunoblotting, and histopathology. The study included
1108 patients with mild and moderate Ulcerative Colitis Endoscopic Index of Severity (UCEIS) scores.
1109 Informed consent forms were obtained from each patient during the biopsy procedure. The
1110 patient's sex was not considered in the current study. Ethical approval was obtained from the
1111 Regional Centre for Biotechnology (Approval No. RCB-IEC-H-11) and AIIMS (Approval No.
1112 IEC-217/05.04.2019, RP-19/2019) for using these patients' samples in the current study.

1113 **Mice:** All C57BL/6 mice were maintained in pathogen-free conditions by following all husbandry
1114 standards in the small animal facility of RCB. All mice were provided with sterilized food and
1115 water at 25 °C, under a 12-hour light/dark cycle. To induce CAC, Azoxymethane (AOM) was
1116 injected intraperitoneally into 6-8-week-old male/ female mice weighing 18-20 g at a dose of 10
1117 mg/kg. To induce chronic colonic inflammation, mice were fed 1% Dextran-sulfate-sodium (DSS)
1118 (w/v) (36–50 kDa molecular weight) through autoclaved drinking water for 7 days, followed by a
1119 recovery period of 1 week, during which mice were fed normal drinking water. The model lasts
1120 for 14 weeks. Mice in the control group were fed with normal drinking water. The same procedure
1121 was employed for developing CAC in IL10 $^{-/-}$ mice (C57BL/6 background, obtained from the
1122 National Institute of Immunology, India) and Coro1A$^{-/-}$ mice (C57BL/6 background, kindly
1123 provided by Prof. Jean Pieters, Biozentrum, Switzerland). An acute colitis model was performed
1124 in 6-8-week-old male/female mice weighing 18-20 g, as described by (Suhail et al., 2019).
1125 Symptoms of colitis, such as diarrhea, rectal bleeding, and body weight loss, were monitored
1126 routinely throughout the experiment. Sporadic colorectal cancer model performed in APC$^{+/-}$ mice.
1127 For 1 week, WT and APC$^{+/-}$ mice were fed 2% DSS, followed by 14 weeks of normal drinking
1128 water. Organs, such as the colon and spleen, were examined for gross morphological changes and
1129 used for further experimental analysis. For some crucial *in vitro* experiments, Bone marrow-
1130 derived macrophages (BMDMs) from WT and Coronin1a $^{-/-}$ mice were harvested. The RCB
1131 Institutional Animal Ethics Committee (IAEC) has approved the above-mentioned animal studies
1132 (RCB/IAEC/2024/199, RCB/IAEC/2023/177, RCB/IAEC/2023/156, RCB/IAEC/2021/101).

1133 **Cell culture and transfections**: Murine macrophage cell lines RAW 264.7 and J774 $^{WT}$ and J774
1134 $^{Coro1A\ KD}$ cell lines were grown in DMEM containing 10% fetal bovine serum, 3.7 g/litre Sodium
1135 bicarbonate, 1% sodium pyruvate, 1% penicillin and streptomycin solution, and 14 mM HEPES
1136 buffer (pH 7.4). BMDMs isolated and cultured from WT and Coronin1A $^{-/-}$ mice as described

1137 by(Toda et al., 2021). All cells were incubated at 37 °C with 5% $CO_2$. RAW264.7 cells were used
1138 for plasmid-based overexpression and siRNA-based knockdown studies. WT plasmids and
1139 mutants of Coro1A and Raftlin, and Scrambled and targeted UBC9 siRNA were transfected in
1140 RAW264.7 using Xtremegene (Merck) and DharmaFECT (Horizon Discovery) according to the
1141 manufacturer's instructions. RAW264.7, BMDMs, J774 $^{WT,}$ and J774 $^{Coro1A\ KD}$ cells were
1142 stimulated with IL-4 (20ng/ml) and TGF-β (10ng/ml) for a specified time period. The
1143 pharmacological drugs used in this study to treat RAW264.7, J774 $^{WT,}$ and J774 $^{Coro1A\ KD}$ cells are
1144 MG-132, Bafilomycin-A1, BAPTA-AM, FK-506, Cyclosporin-A, and Ionomycin. Unstimulated
1145 or untreated cells served as the control.

1146 **Immunoblot**: Human and murine tissues and cell lysates were prepared using RIPA lysis buffer
1147 containing 1X protease inhibitor and 20 mM NEM. The BCA assay was used to quantify proteins.
1148 Equal concentrations of proteins were separated on sodium-dodecyl sulphate polyacrylamide gel
1149 electrophoresis (SDS-PAGE) and transferred to a 0.2 µm or 0.4 µm nitrocellulose membrane. Blots
1150 were blocked with 5% skim milk for 1 hour at room temperature, then probed with antibodies
1151 against the desired proteins overnight at 4 °C. Protein blots were probed with the following set of
1152 antibodies: SENP5, SUMO2/3, SMAD3, Coronin1A, GFP, Actin, GAPDH, TGF-beta, TGF-βRI,
1153 pAKT, AKT, Raftlin, Ubiquitin, and P62. The next day, host-specific HRP-conjugated secondary
1154 antibodies, anti-Rabbit and anti-Mouse, were added and incubated for 1 hour at room temperature.
1155 Protein bands were then detected with Immobilon Forte Western HRP substrate and visualized
1156 with the ImageQuant LAS-4000 imaging system. Immunoblot densitometry analysis was
1157 performed using ImageJ software.

1158 **Quantitative real-time PCR:** RNA was extracted from human patient biopsies, mouse tissue, and
1159 different cell lines using the RNeasy RNA isolation kit. cDNA was synthesized using 1 µg of
1160 isolated RNA from each sample using the iScript cDNA Synthesis Kit. Real-time PCR was
1161 performed using SYBR Green Master Mix in a 20 µL reaction volume on 96-well plates with the
1162 CFX96 Real-Time System. The housekeeping genes GAPDH and HPRT were used for
1163 normalization based on each sample's origin. The list of primers used in this study is included in
1164 the supplementary material.

1165 **Immunohistochemistry**: Mice colon tissue sections were fixed in 4% paraformaldehyde solution
1166 overnight and transferred to cryomatrix, followed by snap-freezing in liquid nitrogen. 5 µm-thick

1167 sections were cut onto glass slides using a Cryotome. The patient's archived tissue biopsy slides
1168 were obtained from the Department of Pathology at AIIMS, New Delhi, India. Tissue sections
1169 were washed three times in 1x PBS (5 minutes each). Further, slides were treated with 3%
1170 Hydrogen peroxide for 10 minutes to quench endogenous peroxidase activity, followed by a
1171 second wash with PBS. Further slides were blocked with 5% Goat serum for 1 hour. Then, the
1172 sections were incubated overnight in a humid chamber with Coronin1A. The next day, sections
1173 were washed with PBS, then incubated with HRP-conjugated secondary antibodies for 2 hours.
1174 Further slides were washed in PBS, stained with DAB, and counterstained with Hematoxylin.
1175 Tissue sections were imaged using a Nikon Bright Field microscope.

1176 **Co-Immunoprecipitation**: Tissue lysate and cell lysate prepared using IP lysis buffer having 1X
1177 protease inhibitor. Samples were centrifuged at high speed at 4ºC for 10 minutes to remove debris.
1178 The supernatant was quantified to 1 mg protein, followed by the addition of the appropriate
1179 antibody at its concentration. Antibody-protein complexes were incubated overnight on an end-to-
1180 end rotor. The next day, activated Agarose-A-beads were used to pull down the antibody-protein
1181 complex. Beads were sedimented by centrifugation (0.5 rcf, 4ºC), washed with IP lysis buffer, and
1182 then denatured. An isotype control IgG was used as a negative control.

1183 **Nuclear fraction isolation:** Cells were washed with chilled PBS, scraped, and collected in pre-
1184 chilled tubes on ice. After centrifugation (10,000 rpm, 5 minutes, and 4 °C), the pellet was
1185 resuspended in a lysis buffer containing chilled PBS, protease inhibitors (PI), and NP-40, and
1186 incubated on ice for 10 minutes. To separate the cytoplasmic fraction, the cell lysate was
1187 centrifuged (10 minutes, 10,000 rpm, 4 °C). The supernatant is the cytoplasmic fraction, and the
1188 pellet is the nuclear fraction. The obtained nuclear pellet was washed 3 times with lysis buffer and
1189 subsequently denatured.

1190 **Hematoxylin and Eosin (H&E) and Sirius red staining:** 5-µm-thick paraffin-embedded tissue
1191 sections were deparaffinized in Xylene and rehydrated through a graded ethanol to distilled water.
1192 For H & E staining, tissue sections were stained with Hematoxylin, followed by eosin
1193 counterstaining. For Sirius red staining, tissue sections were stained with Weigert's iron
1194 hematoxylin, followed by Sirius red stain, and subsequently washed with acidified water to

1195 visualize collagen. Sliders were dehydrated in graded alcohol, cleared in Xylene, and mounted
1196 using DPX mountant. Tissue sections were visualized under a bright-field microscope.

1197 **Immunocytochemistry and structured illumination microscopy:** Cells seeded on a glass
1198 coverslip, fixed with 4% methanol-free paraformaldehyde, washed with PBS, and blocked in 0.1
1199 % BSA containing 0.01% Triton X-100 for 1 hour. Further cells were incubated overnight at 4ºC
1200 with primary antibodies against Coro1A, TGF-βRI, GFP, pSMAD3, Lysotracker, and Phalloidin-
1201 594, followed by a fluorochrome-conjugated secondary antibody the next day for 2 hours at room
1202 temperature. DAPI was used to counterstain nuclei. Coverslips were mounted using Prolong Gold
1203 antifade reagent and imaged by confocal microscopy (Leica SP8) or structured illumination
1204 microscopy (Elyra PS1, Carl Zeiss).

1205 **Lamina propria isolation:** The Lamina propria of the colon was isolated using the method
1206 described by Weigmann et al. (2007). Briefly, the harvested mouse colon was washed with ice-
1207 cold PBS, then longitudinally cut open and again washed with PBS to remove mucus. The open
1208 intestine is cut into small pieces and subjected to predigestion in a buffer containing 5 mM EDTA
1209 and 1 mM DTT for 15-20 minutes in a shaking incubator. With vigorous vortexing, the predigested
1210 tissue was filtered through a 100 µm filter. The remaining tissue was finely chopped and incubated
1211 in a buffer containing collagen and DNase I (50mg per 100 ml PBS) for one hour at 37ºC on slow
1212 shaking. After incubation, the tubes were vortexed, and the cell suspension was passed through a
1213 40 µm strainer. The collected single-cell suspension was vortexed and centrifuged at 500 g for 10
1214 minutes at room temperature. The pellet obtained was resuspended in PBS, and proceeded to flow
1215 cytometric immune phenotyping.

1216 **Flow Cytometry:** Flow cytometric analysis was carried out for immune cells retrieved from the
1217 lamina propria region of the colon (*in vivo*) and cultured J774 $^{WT}$ and J774 $^{Coro1A\ KD}$ cells (*in vitro*).
1218 *In vivo*-derived immune cells were stained with fixable live-dead stain (Aqua Zombie) for 15
1219 minutes at room temperature in the dark, followed by surface marker staining with fluorophore-
1220 conjugated antibodies against CD-45, CD11b, F4/80, and Ly6G for 1 hour at 4ºC. Further, cells
1221 were fixed with 4% paraformaldehyde at room temperature, followed by permeabilization with
1222 chilled methanol for 20 minutes on ice. Intracellular staining was performed using anti-iNOS and
1223 anti-Arginase-1 fluorophore-conjugated antibodies, along with a primary antibody against
1224 Coronin1A for 1 hour of incubation, followed by secondary antibody staining for 1 hour. The same

1225 fixation, permeabilization, and intracellular staining procedure was employed for *in vitro*-cultured
1226 J774 $^{WT}$ and J774 $^{Coro1A\ KD}$ cells to stain Arginase-1. Stained cells were resuspended in FACS
1227 buffer, acquired on a BD FACSymphony, and analyzed using FlowJo software.

1228 **Enzyme-linked immunosorbent assay**: Cell supernatant collected from the cell culture system
1229 and colonic tissue lysates were centrifuged to remove debris. The samples were quantified using
1230 the BCA assay, and equal concentrations of samples were subjected to a kit-based enzyme-linked
1231 immunosorbent assay (ELISA) (R&D Systems) to measure TGF-β & IL-10.

1232 **Protein Digestion and LC-MS/MS**: Murine tissue lysates were immunoprecipitated using an
1233 anti-SENP5 antibody, and J774 cell lysates were immunoprecipitated with an anti-Coronin1A
1234 antibody. An isotype-matched IgG antibody was used as a negative control. The co-
1235 immunoprecipitated samples were resolved on 10% SDS–PAGE, followed by in-gel digestion
1236 with Trypsin Gold at a 1:50 enzyme-to-substrate ratio. The resulting peptides were extracted and
1237 purified using C18 StepPak columns, desalted, and reconstituted in a solution of 98% water, 1%
1238 acetonitrile, and 0.1% formic acid.

1239 Tandem MS/MS analysis was performed on a TripleTOF 5600 mass spectrometer (AB Sciex)
1240 operated in information-dependent acquisition (IDA) mode. The instrument was coupled to a trap
1241 column (Magic C18 AQ, 0.1 × 20 mm, 3 µm, 200 Å) and an analytical column (Magic C18 AQ,
1242 0.1 × 150 mm, 3 µm, 200 Å) via a nano-electrospray ionization source. Peptide separation was
1243 achieved using a linear gradient of 5–75% solvent B (100% acetonitrile with 0.1% formic acid)
1244 over 135 minutes at a flow rate of 300 nL/min; solvent A was 100% water with 0.1% formic acid.

1245 The mass spectrometer was operated in data-dependent acquisition mode, automatically switching
1246 between MS and MS/MS scans. Survey MS spectra were acquired over an m/z range of 300–2000
1247 at a resolution of 75,000. The six most abundant precursor ions per cycle were selected for
1248 fragmentation by collision-induced dissociation (CID), with a fixed cycle time of 3 s and a dynamic
1249 exclusion period of 2 min. The obtained raw files from the MS system (.wiff) were processed for
1250 peptide/protein identification using MaxQuant software (v1.6.0.16) under default settings. An in-
1251 house combined UniProt (*Mus musculus*) database, together with common contaminants
1252 sequences, was provided for MS/MS spectra search. The detailed workflow of peptide/protein

identification, including other search parameters and filtering criteria, was followed as mentioned in (Suhail et al., 2019)

**Structural modeling and docking**: The crystal structure of Coro1A (PDB ID: 2AQ5) and the AlphaFold-predicted structures of Raftlin1 and SUMO2 were used for protein–protein docking. Blind docking was performed using the HADDOCK 2.4 web server (https://rascar.science.uu.nl/haddock2.4/) in standard-precision mode, generating multiple poses without predefined binding sites. The docked models were clustered and ranked using the default HADDOCK scoring function, and the top three complexes were selected for refinement. Further, using the Schrödinger software suite (https://www.schrodinger.com/), the energies of poses were minimized, and binding energies were calculated. The final model was selected based on the high docking score and favorable minimized binding energies.

**Multiple sequence alignment (MSA):** FASTA sequences of Coro1A and Raftlin from 8 organisms were retrieved from the Uniprot database and aligned using Clustal Omega with default parameters. Multiple sequence alignments were visualized and analyzed using Jalview (v2.11.5.0) with the ClustalX coloring scheme. Alignment annotations, including consensus, conservation, quality scores, and occupancy, were displayed below the alignment.

**Molecular Dynamics Simulation**: The wild-type Coro1A structure (PDB ID: 2AQ5) and the PyMOL-generated Coro1A V155K mutant were subjected to molecular dynamics simulations using the CABS flex server with default parameters for 10 seconds, an equivalent simulation time. The server uses coarse-grained Monte Carlo simulations to efficiently sample near-native protein conformational dynamics. Default parameters were used, including structural clustering and all-atom reconstruction. The resulting ensembles were analyzed for conformational flexibility and residue fluctuations, with residue-wise mobility quantified using root-mean-square fluctuation (RMSF) plots generated with the server's analysis tools.

**Quantification and statistical analysis:** Data were analyzed and visualized using GraphPad Prism version 8.0.1. Results are presented as the mean ± standard error from independent experiments performed in triplicate. As appropriate, statistical analysis was carried out using the

unpaired two-tailed Student's t-test or Welch's t-test. A *p*-value less than 0.05 was considered statistically significant.

**Acknowledgment:**

We thank the sophisticated instrumentation facility at the Central Instrumentation Facility (CIF) of the Regional Centre for Biotechnology (RCB), the Flow Cytometry, Confocal Microscopy, Genomics, and Mass Spectrometry facility of the Advanced Technology Platform Centre (ATPC) in the RCB campus, and the Experimental Animal Facility (EAF) at NCR-Biotech Science Cluster for animal experiments. We acknowledge Addgene for the Coro1A plasmid (102815). We are grateful to Prof. Josef M. Penninger and Prof. Jean Pieters for sharing Coro1A knockout mice and J774 $^{WT}$ and J774 $^{Coro1A\ KD}$ cells. We are thankful to Prof. Venuprasad Poojary for the Raftlin Plasmid. We thank Prof. Tushar K. Maiti for his extended help with mass spectrometry-based experiments. We are grateful to Dr. Rajender Motiani and Dr. Pallavi Keshtrapal for sharing the crucial reagents used in the experiments.

**Funding:** This work was supported by an RCB Core Grant, an ICMR(IIRP/SG-2024-01-00385) and DBT (BT/PR45284/CMD/150/9/2022) grant, and a CSIR-JRF fellowship (Council of Scientific and Industrial Research, Govt. of India) of Rohan Babar.

**Competing Interest:**
The authors declare that they have no competing interests**.**

**Author Contributions:**

**Conceptualization**: Chittur V. Srikanth.

**Methodology**: Rohan Babar, Chittur V. Srikanth.

**Investigation**: Rohan Babar, Poorvi Saini, Neha Guliya, Prakhar Varshney, Vishnu Ashok Kumar, Prabhakar Mujagond.

**Resource**: Rohan Babar, Aamir Suhail, Mukesh Singh, Dolly Jain, Lalita Mehra, Shivangi Tyagi.

**Supervision**: Avinash Bajaj, Krishnan Vengadesan, Prasenjit Das, Vineet Ahuja, and Chittur V. Srikanth.

**Project Administration**: Chittur V. Srikanth.
**Writing-original draft**: Rohan Babar, Poorvi Saini, Neha Guliya, and Prakhar Varshney.

**Writing -review and editing**- Rohan Babar and Chittur V. Srikanth.

References:


1. Foersch S, Neurath MF. Colitis-associated neoplasia: Molecular basis and clinical translation. Vol. 71, Cellular and Molecular Life Sciences Birkhauser Verlag AG; 2014. p. 3523–35.
2. Zhou RW, Harpaz N, Itzkowitz SH, Parsons RE. Molecular mechanisms in colitis-associated colorectal cancer. Vol. 12, Oncogenesis Springer Nature; 2023.
3. Díaz-Gay M, dos Santos W, Moody S, Kazachkova M, Abbasi A, Steele CD, et al. Geographic and age variations in mutational processes in colorectal cancer. Nature. Nature Research; 2025;643(8070):230–40. DOI: 10.1038/s41586-025-09025-8
4. Bogaert J, Prenen H. Molecular genetics of colorectal cancer. Vol. 27, Annals of Gastroenterology 2014. p. 9–14.
5. Su Z, El Hage M, Linnebacher M. Mutation patterns in colorectal cancer and their relationship with prognosis. Heliyon. Elsevier Ltd; 2024;10(17). DOI: 10.1016/j.heliyon.2024.e36550
6. Yin Y, Wan J, Yu J, Wu K. Molecular Pathogenesis of Colitis-associated Colorectal Cancer: Immunity, Genetics, and Intestinal Microecology. Vol. 29, Inflammatory Bowel Diseases Oxford University Press; 2023. p. 1648–57.
7. Yamagishi H, Kuroda H, Imai Y, Hiraishi H. Molecular pathogenesis of sporadic colorectal cancers. Vol. 35, Chinese Journal of Cancer Landes Bioscience; 2016.
8. Yashiro M. Ulcerative colitis-associated colorectal cancer. World J Gastroenterol. WJG Press; 2014;20(44):16389–97. DOI: 10.3748/wjg.v20.i44.16389

1342 9. Shawki S, Ashburn J, Signs SA, Huang E. Colon Cancer: Inflammation-Associated
1343 Cancer. Vol. 27, Surgical Oncology Clinics of North America W.B. Saunders; 2018. p.
1344 269–87.

1345 10. Kakiuchi N, Yoshida K, Uchino M, Kihara T, Akaki K, Inoue Y, et al. Frequent mutations
1346 that converge on the NFKBIZ pathway in ulcerative colitis. Nature. Nature Research;
1347 2020;577(7789):260–5. DOI: 10.1038/s41586-019-1856-1

1348 11. Dan WY, Zhou GZ, Peng LH, Pan F. Update and latest advances in mechanisms and
1349 management of colitis-associated colorectal cancer. Vol. 15, World Journal of
1350 Gastrointestinal Oncology Baishideng Publishing Group Inc; 2023. p. 1317–31.

1351 12. Deng Y, Jia X, Liu L, He Q, Liu L. The role of intestinal macrophage polarization in
1352 colitis-associated colon cancer. Vol. 16, Frontiers in Immunology Frontiers Media SA;
1353 2025.

1354 13. Zhang M, Li X, Zhang Q, Yang J, Liu G. Roles of macrophages on ulcerative colitis and
1355 colitis-associated colorectal cancer. Vol. 14, Frontiers in Immunology Frontiers Media
1356 S.A.; 2023.

1357 14. Shin AE, Tesfagiorgis Y, Larsen F, Derouet M, Zeng PYF, Good HJ, et al.
1358 F4/80+Ly6Chigh Macrophages Lead to Cell Plasticity and Cancer Initiation in Colitis.
1359 Gastroenterology. W.B. Saunders; 2023;164(4):593-609.e13. DOI:
1360 10.1053/j.gastro.2023.01.002

1361 15. Hardbower DM, Coburn LA, Asim M, Singh K, Sierra JC, Barry DP, et al. EGFR-
1362 mediated macrophage activation promotes colitis-associated tumorigenesis. Oncogene.
1363 Nature Publishing Group; 2017;36(27):3807–19. DOI: 10.1038/onc.2017.23

1364 16. Wang Y, Liu H, Zhang Z, Bian D, Shao K, Wang S, et al. G-MDSC-derived exosomes
1365 mediate the differentiation of M-MDSC into M2 macrophages promoting colitis-to-cancer
1366 transition. J Immunother Cancer. BMJ Publishing Group; 2023;11(6). DOI: 10.1136/jitc-
1367 2022-006166

1368 17. Yuan Q, Gu J, Zhang J, Liu S, Wang Q, Tian T, et al. MyD88 in myofibroblasts enhances
1369 colitis-associated tumorigenesis via promoting macrophage M2 polarization. Cell Rep.
1370 Elsevier B.V.; 2021;34(5). DOI: 10.1016/j.celrep.2021.108724

1371 18. Sheng YH, Davies JM, Wang R, Wong KY, Giri R, Yang Y, et al. MUC1-mediated
1372 Macrophage Activation Promotes Colitis-associated Colorectal Cancer via Activating the
1373 Interleukin-6/ Signal Transducer and Activator of Transcription 3 Axis. CMGH. Elsevier
1374 Inc.; 2022;14(4):789–811. DOI: 10.1016/j.jcmgh.2022.06.010

1375 19. Long Y, Huang F, Zhang J, Zhang J, Cheng R, Zhu L, et al. Identification of
1376 SUMOylation-related signature genes associated with immune infiltration in ulcerative

1377 colitis through bioinformatics analysis and experimental validation. Gene. Elsevier B.V.;
1378 2025;935. DOI: 10.1016/j.gene.2024.148996

1379 20. Ma XN, Li MY, Qi GQ, Wei LN, Zhang DK. SUMOylation at the crossroads of gut
1380 health: insights into physiology and pathology. Vol. 22, Cell Communication and
1381 Signaling BioMed Central Ltd; 2024.

1382 21. Gostissa M, Hengstermann A, Fogal V, Sandy P, Schwarz SE, Scheffner M, et al.
1383 Activation of p53 by conjugation to the ubiquitin-like protein SUMO-1. Vol. 18, The
1384 EMBO Journal 1999.

1385 22. Zhou Z, Wang M, Li J, Xiao M, Chin YE, Cheng J, et al. SUMOylation and SENP3
1386 regulate STAT3 activation in head and neck cancer. Oncogene. Nature Publishing Group;
1387 2016;35(45):5826–38. DOI: 10.1038/onc.2016.124

1388 23. Yang Q, Tang J, Xu C, Zhao H, Zhou Y, Wang Y, et al. Histone deacetylase 4 inhibits
1389 NF-κB activation by facilitating IκBα sumoylation. J Mol Cell Biol. Oxford University
1390 Press; 2020;12(12):933–45. DOI: 10.1093/jmcb/mjaa043

1391 24. Lin CH, Liu SY, Lee EHY. SUMO modification of Akt regulates global SUMOylation
1392 and substrate SUMOylation specificity through Akt phosphorylation of Ubc9 and
1393 SUMO1. Oncogene. Nature Publishing Group; 2016;35(5):595–607. DOI:
1394 10.1038/onc.2015.115

1395 25. Liu T, Wang H, Chen Y, Wan Z, Du Z, Shen H, et al. SENP5 promotes homologous
1396 recombination-mediated DNA damage repair in colorectal cancer cells through H2AZ
1397 deSUMOylation. Journal of Experimental and Clinical Cancer Research. BioMed Central
1398 Ltd; 2023;42(1). DOI: 10.1186/s13046-023-02789-9

1399 26. Sheng Z, Luo S, Huang L, Deng YN, Zhang N, Luo Y, et al. SENP1-mediated
1400 deSUMOylation of YBX1 promotes colorectal cancer development through the SENP1-
1401 YBX1-AKT signaling axis. Oncogene. Springer Nature; 2025;44(19):1361–74. DOI:
1402 10.1038/s41388-025-03302-6

1403 27. Du L, Li YJ, Fakih M, Wiatrek RL, Duldulao M, Chen Z, et al. Role of SUMO activating
1404 enzyme in cancer stem cell maintenance and self-renewal. Nat Commun. Nature
1405 Publishing Group; 2016;7. DOI: 10.1038/ncomms12326

1406 28. Arnesen H, Müller MHB, Aleksandersen M, Østby GC, Carlsen H, Paulsen JE, et al.
1407 Induction of colorectal carcinogenesis in the C57BL/6J and A/J mouse strains with a
1408 reduced DSS dose in the AOM/DSS model. Lab Anim Res. BioMed Central Ltd;
1409 2021;37(1). DOI: 10.1186/s42826-021-00096-y

1410 29. Ren J, Sui H, Fang F, Li Q, Li B. The application of ApcMin/+ mouse model in colorectal
1411 tumor researches. Vol. 145, Journal of Cancer Research and Clinical Oncology Springer
1412 Science and Business Media Deutschland GmbH; 2019. p. 1111–22.

1413 30. Sánchez-Alba L, Ying L, Maletic MD, De Bolòs A, Borràs-Gas H, Liu B, et al. Structural
1414 basis for the human SENP5's SUMO isoform discrimination. Nature Communications .
1415 Nature Research; 2025;16(1). DOI: 10.1038/s41467-025-60029-4

1416 31. Galkin VE, Orlova A, Brieher W, Yuan Kueh H, Mitchison TJ, Egelman EH. Author
1417 manuscript. Vol. 376, J Mol Biol 2008.

1418 32. Humphries CL, Balcer HI, D'Agostino JL, Winsor B, Drubin DG, Barnes G, et al. Direct
1419 regulation of Arp2/3 complex activity and function by the actin binding protein coronin.
1420 Journal of Cell Biology. 2002;159(6):993–1004. DOI: 10.1083/jcb.200206113

1421 33. Mueller P, Massner J, Jayachandran R, Combaluzier B, Albrecht I, Gatfield J, et al.
1422 Regulation of T cell survival through coronin-1-mediated generation of inositol-1,4,5-
1423 trisphosphate and calcium mobilization after T cell receptor triggering. Nat Immunol.
1424 2008;9(4):424–31. DOI: 10.1038/ni1570

1425 34. Stocker TJ, Pircher J, Skenderi A, Ehrlich A, Eberle C, Megens RTA, et al. The Actin
1426 Regulator Coronin-1A Modulates Platelet Shape Change and Consolidates Arterial
1427 Thrombosis. Thromb Haemost. Georg Thieme Verlag; 2018;118(12):2098–111. DOI:
1428 10.1055/s-0038-1675604

1429 35. Castro-Castro A, Ojeda V, Barreira M, Sauzeau V, Navarro-Lérida I, Muriel O, et al.
1430 Coronin 1A promotes a cytoskeletal-based feedback loop that facilitates Rac1
1431 translocation and activation. EMBO Journal. 2011;30(19):3913–27. DOI:
1432 10.1038/emboj.2011.310

1433 36. Pick R, Begandt D, Stocker TJ, Salvermoser M, Thome S, Böttcher RT, et al. Coronin 1A,
1434 a novel player in integrin biology, controls neutrophil trafficking in innate immunity.
1435 Blood. American Society of Hematology; 2017;130(7):847–58. DOI: 10.1182/blood-
1436 2016-11-749622

1437 37. Nicolaou O, Sokratous K, Makowska Z, Morell M, De Groof A, Montigny P, et al.
1438 Proteomic analysis in lupus mice identifies Coronin-1A as a potential biomarker for lupus
1439 nephritis. Arthritis Res Ther. BioMed Central; 2020;22(1). DOI: 10.1186/s13075-020-
1440 02236-6

1441 38. Siegmund K, Klepsch V, Hermann-Kleiter N, Baier G. Proof of principle for a T
1442 lymphocyte intrinsic function of Coronin 1A. Journal of Biological Chemistry. American
1443 Society for Biochemistry and Molecular Biology Inc.; 2016;291(42):22086–92. DOI:
1444 10.1074/jbc.M116.748012

1445 40. Deng X, Liu B, Jiang Q, Li G, Li J, Xu K. CREBH promotes autophagy to ameliorate
1446 NASH by regulating Coro1a. Biochim Biophys Acta Mol Basis Dis. Elsevier B.V.;
1447 2024;1870(1). DOI: 10.1016/j.bbadis.2023.166914

1448 41. Gunasekera DC, Ma J, Vacharathit V, Shah P, Ramakrishnan A, Uprety P, et al. The
1449 development of colitis in Il10 −/− mice is dependent on IL-22. Mucosal Immunol.
1450 Springer Nature; 2020;13(3):493–506. DOI: 10.1038/s41385-019-0252-3

1451 42. Suhail A, Rizvi ZA, Mujagond P, Ali SA, Gaur P, Singh M, et al. DeSUMOylase SENP7-
1452 Mediated Epithelial Signaling Triggers Intestinal Inflammation via Expansion of Gamma-
1453 Delta T Cells. Cell Rep. Elsevier B.V.; 2019;29(11):3522-3538.e7. DOI:
1454 10.1016/j.celrep.2019.11.028

1455 43. Kaminski S, Hermann-Kleiter N, Meisel M, Thuille N, Cronin S, Hara H, et al. Coronin
1456 1A is an essential regulator of the TGFβ receptor/SMAD3 signaling pathway in Th17
1457 CD4 + T cells. J Autoimmun. 2011;37(3):198–208. DOI: 10.1016/j.jaut.2011.05.018

1458 44. Burandt E, Lübbersmeyer F, Gorbokon N, Büscheck F, Luebke AM, Menz A, et al. E-
1459 Cadherin expression in human tumors: a tissue microarray study on 10,851 tumors.
1460 Biomark Res. BioMed Central Ltd; 2021;9(1). DOI: 10.1186/s40364-021-00299-4

1461 45. Rodriguez FJ, Lewis-Tuffin LJ, Anastasiadis PZ. E-cadherin's dark side: Possible role in
1462 tumor progression. Vol. 1826, Biochimica et Biophysica Acta - Reviews on Cancer 2012.
1463 p. 23–31.

1464 46. Popp C, Nichita L, Voiosu T, Bastian A, Cioplea M, Micu G, et al. Expression Profile of
1465 p53 and p21 in Large Bowel Mucosa as Biomarkers of Inflammatory-Related
1466 Carcinogenesis in Ulcerative Colitis. Dis Markers. Hindawi Limited; 2016;2016. DOI:
1467 10.1155/2016/3625279

1468 47. Lu X, Yu Y, Tan S. p53 expression in patients with ulcerative colitis - associated with
1469 dysplasia and carcinoma: A systematic meta-analysis. BMC Gastroenterol. BioMed
1470 Central Ltd.; 2017;17(1). DOI: 10.1186/s12876-017-0665-y

1471 48. Khursheed S, Ali T, Mushtaq M, Humayun S, Khan A, Akbar A, et al.
1472 Immunohistochemical Analysis of the p53 Protein in Colorectal Cancer: A
1473 Clinicopathological Study. Cureus. Springer Science and Business Media LLC; 2024;
1474 DOI: 10.7759/cureus.76172

1475 49. Suarez-Lopez L, Sriram G, Kong YW, Morandell S, Merrick KA, Hernandez Y, et al.
1476 MK2 contributes to tumor progression by promoting M2 macrophage polarization and
1477 tumor angiogenesis. Proc Natl Acad Sci U S A. National Academy of Sciences;
1478 2018;115(18):E4236–44. DOI: 10.1073/pnas.1722020115

1479 50. Zhang F, Wang H, Wang X, Jiang G, Liu H, Zhang G, et al. TGF-β induces M2-like
1480 macrophage polarization via SNAIL-mediated suppression of a pro-inflammatory
1481 phenotype [Internet]. Vol. 7 2016 [cited. Available from:
1482 www.impactjournals.com/oncotarget

1483 51. Deng Z, Fan T, Xiao C, Tian H, Zheng Y, Li C, et al. TGF-β signaling in health, disease,
1484 and therapeutics. Vol. 9, Signal Transduction and Targeted Therapy Springer Nature;
1485 2024.

1486 52. Massagué J. TGFβ signalling in context. Vol. 13, Nature Reviews Molecular Cell Biology
1487 2012. p. 616–30.

1488 53. Jayachandran R, Sundaramurthy V, Combaluzier B, Mueller P, Korf H, Huygen K, et al.
1489 Survival of Mycobacteria in Macrophages Is Mediated by Coronin 1-Dependent
1490 Activation of Calcineurin. Cell. Elsevier B.V.; 2007;130(1):37–50. DOI:
1491 10.1016/j.cell.2007.04.043

1492 54. Suo D, Park J, Harrington AW, Zweifel LS, Mihalas S, Deppmann CD. Coronin-1 is a
1493 neurotrophin endosomal effector that is required for developmental competition for
1494 survival. Nat Neurosci. 2014;17(1):36–45. DOI: 10.1038/nn.3593

1495 55. Huang W, Ghisletti S, Saijo K, Gandhi M, Aouadi M, Tesz GJ, et al. Coronin 2A mediates
1496 actin-dependent de-repression of inflammatory response genes. Nature.
1497 2011;470(7334):414–8. DOI: 10.1038/nature09703

1498 56. Kerscher O. SUMO junction - What's your function? New insights through SUMO-
1499 interacting motifs. Vol. 8, EMBO Reports 2007. p. 550–5.

1500 57. Song J, Durrin LK, Wilkinson TA, Krontiris TG, Chen Y. Identification of a SUMO-
1501 binding motif that recognizes SUMO-modified proteins [Internet]. Vol. 101 2004 [cited.
1502 Available from: www.pnas.orgcgidoi10.1073pnas.0403498101

1503 58. Gou Y, Liu D, Chen M, Wei Y, Huang X, Han C, et al. GPS-SUMO 2.0: an updated
1504 online service for the prediction of SUMOylation sites and SUMO-interacting motifs.
1505 Nucleic Acids Res. Oxford University Press; 2024;52(W1):W238–47. DOI:
1506 10.1093/nar/gkae346

1507 59. Beauclair G, Bridier-Nahmias A, Zagury JF, Säb A, Zamborlini A. JASSA: A
1508 comprehensive tool for prediction of SUMOylation sites and SIMs. Bioinformatics.
1509 Oxford University Press; 2015;31(21):3483–91. DOI: 10.1093/bioinformatics/btv403

1510 60. Rytinki MM, Palvimo JJ. SUMOylation attenuates the function of PGC-1α. Journal of
1511 Biological Chemistry. 2009;284(38):26184–93. DOI: 10.1074/jbc.M109.038943

1512 61. Niu X, Xu C, Cheuk YC, Xu X, Liang L, Zhang P, et al. Characterizing hub biomarkers
1513 for post-transplant renal fibrosis and unveiling their immunological functions through

1514 RNA sequencing and advanced machine learning techniques. J Transl Med. BioMed
1515 Central Ltd; 2024;22(1). DOI: 10.1186/s12967-024-04971-9

1516 62. Elihamu D, Li Y, Wang Y, Cui H, Xing Y, Peng H, et al. CORO1A: a pan-cancer
1517 prognosis, diagnostic and immune biomarker based on breast cancer validation. Front
1518 Oncol. Frontiers Media SA; 2025;15. DOI: 10.3389/fonc.2025.1670526

1519 63. Kros JM, Zeneyedpour L, Pedrosa RMSM, Belcaid Z, Dik WA, Luider TM, et al. T cell
1520 induced expression of Coronin-1A facilitates blood-brain barrier transmigration of breast
1521 cancer cells. Sci Rep. Nature Research; 2024;14(1). DOI: 10.1038/s41598-024-83301-x

1522 64. Li Z, Chen L, Wei Z, Liu H, Zhang L, Huang F, et al. A novel classification method for
1523 LUAD that guides personalized immunotherapy on the basis of the cross-talk of
1524 coagulation- and macrophage-related genes. Front Immunol. Frontiers Media SA;
1525 2025;16. DOI: 10.3389/fimmu.2025.1518102

1526 65. Sun Y, Ma Q, Chen Y, Liao D, Kong F. Identification and analysis of prognostic immune
1527 cell homeostasis characteristics in lung adenocarcinoma. Clinical Respiratory Journal.
1528 John Wiley and Sons Inc; 2024;18(5). DOI: 10.1111/crj.13755

1529 66. Zhou Y, Shi X, Chen H, Mao B, Song X, Gao L, et al. Tumor Immune Microenvironment
1530 Characterization of Primary Lung Adenocarcinoma and Lymph Node Metastases. Biomed
1531 Res Int. Hindawi Limited; 2021;2021. DOI: 10.1155/2021/5557649

1532 67. Bao M, Huang Y, Lang Z, Zhao H, Saito Y, Nagano T, et al. Proteomic analysis of plasma
1533 exosomes in patients with non-small cell lung cancer. Transl Lung Cancer Res. AME
1534 Publishing Company; 2022;11(7):1434–52. DOI: 10.21037/tlcr-22-467

1535 68. Kumar P, Nandi S, Tan TZ, Ghee Ler S, Chia KS, Lim W-Y, et al. Highly sensitive and
1536 specific novel biomarkers for the diagnosis of transitional bladder carcinoma [Internet].
1537 Available from: www.impactjournals.com/oncotarget/

1538 69. Jayachandran R, Gumienny A, Bolinger B, Ruehl S, Lang MJ, Fucile G, et al. Disruption
1539 of Coronin 1 Signaling in T Cells Promotes Allograft Tolerance while Maintaining Anti-
1540 Pathogen Immunity. Immunity. Cell Press; 2019;50(1):152-165.e8. DOI:
1541 10.1016/j.immuni.2018.12.011

1542 70. Ndinyanka Fabrice T, Buczak K, Schmidt A, Pieters J. T cell population size control by
1543 coronin 1 uncovered: from a spot identified by two-dimensional gel electrophoresis to
1544 quantitative proteomics. Vol. 22, Expert Review of Proteomics Taylor and Francis Ltd.;
1545 2025. p. 35–44.

1546 71. Jayachandran R, Pieters J. Regulation of immune cell homeostasis and function by
1547 coronin 1. Vol. 28, International Immunopharmacology Elsevier B.V.; 2015. p. 825–8.

1548 72. Shiow LR, Paris K, Akana MC, Cyster JG, Sorensen RU, Puck JM. Severe combined
1549 immunodeficiency (SCID) and attention deficit hyperactivity disorder (ADHD) associated
1550 with a coronin-1A mutation and a chromosome 16p11.2 deletion. Clinical Immunology.
1551 2009;131(1):24–30. DOI: 10.1016/j.clim.2008.11.002

1552 73. Younis DA, Marosvari M, Liu W, Pulikkot S, Cao Z, Zhou B, et al. CFTR dictates
1553 monocyte adhesion by facilitating integrin clustering but not activation. Proc Natl Acad
1554 Sci U S A. National Academy of Sciences; 2025;122(3). DOI: 10.1073/pnas.2412717122

1555 74. Deng Z, Fan T, Xiao C, Tian H, Zheng Y, Li C, et al. TGF-β signaling in health, disease,
1556 and therapeutics. Vol. 9, Signal Transduction and Targeted Therapy Springer Nature;
1557 2024.

1558 75. Fridlender ZG, Sun J, Kim S, Kapoor V, Cheng G, Ling L, et al. Polarization of Tumor-
1559 Associated Neutrophil Phenotype by TGF-β: "N1" versus "N2" TAN. Cancer Cell. Cell
1560 Press; 2009;16(3):183–94. DOI: 10.1016/j.ccr.2009.06.017

1561 76. Gong D, Shi W, Yi S ju, Chen H, Groffen J, Heisterkamp N. TGFβ signaling plays a
1562 critical role in promoting alternative macrophage activation. BMC Immunol. 2012;13.
1563 DOI: 10.1186/1471-2172-13-31

1564 77. Lin CS, Chen MF, Wang YS, Chuang TF, Chiang YL, Chu RM. IL-6 restores dendritic
1565 cell maturation inhibited by tumor-derived TGF-β through interfering Smad 2/3 nuclear
1566 translocation. Cytokine. 2013;62(3):352–9. DOI: 10.1016/j.cyto.2013.03.005

1567 78. Mckarns SC, Schwartz RH, Kaminski NE. Smad3 Is Essential for TGF-1 to Suppress IL-2
1568 Production and TCR-Induced Proliferation, but Not IL-2-Induced Proliferation1 [Internet].
1569 2004 [cited. Available from:
1570 https://academic.oup.com/jimmunol/article/172/7/4275/8060313

1571 79. Strobl H, Knapp W. TGF-1 regulation of dendritic cells TGF-/ dendritic cell / Langerhans
1572 cell / differentiation / antigen presentation. 1999.

1573 80. Calon A, Espinet E, Palomo-Ponce S, Tauriello DVF, Iglesias M, Céspedes MV, et al.
1574 Dependency of Colorectal Cancer on a TGF-β-Driven Program in Stromal Cells for
1575 Metastasis Initiation. Cancer Cell. Cell Press; 2012;22(5):571–84. DOI:
1576 10.1016/j.ccr.2012.08.013

1577 81. Means AL, Freeman TJ, Zhu J, Woodbury LG, Marincola-Smith P, Wu C, et al. Epithelial
1578 Smad4 Deletion Up-Regulates Inflammation and Promotes Inflammation-Associated
1579 Cancer. CMGH. Elsevier Inc; 2018;6(3):257–76. DOI: 10.1016/j.jcmgh.2018.05.006

1580 82. Gong D, Shi W, Yi S ju, Chen H, Groffen J, Heisterkamp N. TGFβ signaling plays a
1581 critical role in promoting alternative macrophage activation. BMC Immunol. 2012;13.
1582 DOI: 10.1186/1471-2172-13-31

1583 83. Chan MKK, Chung JYF, Tang PCT, Chan ASW, Ho JYY, Lin TPT, et al. TGF-β
1584 signaling networks in the tumor microenvironment. Vol. 550, Cancer Letters Elsevier
1585 Ireland Ltd; 2022.

1586 84. Li J, Liu Y, Wang B, Xu Y, Ma A, Zhang F, et al. Myeloid TGF-β signaling contributes to
1587 colitis-associated tumorigenesis in mice. Carcinogenesis. 2013;34(9):2099–108. DOI:
1588 10.1093/carcin/bgt172

1589 85. Wang W, Li X, Zheng D, Zhang D, Peng X, Zhang X, et al. Dynamic changes and
1590 functions of macrophages and M1/M2 subpopulations during ulcerative colitis-associated
1591 carcinogenesis in an AOM/DSS mouse model. Mol Med Rep. Spandidos Publications;
1592 2015;11(4):2397–406. DOI: 10.3892/mmr.2014.3018

1593 86. Zadka Ł, Chabowski M, Grybowski D, Piotrowska A, Dzięgiel P. Interplay of stromal
1594 tumor-infiltrating lymphocytes, normal colonic mucosa, cancer-associated fibroblasts,
1595 clinicopathological data and the immunoregulatory molecules of patients diagnosed with
1596 colorectal cancer. Cancer Immunology, Immunotherapy. Springer Science and Business
1597 Media Deutschland GmbH; 2021;70(9):2681–700. DOI: 10.1007/s00262-021-02863-1

1598 87. Kazuko Saeki, Akihiko Yoshimura. The B-cell-specific major raft protein, Raftlin, is
1599 necessary for the integrity of lipid raft and BCR signal transduction. EMBO.
1600 2003;12:3015–26.

1601 88. Saeki K, Fukuyama S, Ayada T, Nakaya M, Aki D, Takaesu G, et al. A Major Lipid Raft
1602 Protein Raftlin Modulates T Cell Receptor Signaling and Enhances Th17-Mediated
1603 Autoimmune Responses. The Journal of Immunology. Oxford University Press (OUP);
1604 2009;182(10):5929–37. DOI: 10.4049/jimmunol.0802672

1605 89. Watanabe A, Tatematsu M, Saeki K, Shibata S, Shime H, Yoshimura A, et al. Raftlin is
1606 involved in the nucleocapture complex to induce poly(I:C)-mediated TLR3 activation.
1607 Journal of Biological Chemistry. American Society for Biochemistry and Molecular
1608 Biology Inc.; 2011;286(12):10702–11. DOI: 10.1074/jbc.M110.185793

1609 90. Bayliss AL, Sundararaman A, Granet C, Mellor H. Raftlin is recruited by neuropilin-1 to
1610 the activated VEGFR2 complex to control proangiogenic signaling. Angiogenesis.
1611 Springer; 2020;23(3):371–83. DOI: 10.1007/s10456-020-09715-z

1612 91. Tatematsu M, Yoshida R, Morioka Y, Ishii N, Funami K, Watanabe A, et al. Raftlin
1613 Controls Lipopolysaccharide-Induced TLR4 Internalization and TICAM-1 Signaling in a
1614 Cell Type–Specific Manner. The Journal of Immunology. Oxford University Press (OUP);
1615 2016;196(9):3865–76. DOI: 10.4049/jimmunol.1501734

1616 92. Lacy MM, Ma R, Ravindra NG, Berro J. Molecular mechanisms of force production in
1617 clathrin-mediated endocytosis. Vol. 592, FEBS Letters Wiley Blackwell; 2018. p. 3586–
1618 605.

1619 93. Mustfa SA, Singh M, Suhail A, Mohapatra G, Verma S, Chakravorty D, et al.
1620 SUMOylation pathway alteration coupled with downregulation of SUMO E2 enzyme at
1621 mucosal epithelium modulates inflammation in inflammatory bowel disease. Open Biol.
1622 Royal Society Publishing; 2017;7(6). DOI: 10.1098/rsob.170024

1623 94. Toda G, Yamauchi T, Kadowaki T, Ueki K. Preparation and culture of bone marrow-
1624 derived macrophages from mice for functional analysis. STAR Protoc. Cell Press;
1625 2021;2(1). DOI: 10.1016/j.xpro.2020.100246

1626 95. Weigmann B, Tubbe I, Seidel D, Nicolaev A, Becker C, Neurath MF. Isolation and
1627 subsequent analysis of murine lamina propria mononuclear cells from colonic tissue. Nat
1628 Protoc. 2007;2(10):2307–11. DOI: 10.1038/nprot.2007.315

1629

- 1. Dynamic expression pattern of SENP5 in chronic colitis and colitis-associated colorectal cancer (CAC)

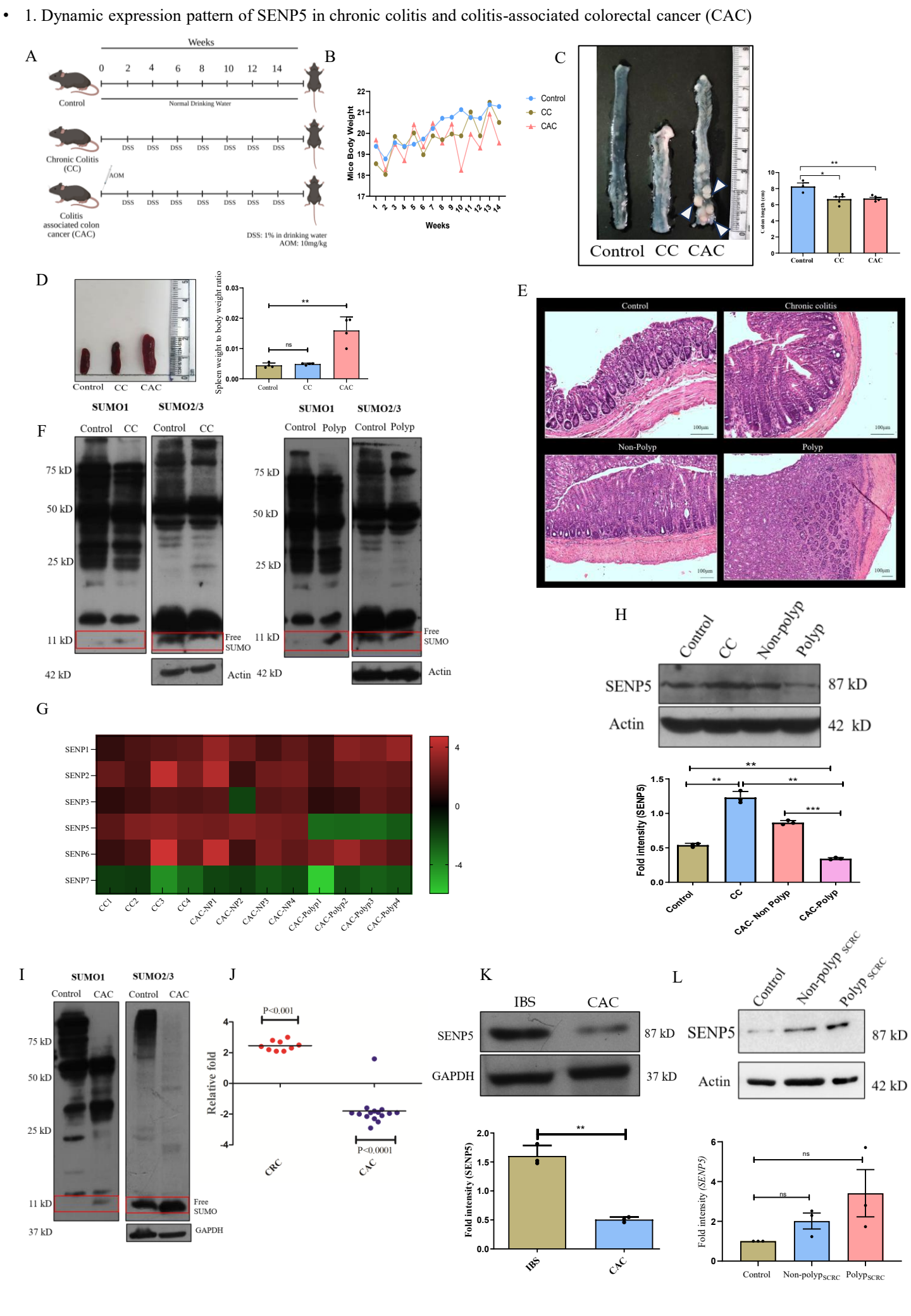

- 2. Altered interactome of SENP5 in Chronic colitis and colitis-associated colorectal cancer (CAC)

A

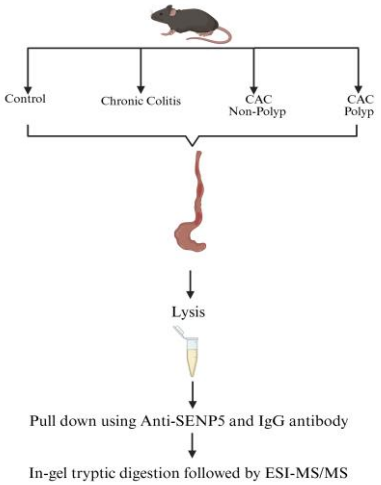


B

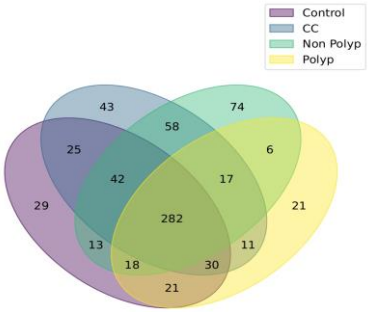


| Sample Name | Number of Unique Elements |
|---|---|
| Control | 460 |
| Chronic colitis | 508 |
| NP CAC | 510 |
| Polyp CAC | 406 |

| Parameters | Values |
|---|---|
| Peptide tolerance | 0.5 Da |
| Significant Threshold | 0.05 |
| Protein FDR | 5 % |
| MS/MS tolerance | 50ppm |

C

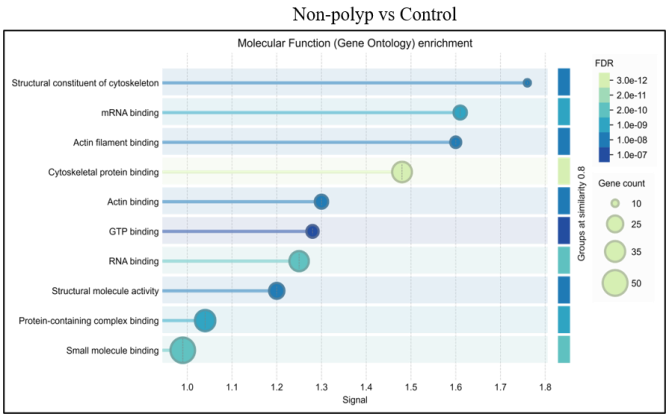


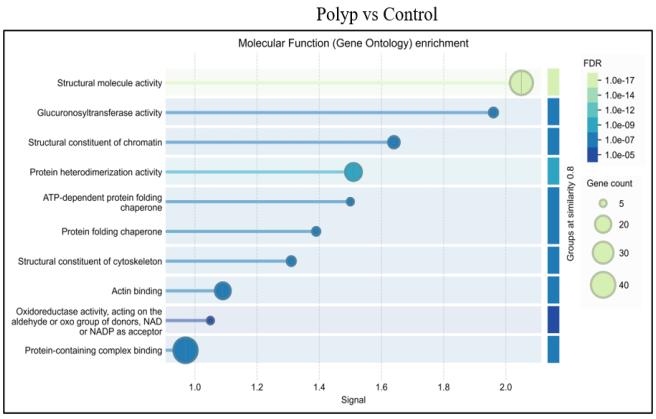


D

| Name of the Protein | Condition of identification | Presence of SUMOylation and/or SIM site | Function and disease reported | References |
|---|---|---|---|---|
| Coronin1A (Coro1a) | Control, CC, Non-Polyp and Polyp | 20, 461, 200-204, 155-159 | Cytoskeleton remodeling, immune cells maturation and trafficking. | *Pick R. et al. Blood, 2017 Jean Pieters et al. Nat. Rev. 2013* |
| Myosin-9 (Myh9) | Control, CC, Non-Polyp and Polyp | 47, 82,180, 228,289, 580, 778, | Cell adhesion, migration. Involved in the EMT process. Play role in SCRC. | *Yan Zhong et al. Cell Death and Differentiation, 2021 Zixuan Gou et al. Rev. Frontier 2021.* |
| Tropomyosin 4 (Tmp4) | Control, CC, Non-Polyp and Polyp | 104, 113, 153, 125, 190, 56-60, 189-193 | Binds actin filaments in muscle and non-muscle cells. Act as Tumor suppressor in SCRC | *Rui Yang et al. Biomed. 2018, Piesi Li et al. Cell Death and Disease 2024* |
| Collagen alpha-3(VI) (Col6a3) | Control, CC, Non-Polyp and Polyp | 32, 98, 698, 504, 242-246, 278-282 | Key structural component of VI collagen, part of the ECM. Predominantly expressed in the stroma of the tumor. Serves as a stromal-specific diagnostic marker. | *Jie Qiao et al. Oncotarget, 2015 Wei Liu et al. Oncol Reports, 2018* |
| Cytoplasmic Dynein 1 heavy chain 1 (Dync1h1) | Control, CC, Non-Polyp and Polyp | | Key motor protein involved in retrograde transport, intracellular cargo trafficking, and cytoskeleton organization Promote proliferation in gastric cancer | *Hongyu Pan et al. Expt. Cell Research, 2021.* |

E

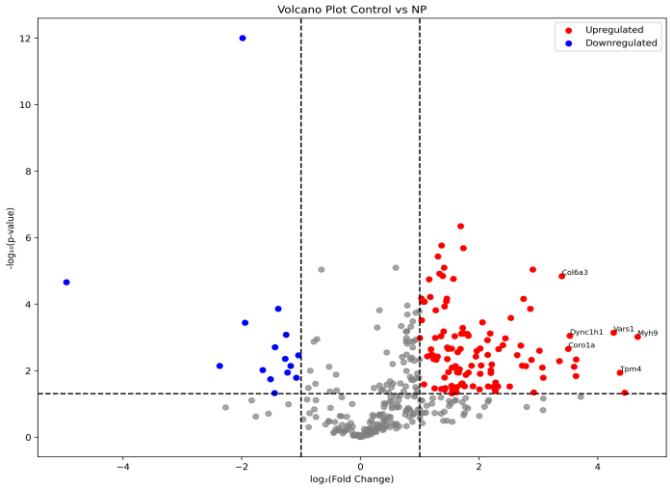


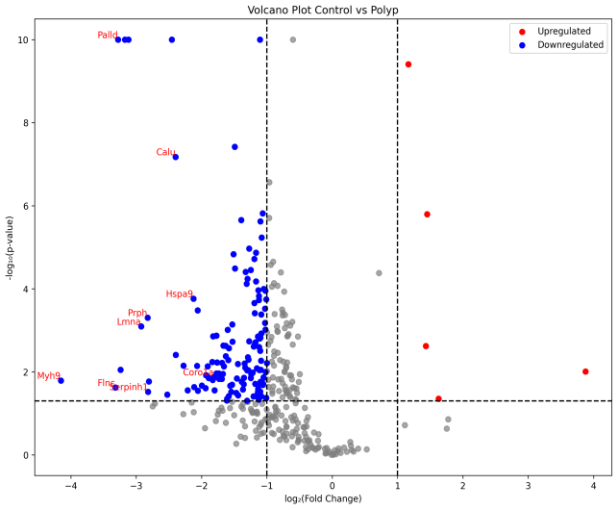

- 3. Coro1A as an interactor of SENP5

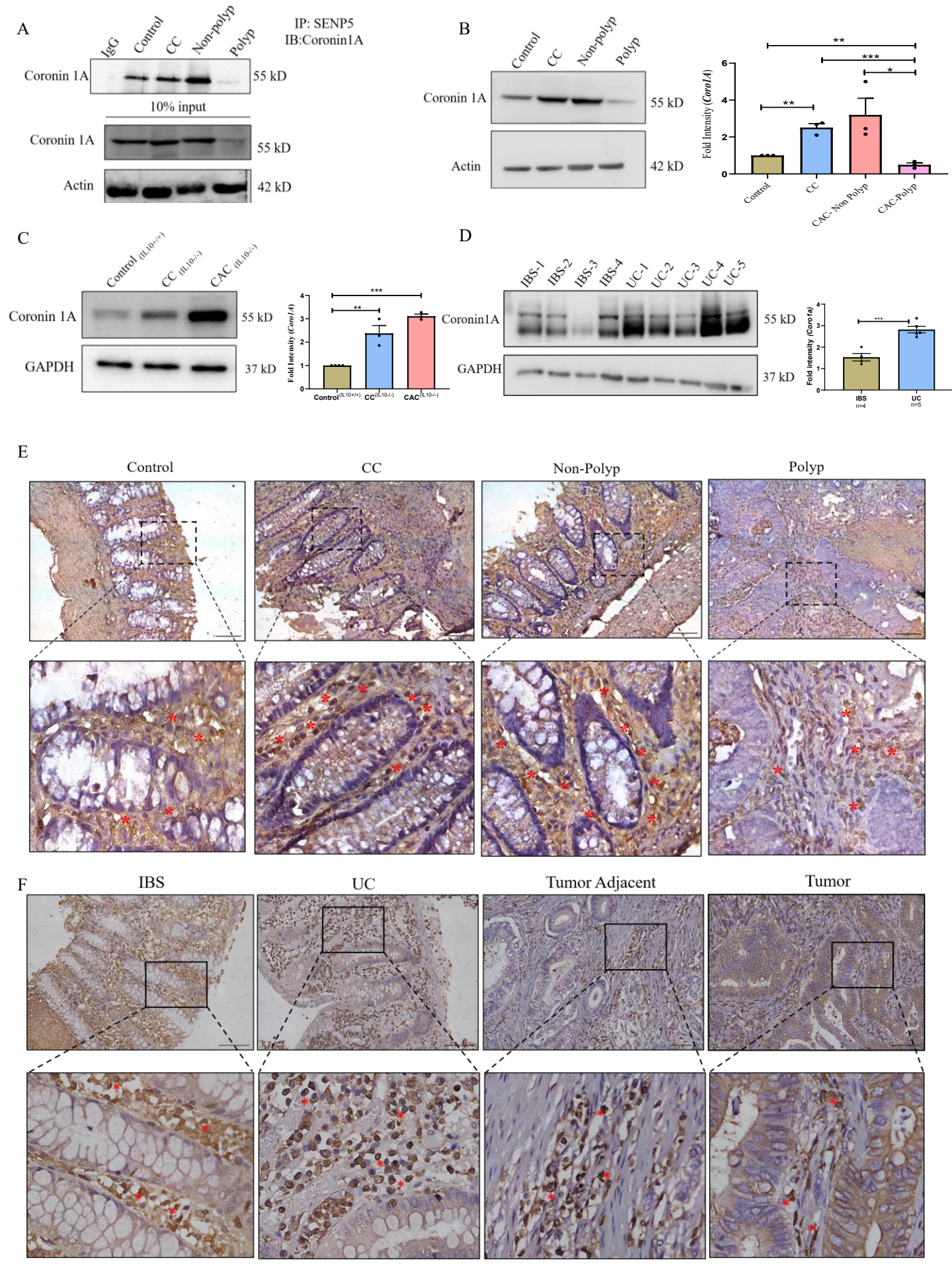

- 4. Absence of Coro 1A confers resistance to CAC development in mice

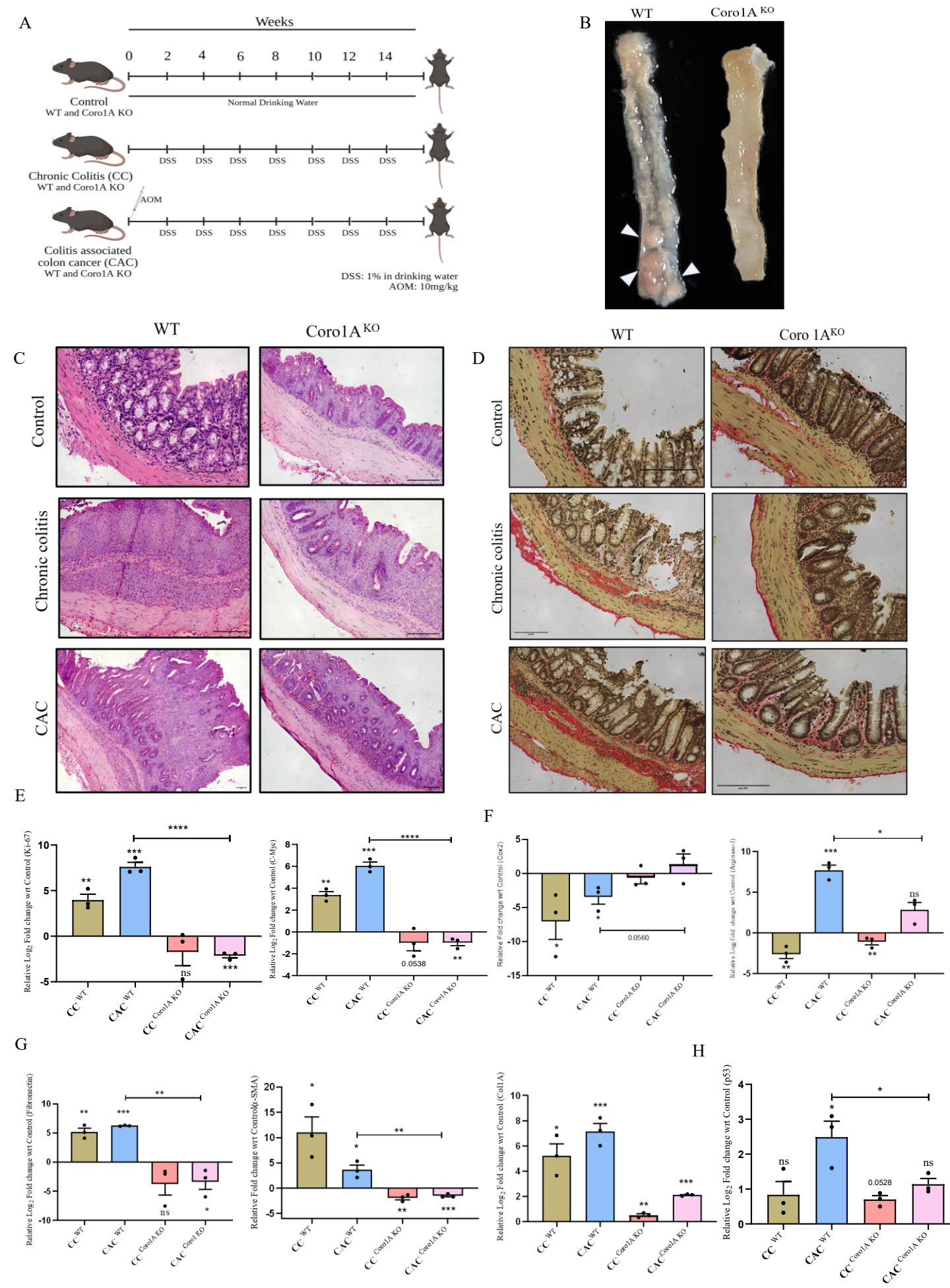

- 5. Increased expression of Coro1A is associated with M2 macrophages

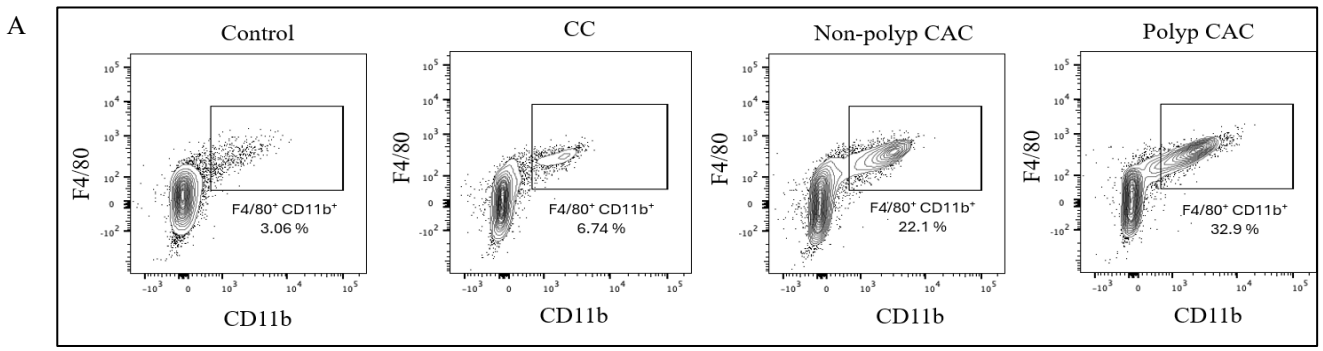


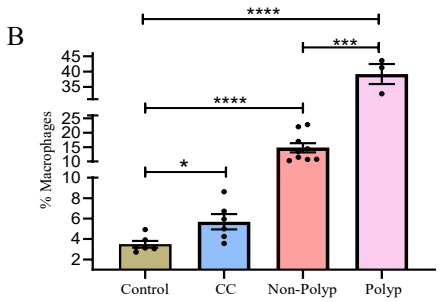


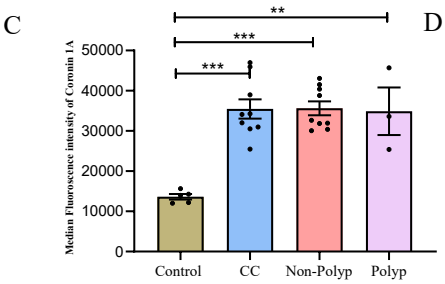


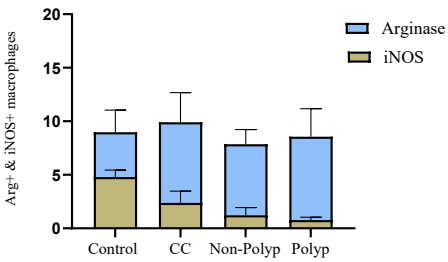


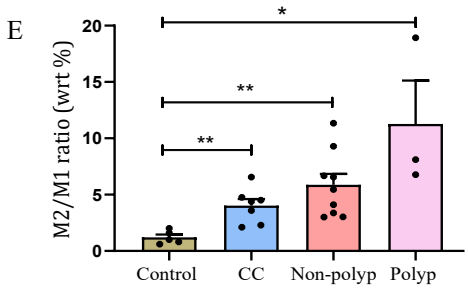


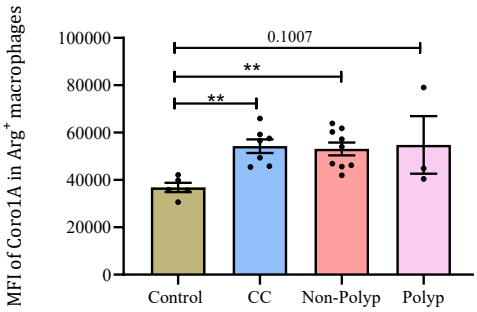


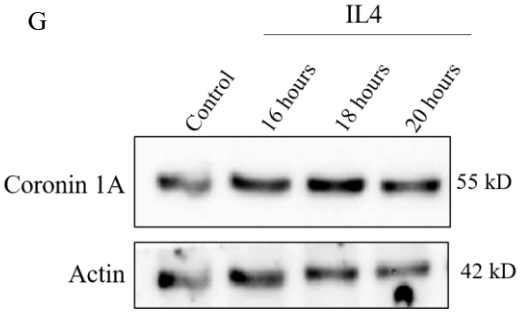


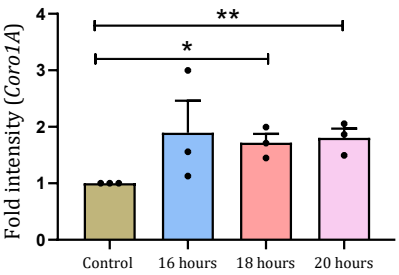


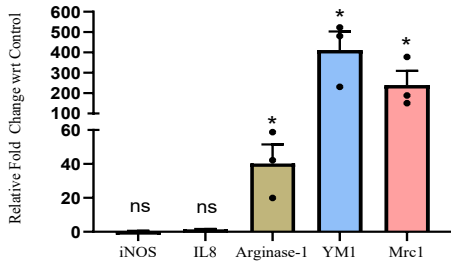


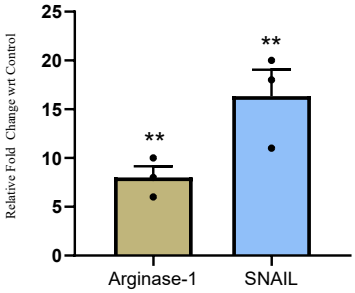


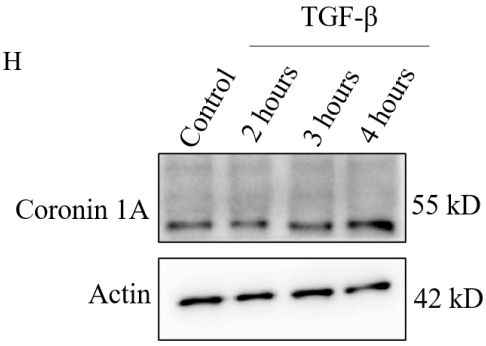


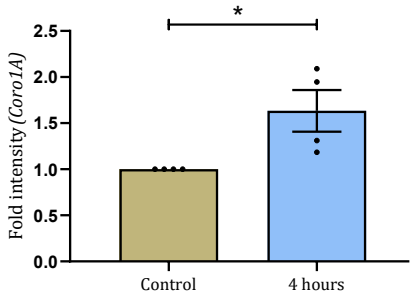


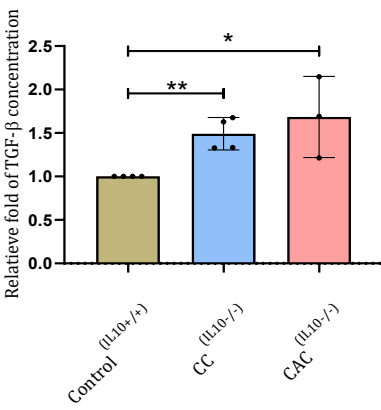

- 6. Coro 1A interacts directly with the TGF-β RI and controls TGF-β-mediated M2 macrophage polarization

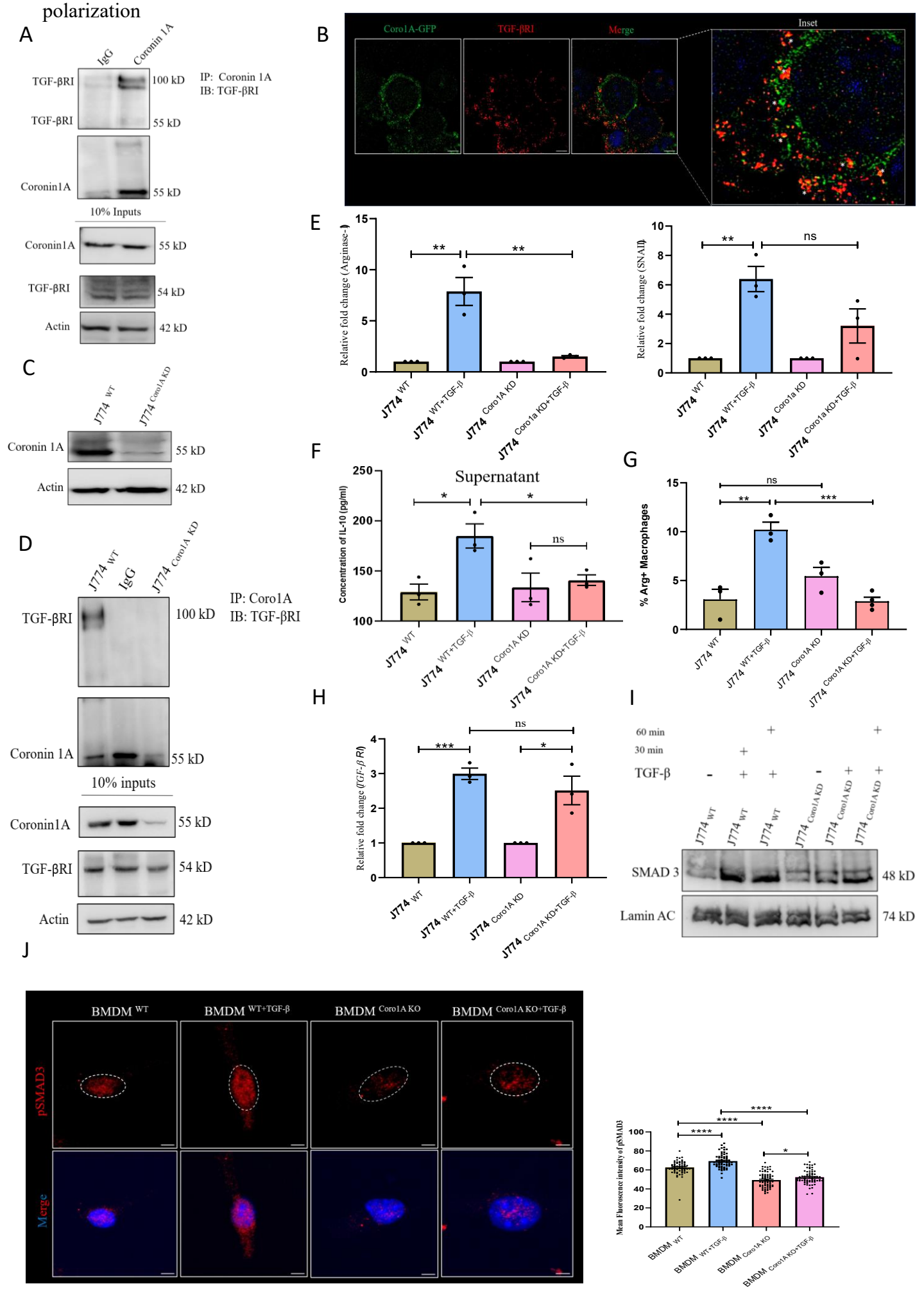

- 7. Coro1A is required for the stability of TGF-βRI

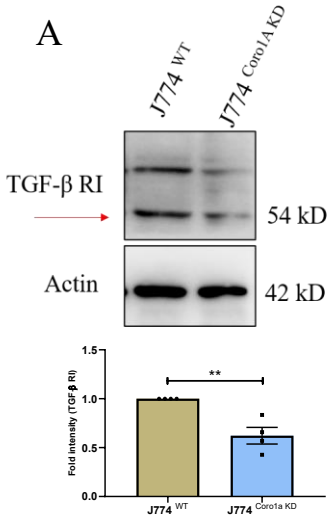


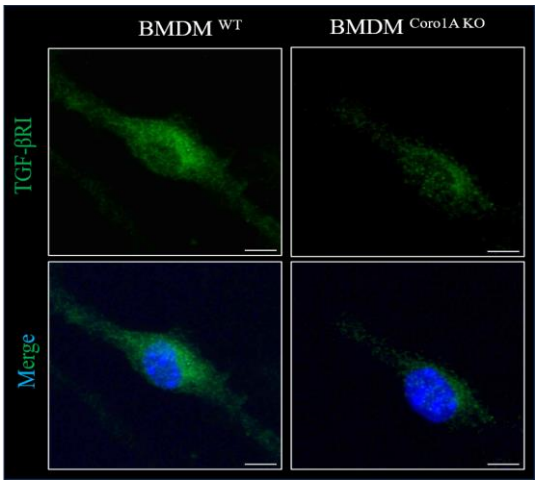


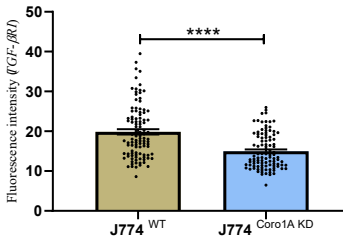


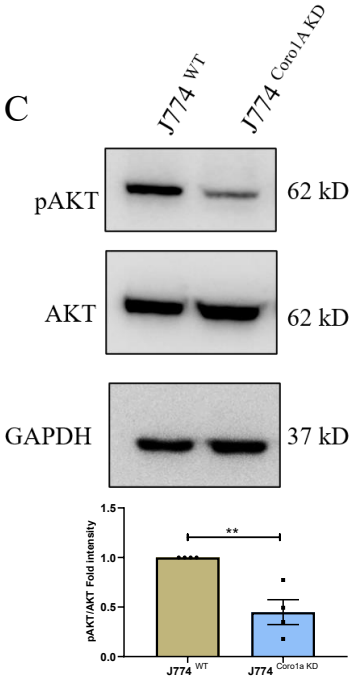


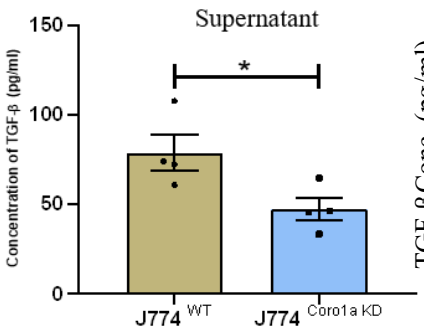


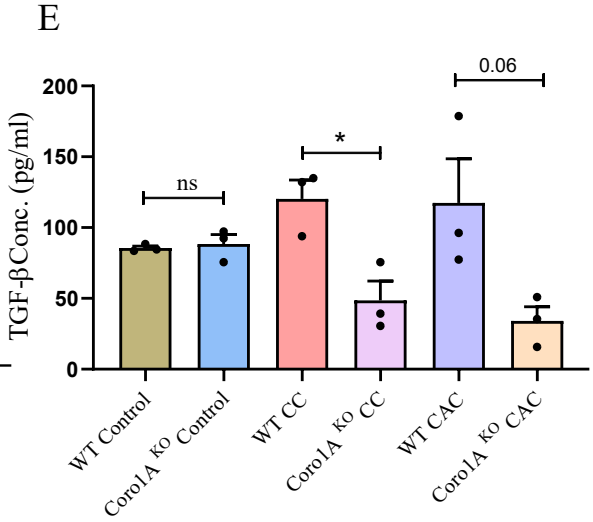


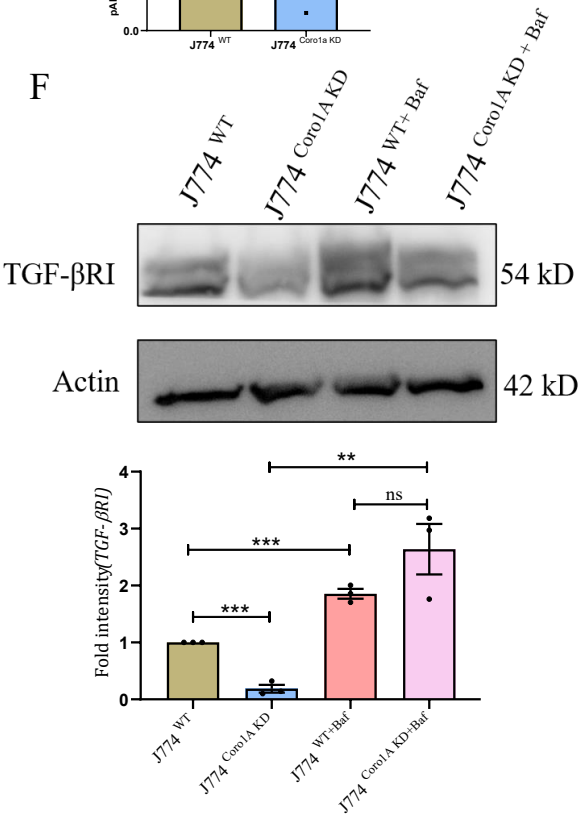


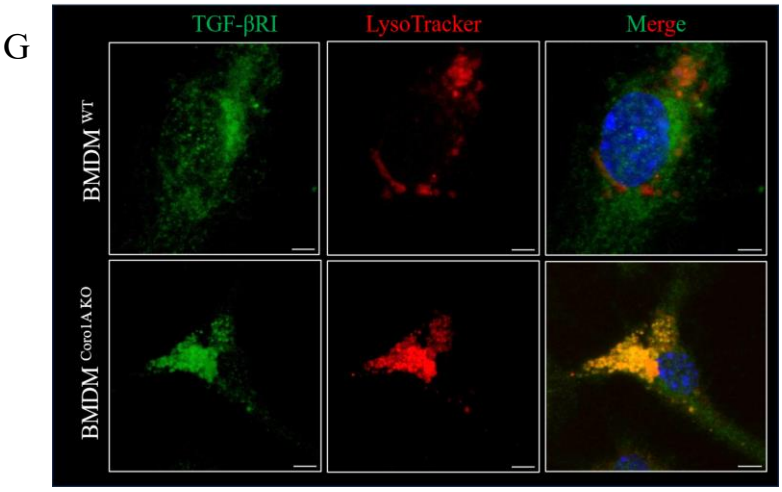


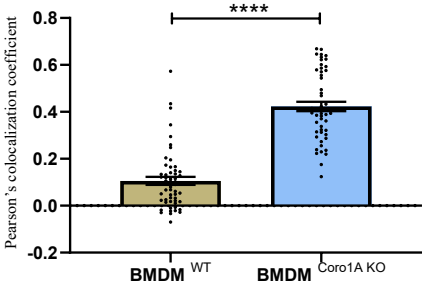

- 8. Coro1A utilizes the calcium-calcineurin signaling pathway to protect TGF-βRI from degradation

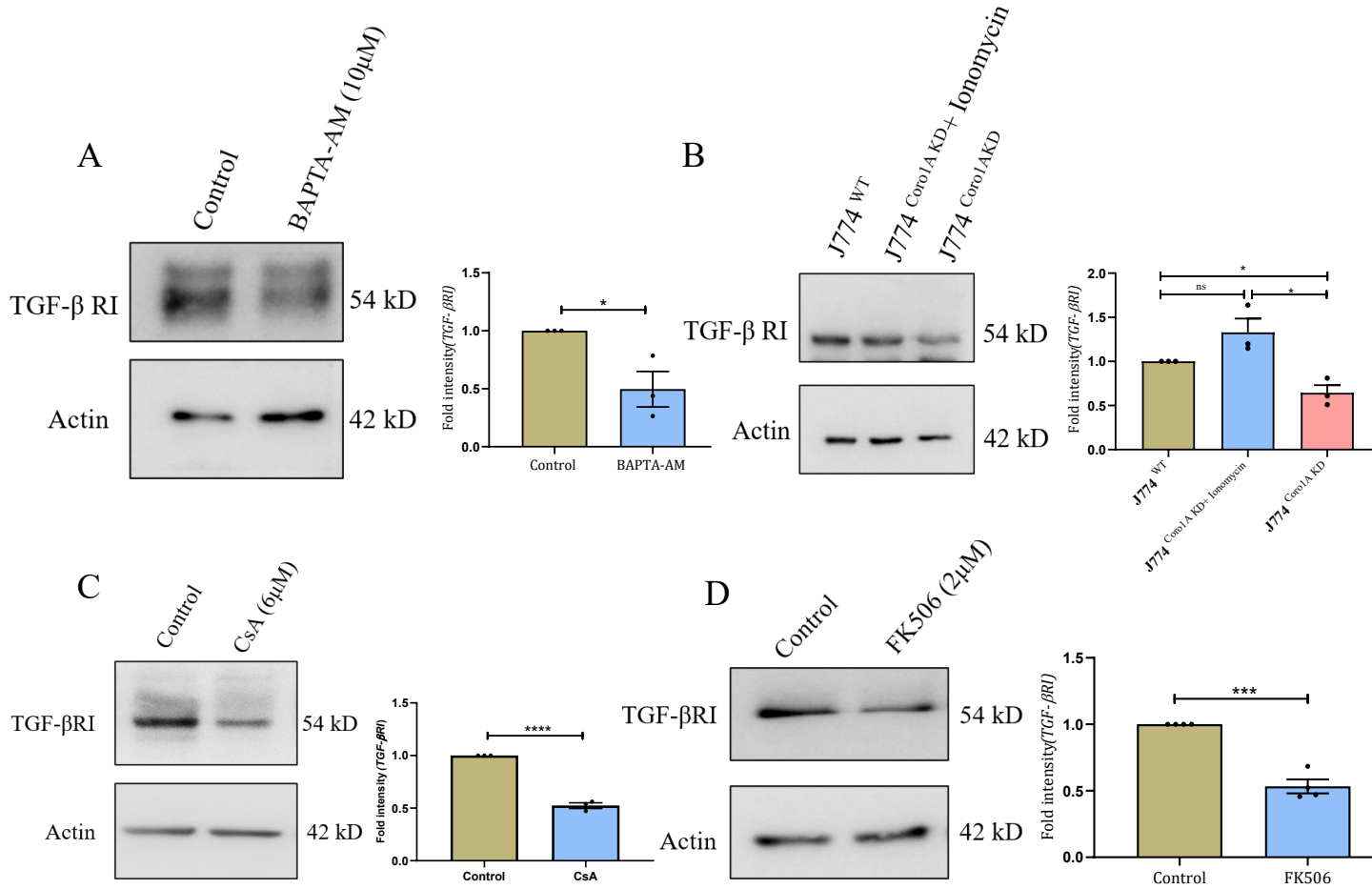

- 9. SUMO2/3 governs stability of Coro1A

A

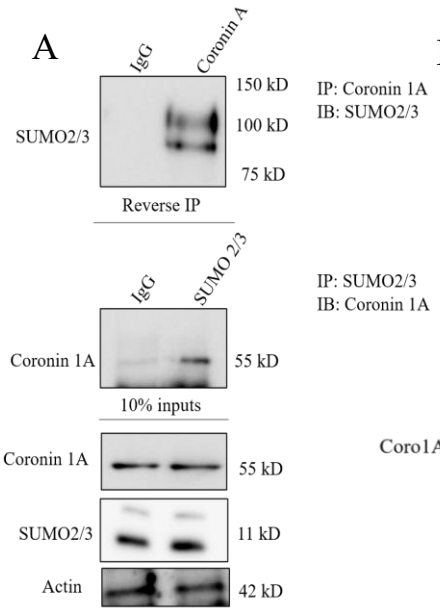


IP: Coronin 1A
IB: SUMO2/3

IP: SUMO2/3
IB: Coronin 1A

B

| Protein | GPS | JASSA |
|---|---|---|
| Coronin 1a | SIM sites | SIM sites |
| | 155-159 | 155-159 (High) |
| | 167-171 | 167-171(High) |
| | 124-128 | 124-128 (High) |
| | 281-285 (High) | 84-87 |
| | 440-444 | 200-204 |

C

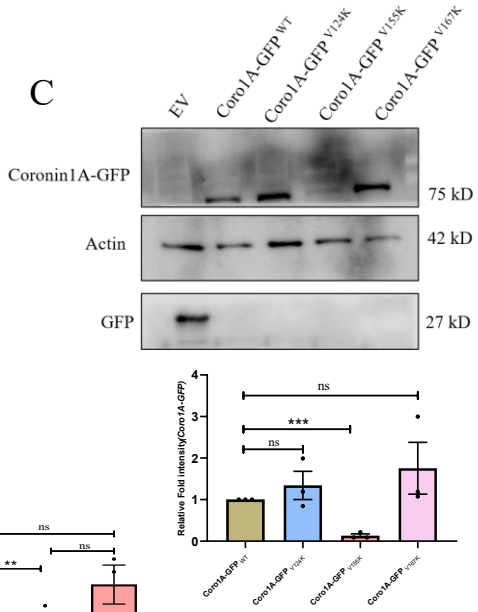


D

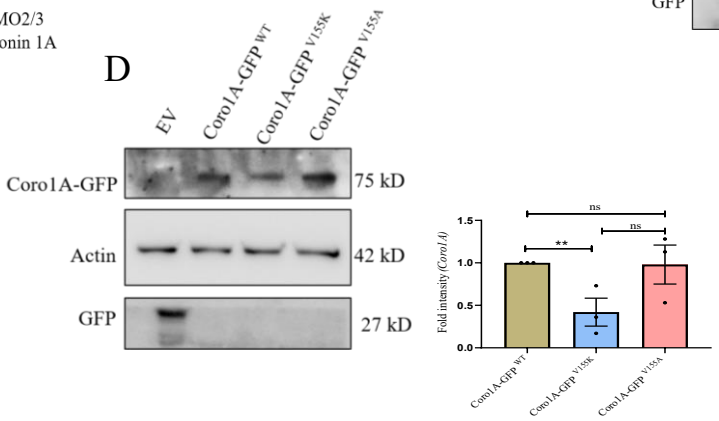


E

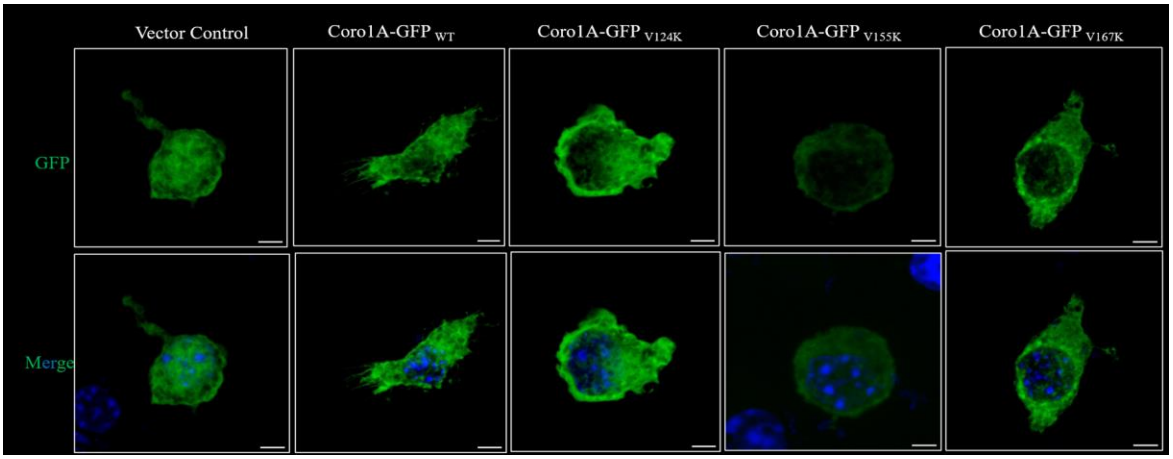


F

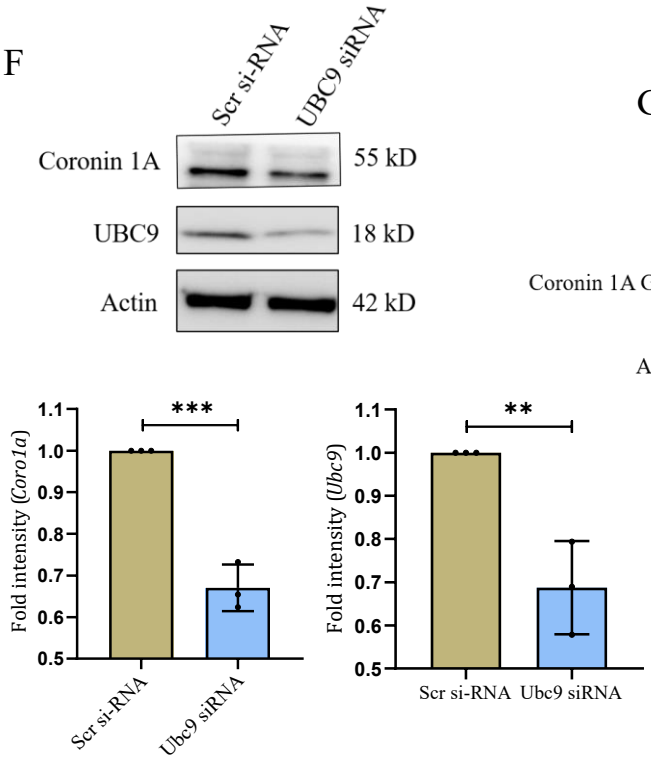


G

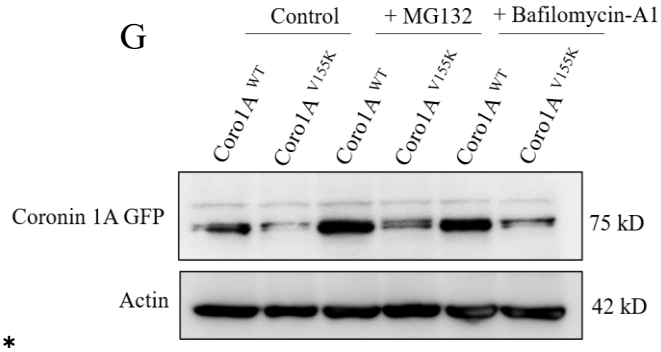

- 10. Coro1A interacts with SUMOylated Raftlin through the SIM site

A

| Gene ID | Name of protein | Gene Name | Class of protein |
|---|---|---|---|
| Q6A0D4 | Raftlin | Rftn1 | Clatherin-AP binding protein |
| Q5NCX5 | Neuralised like protein 4 | Neurl4 | Ubiquitin protein ligaseQ |
| Q8BTF7 | DNA Ligase | Lig4 | DNA metabolism Protein |
| Q9R087 | Glypican-6 | Gpc6 | Scaffold/adaptor protein |
| Q8BGQ6 | EF-hand calcium-binding domain-containing protein-14 | Efcab14 | - |
| Q0VBP7 | Protein shisa like -1 | Shisal1 | Scaffold/adaptor protein |

B

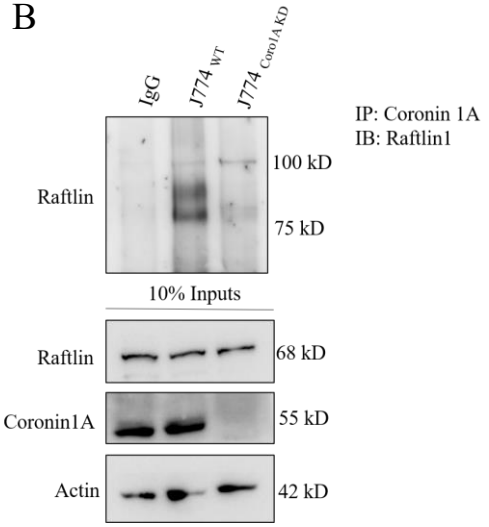


C

| Protein | GPS-SUMO | JASSA |
|---|---|---|
| | SUMO binding sites | |
| Raftlin | K31 | K31 (High) |
| | K224 | K224 (High) |
| | K206 | |
| | K381 | |
| | K481 | |
| | K191 | |

D

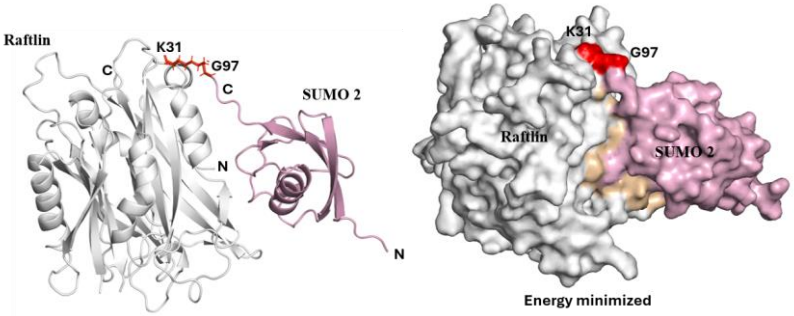


E

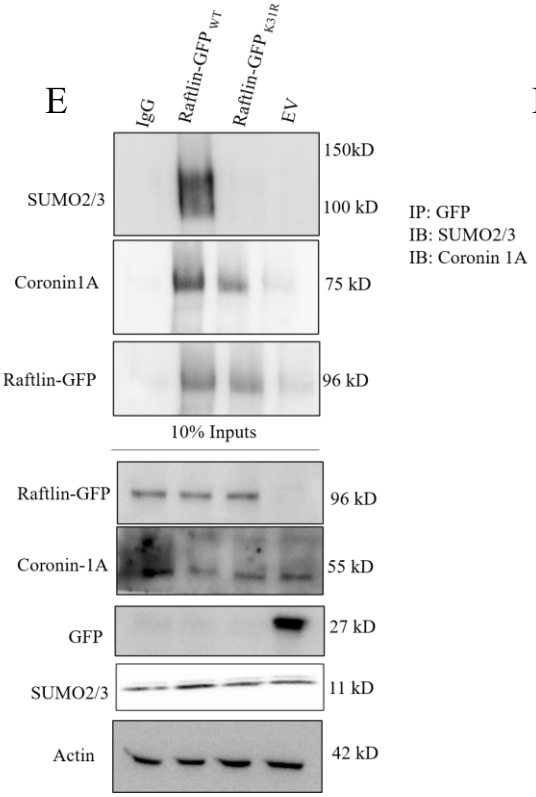


F

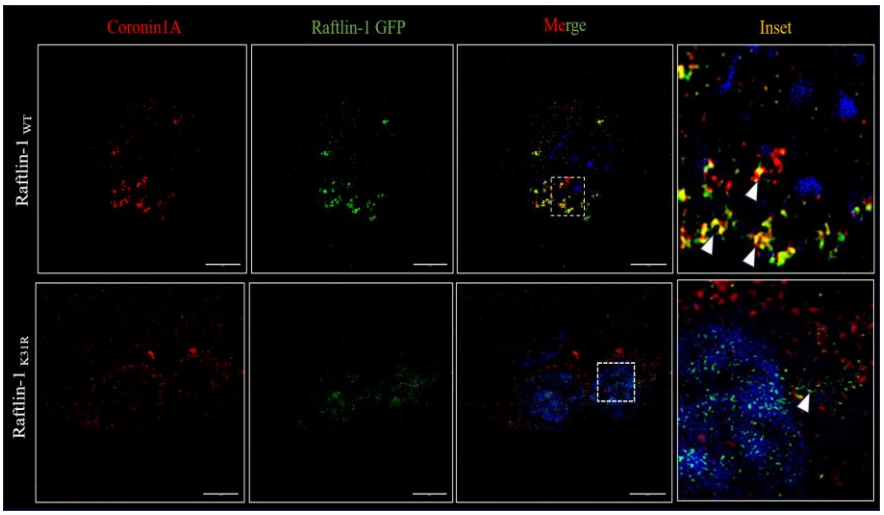


G

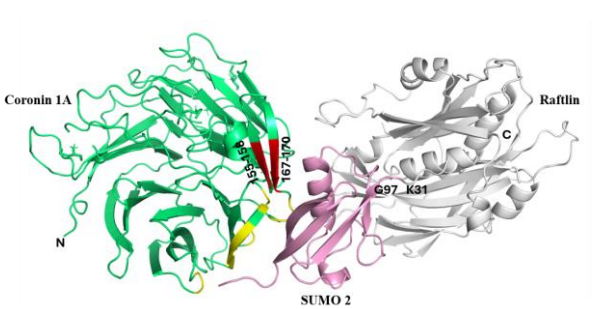


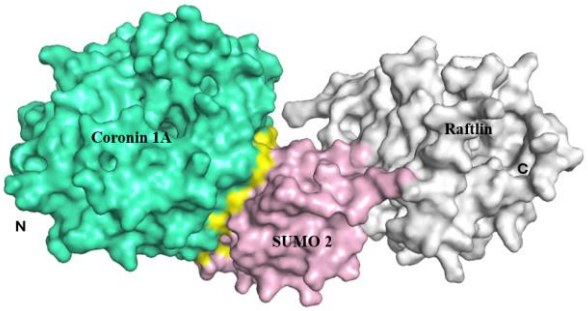

- Supplementary Figure 01:

A

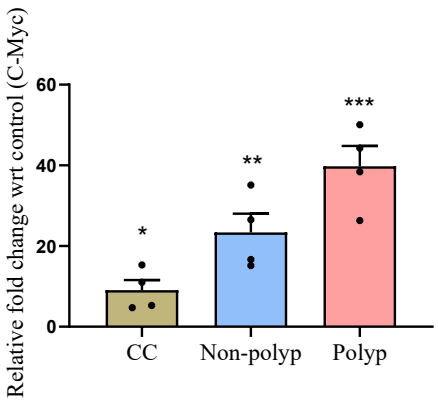


B

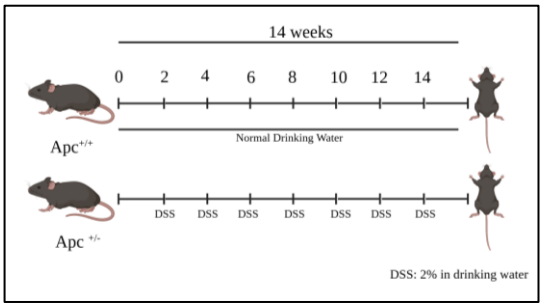


C

- Supplementary Figure 02:

A

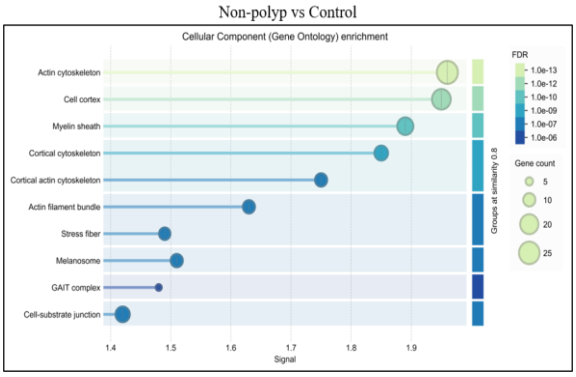


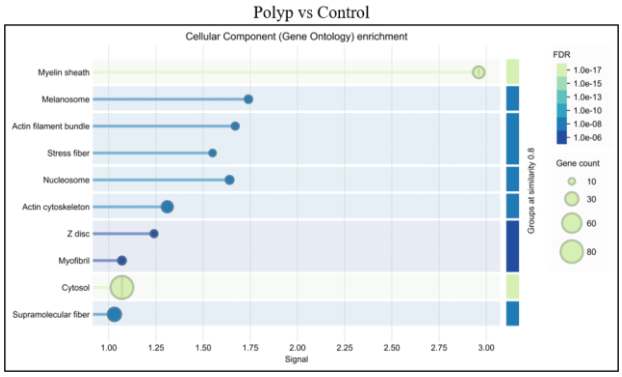


B

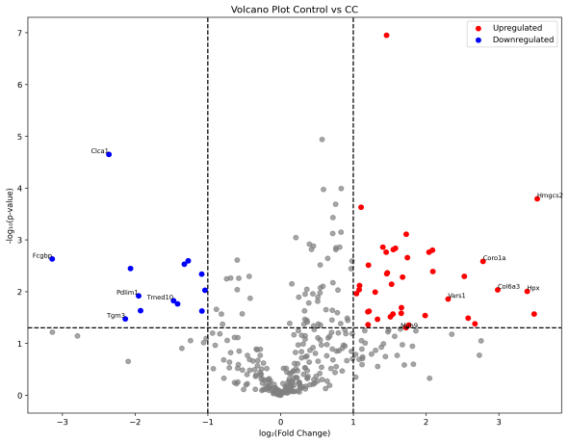

- Supplementary Figure 03:

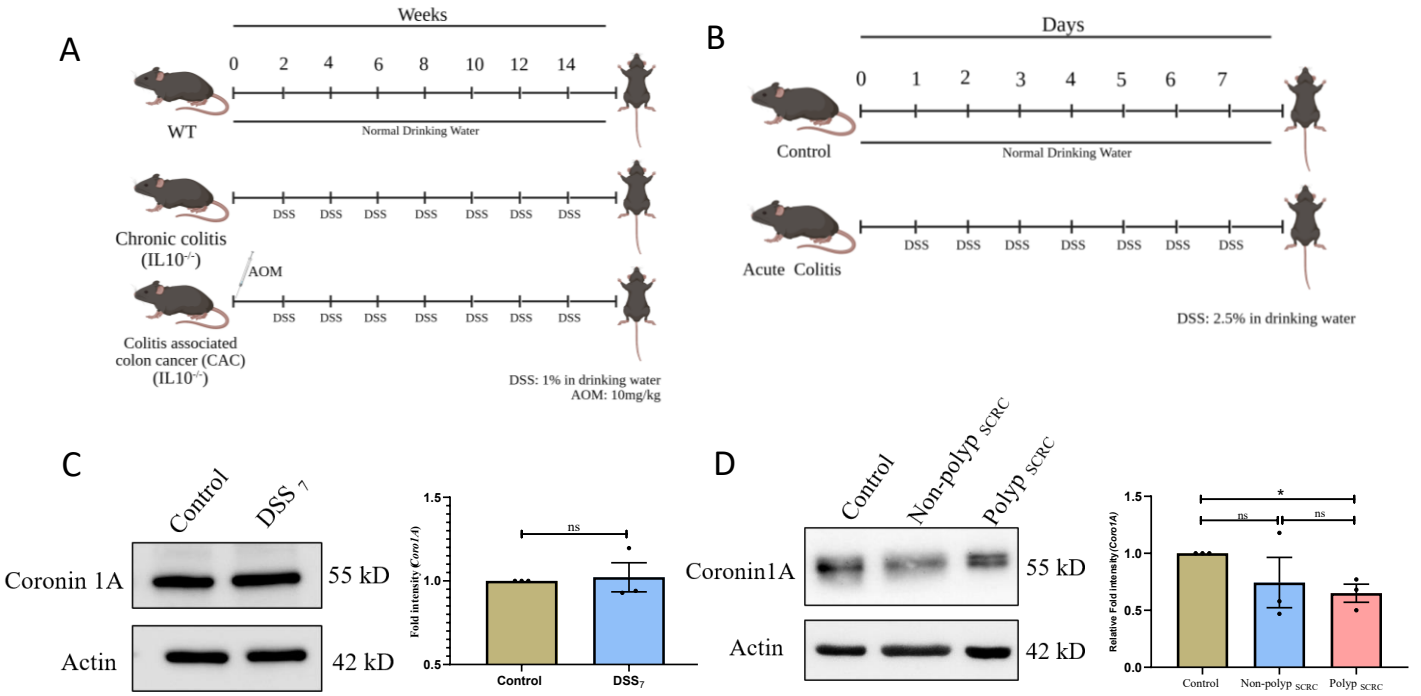

- Supplementary Figure 04:

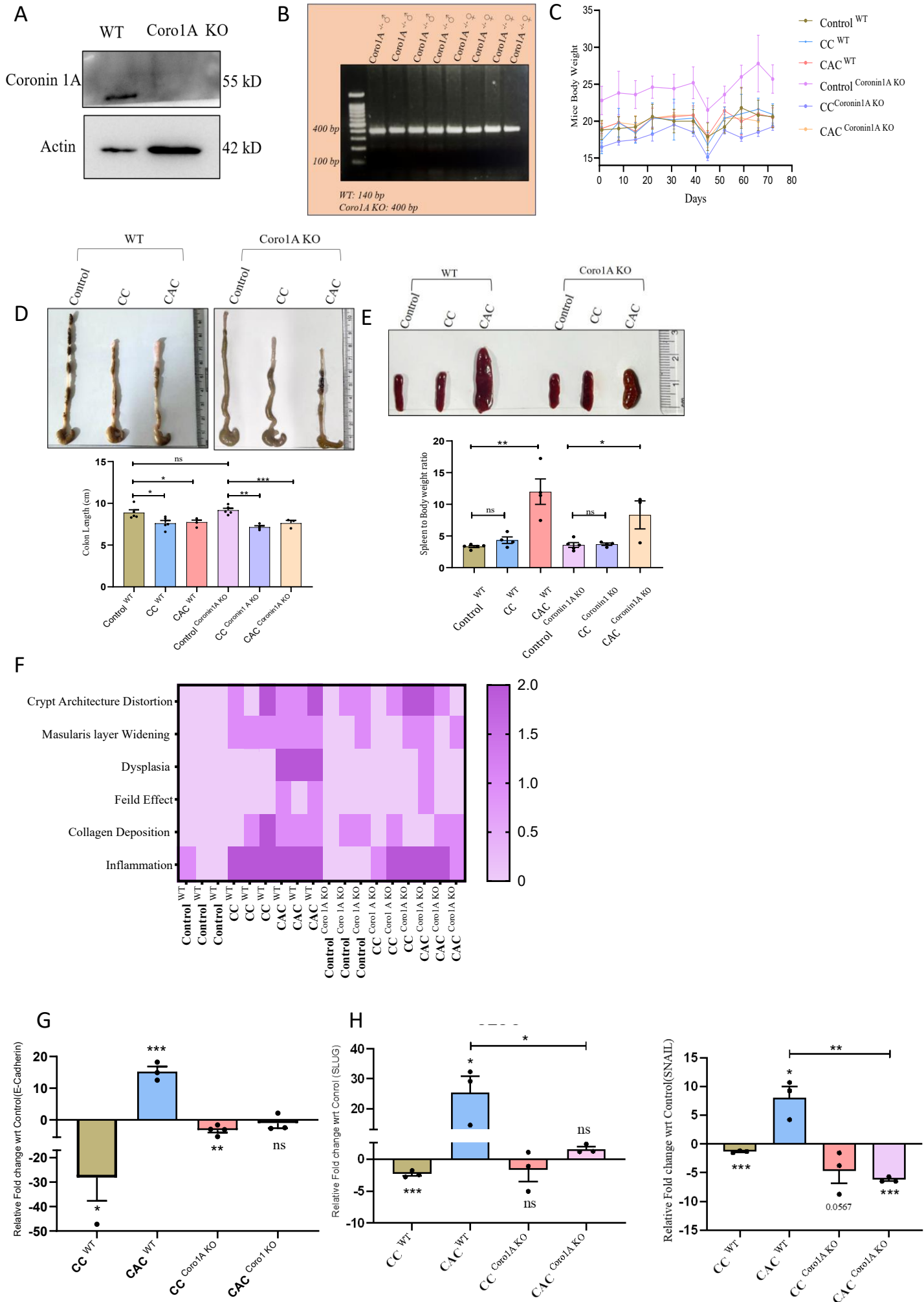

- Supplementary Figure 05:

A

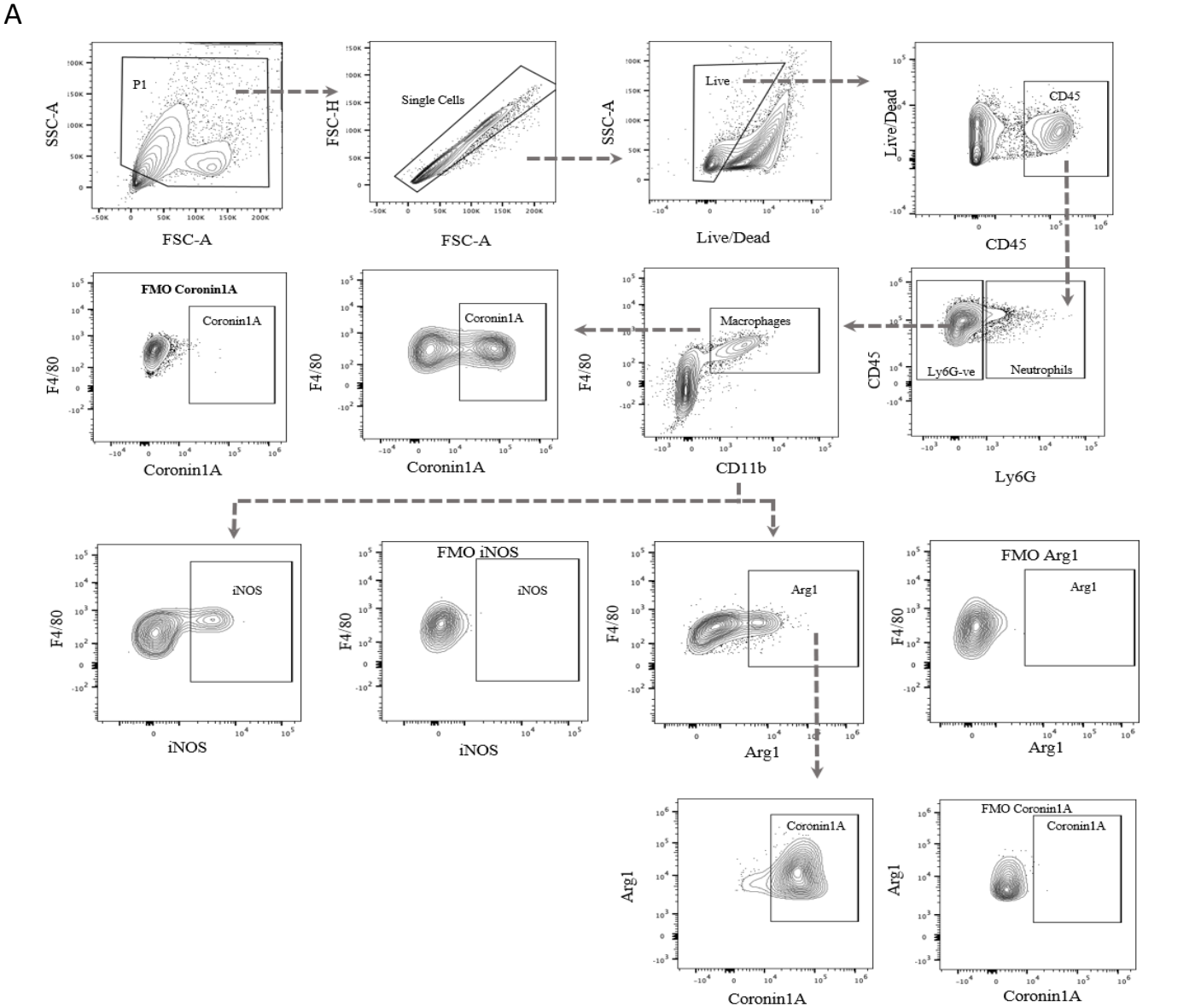


B

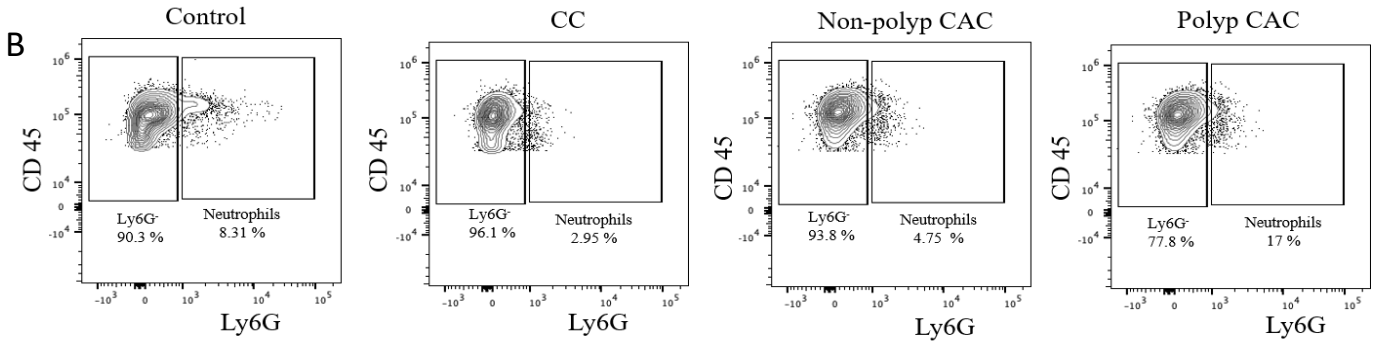


C

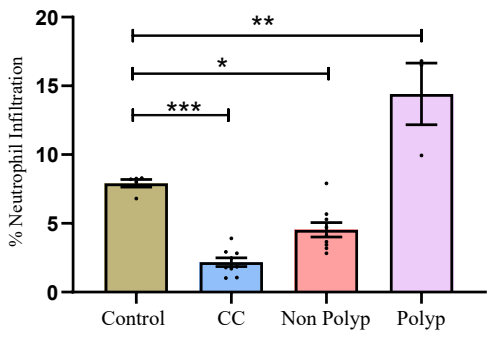


D

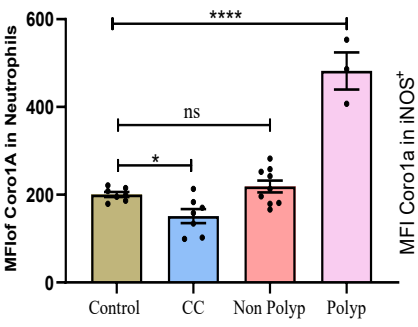


E

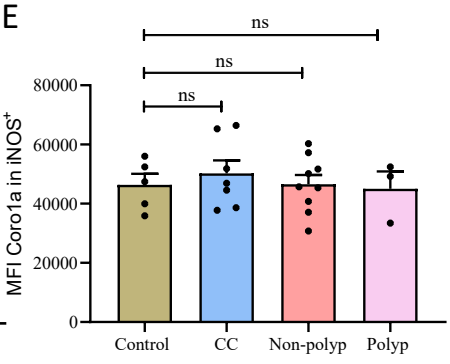

- Supplementary Figure 06:

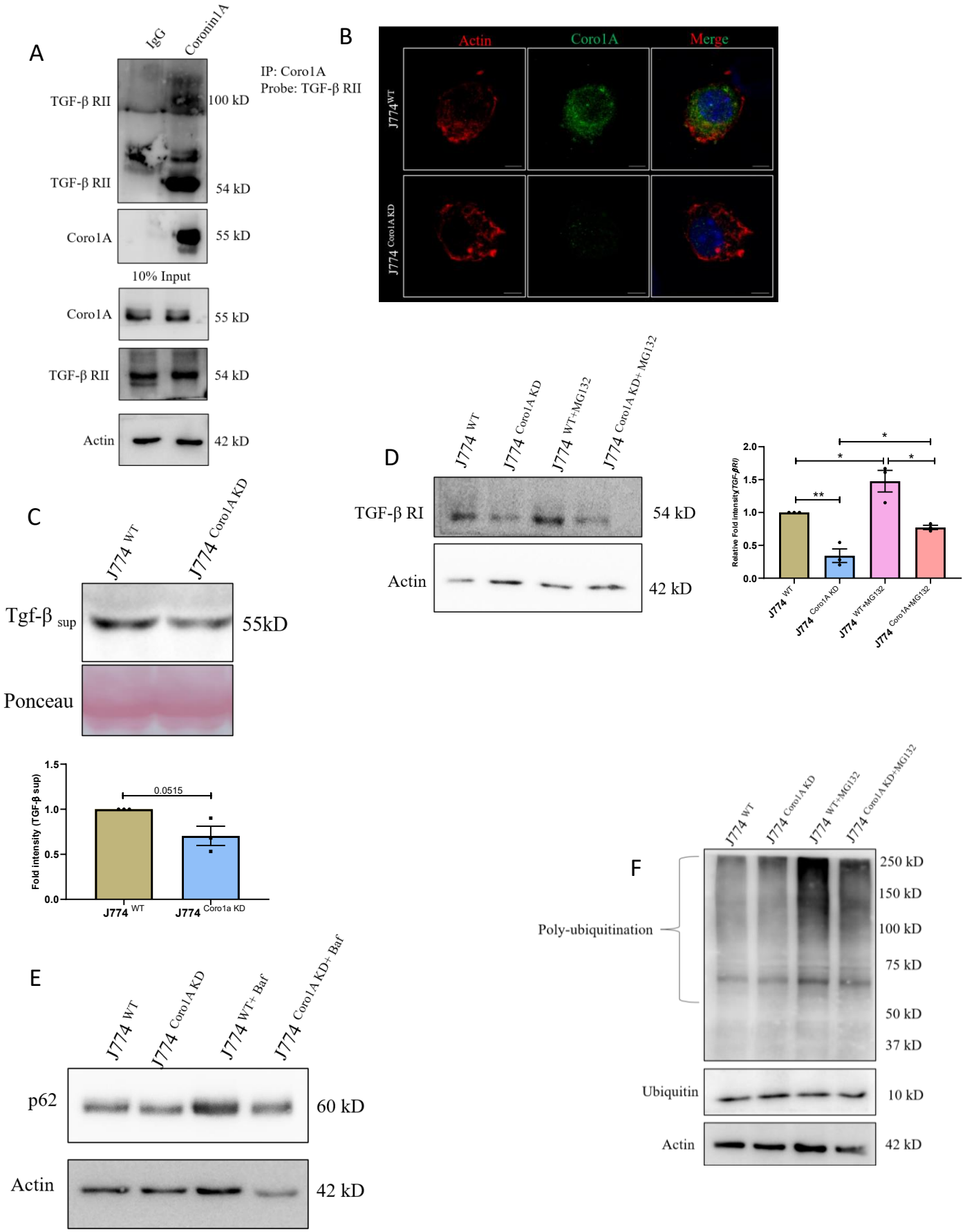

- Supplementary Figure 07:

A

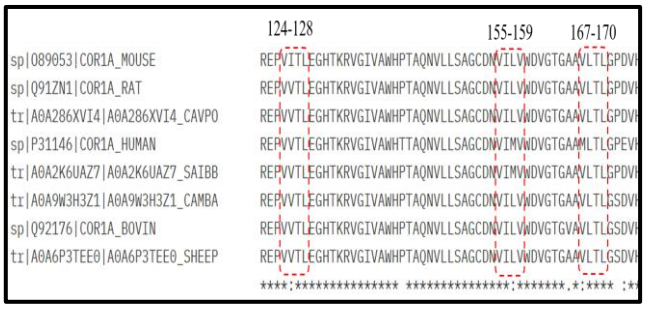


B

| Protein | SIM Sites | SIM Sequence | Mutation in SIM Sequence |
|---|---|---|---|
| Coro1A | 124-128 | VITL | KITL |
| | 155-159 | VILV | KILV |
| | 167-171 | VLTL | KLTL |

C

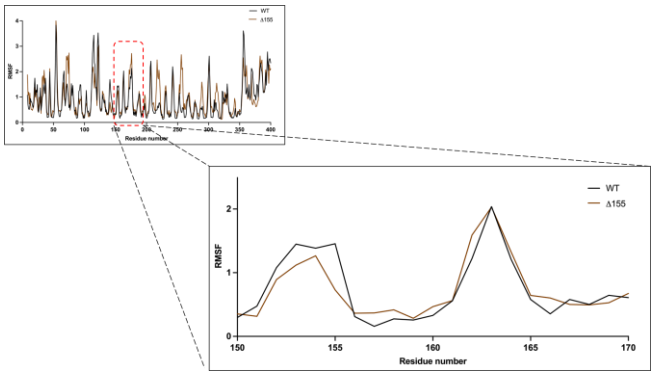


D

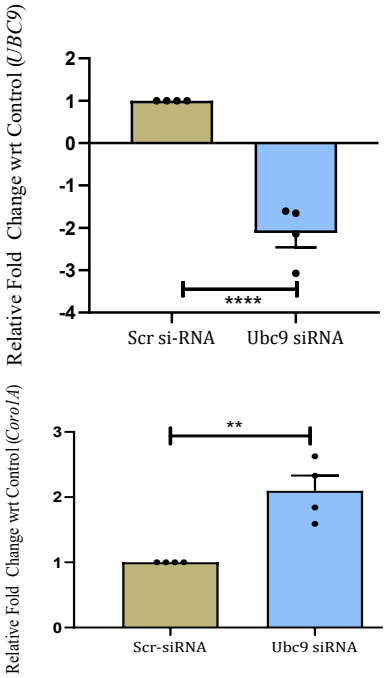


E

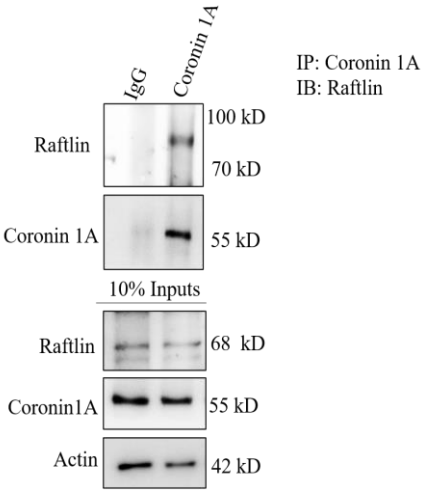


F

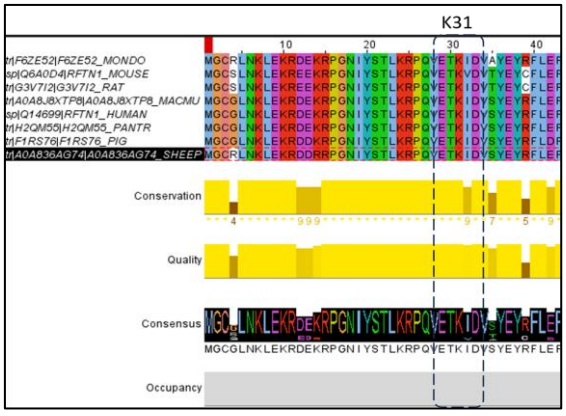

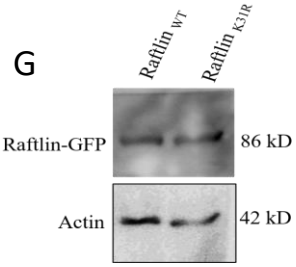
G